Tailored dosimetry in the radioiodine treatment of differentiated thyroid cancer

Tailored dosimetry in the radioiodine treatment of differentiated thyroid cancer

Production
Printing: Datawyse | Universitaire Pers Maastricht
ISBN: 978-94-6295-884-5

Tailored dosimetry in the radioiodine treatment of differentiated thyroid cancer

PROEFSCHRIFT

ter verkrijging van de graad doctor aan de Universiteit Maastricht,
op gezag van de Rector Magnificus, Prof. dr. Rianne M. Letschert,
volgens het besluit van het College van Decanen,
in het openbaar te verdedigen
op woensdag 30 mei 2018 om 14:00 uur

door

Roel Wierts

Promotores
Prof. dr. F.M. Mottaghy
Prof. dr. ir. W.H. Backes

Copromotor
Dr. G.J. Kemerink

Beoordelingscommissie
Prof. dr. ir. F. Verhaegen (voorzitter)
Prof. dr. M. Gotthardt (Radboud University Nijmegen)
Prof. dr. D. De Ruysscher
Prof. dr. ir. P.F.F. Wijn, em. (Eindhoven University of Technology)

Table of contents

Chapter 1

General introduction

Thesis contents

This thesis describes different aspects of tailored dosimetry in the radioiodine treatment of differentiated thyroid cancer (DTC). This involves the use of different radionuclides of iodine for diagnosis and for therapy. First, ^{124}I is used in the detection and characterization of thyroid remnants and iodine-avid lesions, followed by accurate lesion absorbed dose assessment. In a pre-therapeutic setting, this can provide relevant information on treatment outcome and can be used in the optimization of the therapeutic ^{131}I activity dosage. Second, medical imaging and treatment using radionuclides should be performed with acceptable radiation exposure to the patient, personnel, general population and environment. These are in a nutshell the topics that will be covered in the various chapters of this thesis.

Differentiated thyroid cancer

Thyroid carcinoma is a relatively rare type of cancer. With a yearly incidence of 3.1 and 9.3 per 100,000 for men and females respectively, thyroid cancer accounted for less than 2% of all newly diagnosed cancers in Europe in 2012 [1]. However, thyroid cancer is the most frequent endocrine malignancy and during the last three decades the yearly incidence has shown a significant increase worldwide [2]. A large fraction of this rising incidence consisted of small volume tumour [3]. Improved detection of these subclinical tumours due to increased diagnostic scrutiny and advances in technology has been ascribed to contribute to the increase in thyroid cancer incidence [4, 5]. Of all thyroid cancers, the vast majority (>90%) comprises differentiated thyroid carcinomas that derive from the follicular epithelium, including papillary and follicular cancer [6].

In DTC pathology basic biologic characteristics of healthy thyroid tissue, including specific iodine uptake through the sodium iodide symporter, are retained. Given appropriate treatment including radioiodine therapy, the prognosis of DTC is in general excellent, and 10-year relative survival rates[1] of 0.98 for papillary and 0.92 for follicular disease have been reported [7]. However, in patients presenting distant metastases, substantially lower survival rates in the range of 0.25 – 0.40 have been described [8, 9]. Furthermore, as a result of the relatively high recurrence rate up to 0.10 – 0.30, lifelong follow-up is recommended and subsequent therapy is needed in a substantial number of patients [10]. The application of personalized radioiodine treatment using accurate patient specific dosimetry calculations based on advanced pre-therapeutic molecular imaging techniques such as ^{124}I PET/CT or PET/MRI may further improve patient treatment and outcome.

[1] The 10-year relative survival rate is defined as the overall survival 10 years after diagnosis of the disease divided by the 10 year survival of a comparable population not diagnosed with the disease.

Intermezzo: Radioactive iodine

Iodine is a chemical element belonging to the halogen group. The elemental form of iodine was discovered in 1811 by the French chemist Bernard Courtois. Based on its purple-violet colour, the element was named after the Greek word ιωδης meaning "violet". ^{127}I is the only stable isotope of iodine having a natural abundance of 100%. In 1934 Enrico Fermi produced the first radioisotope of iodine by neutron bombardment: ^{128}I.

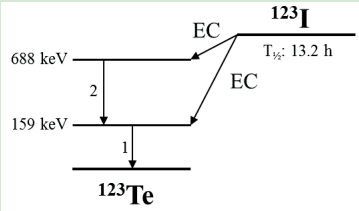

Transition	Energy (keV)	Yield (%)
ce $K_{\gamma 1}$	127	13.6
K_α	27	70.4
K_β	31	14.7
γ_1	159	83.3
γ_2	529	1.4

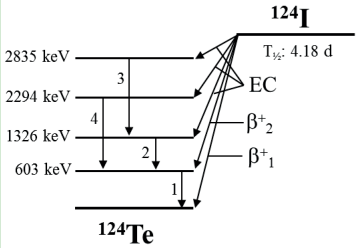

Transition	Energy (keV)	Yield (%)
β^+_1	2138†	10.7
β^+_2	1535†	11.7
K_α	27	47.2
K_β	31	9.7
$\gamma^\pm$	511	45
γ_1	603	62.9
γ_2	723	10.4
γ_3	1509	3.3
γ_4	1691	11.2

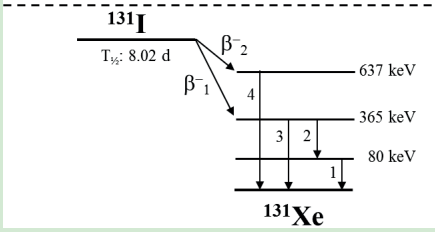

Transition	Energy (keV)	Yield (%)
β^-_1	606†	89.6
β^-_2	334†	7.2
γ_1	80	2.6
γ_2	284	6.1
γ_3	364	81.5
γ_4	637	7.2

FIGURE 1.1. Physical characteristics of radioisotopes of iodine used in medicine: ^{123}I (top), ^{124}I (middle) and ^{131}I (bottom).

EC: electron capture, ce: conversion electron, $T_{½}$: half-life, K: characteristic X-ray photon emitted by electron transition to K shell from L (α) or higher shells (β).
† Beta particle end-point-energy.

The potential of using radioactive iodine for both measurement of thyroid function and therapy of thyroid cancer was quickly recognized and the first patients were treated with ^{131}I in the early 1940s [11]. With the development of the first gamma camera by Anger in 1952 [12], radioiodine became the first theranostic (radio)pharmaceutical.

The radioisotopes of iodine used in medical diagnosis and therapy of thyroid disease are mostly limited to ^{123}I, ^{124}I and ^{131}I. In Figure 1.1 the physical characteristics of these isotopes are presented.

For diagnostic imaging ^{123}I, ^{124}I and ^{131}I are all used, whereas ^{131}I is generally used for radionuclide therapy purposes due to its emission of β^--particles. For quantitative pre-therapeutic imaging, ^{124}I positron emission tomography (PET) is the preferred imaging technique since it has a 100 to 150 times higher detection efficiency compared to ^{123}I and ^{131}I single-photon emission computed tomography (SPECT) [13]. In addition, ^{124}I PET has the best spatial resolution followed by ^{123}I SPECT and ^{131}I SPECT. In Figure 1.2 an overview of the spatial resolution for all iodine radioisotopes and corresponding imaging technique is shown [13].

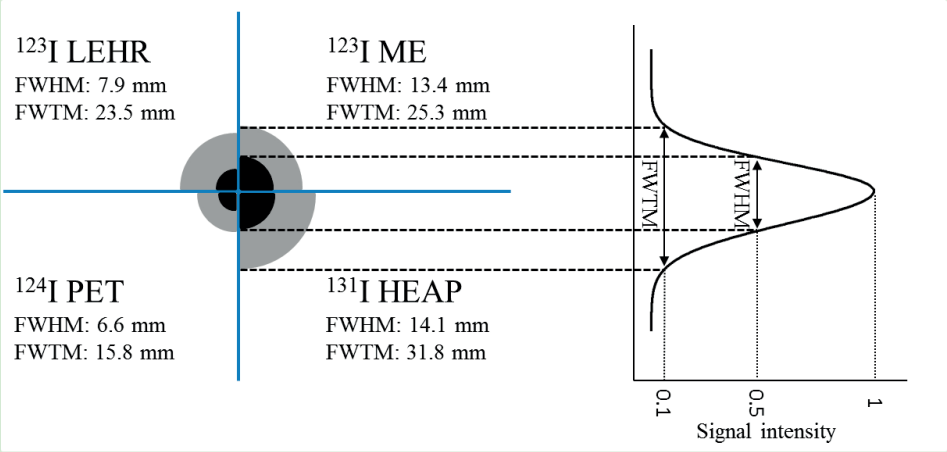

FIGURE 1.2. Comparison of the full-width at half and tenth of maximum (FWHM and FWTM) spatial resolution between ^{123}I SPECT, ^{124}I PET and ^{131}I SPECT, according to Rault et al.[13]. The spatial resolution of ^{123}I is shown for two different types of SPECT collimators: low energy high resolution (LEHR) and medium energy (ME). For ^{131}I the high energy all purpose (HEAP) collimator is used.

Radioiodine therapy

In general, total thyroidectomy is the preferred initial surgical procedure in DTC patients followed by radioiodine treatment 4-6 weeks after surgery [14]. In radioiodine treatment ^{131}I sodium or potassium iodide is systemically administered to a patient. Three distinct but closely interrelated objectives for radioiodine treatment can be distinguished: 1) ablation of possible thyroid remnant tissue, 2) adjuvant therapy aimed to reduce risk of recurrence and mortality by elimination of potential residual microscopic tumour deposits, and 3) treatment of non-resectable or incompletely resectable iodine-avid tumours [6].

The aim of thyroid remnant ablation is to eliminate all remaining thyroid tissue, which will increase the sensitivity and specificity of follow-up testing of persisting and recurrent disease. Post-ablative ^{131}I whole body scintigraphy and SPECT/CT imaging, performed approximately one week after ablation dose administration, can provide relevant information on the existence of iodine-avid metastases and is therefore used for staging. Prior to thyroid remnant ablation, imaging using radioactive iodine can be performed for verification of completeness of the total thyroidectomy and staging. However, administration of diagnostic quantities of ^{131}I for pre-ablation imaging has been reported to reduce iodine uptake and residence time in the subsequent ablation therapy and can thereby decrease the effectiveness of the ablation, an effect known as stunning [15]. To minimize possible stunning effects, it is recommended to limit the pre-therapeutically delivered absorbed dose to thyroid remnants [16].

Although a personalized approach is required by the European union council directive 2013 [17], in clinical practise, empirically determined fixed amounts of ^{131}I activity are generally administered in radioiodine treatment based on disease characteristics and patient age, with the risk of under- or overdosing [10, 18, 19]. Radioiodine treatment in DTC has been shown to result in adverse effects such as salivary gland dysfunction, transient gonadal dysfunction and second primary malignancies. The prevalence and severity of these effects have been shown to correlate with increasing ^{131}I dose [20]. Since several studies reported no statistically significant differences in success rate between low-dose (1.1 – 1.85 GBq) and high-dose (3.7 – 5.5 GBq) ^{131}I radioiodine therapy in low- to intermediate-risk patients[2] [21-24], low-dose radioiodine therapy may be feasible and could result in a decrease of adverse effects. In contrast, for patients presenting with distant metastases radioiodine therapy success is decreased and multiple high-dose (3.7 – 7.4 GBq) radioiodine treatments are often required [10]. As Kulkarni et al. demonstrated that in more than 90% of such patients even much higher doses can be administered, they concluded that the majority of high-risk patients are potentially undertreated using a fixed radioiodine activity approach [25].

As an alternative to empirically determined fixed ^{131}I activity approaches, pre-therapeutic dosimetry can be used to facilitate personalized radioiodine treatment. To this purpose, two main approaches have been developed: 1) maximum-tolerated radioiodine activity administration and 2) lesion-based dosimetry. In the maximum-tolerated activity approach, the therapeutic amount of radioiodine is calculated to restrict either the absorbed dose to the blood to 2 Gy (a limit which is widely accepted for red bone marrow toxicity) or the 48 hour post-administration whole-body retention to 4.4 GBq in

[2] Risk stratification according to the American thyroid association:
- Low-risk: intra-thyroidal DTC without evidence of extra-thyroidal extension, vascular invasion or metastases.
- Intermediate-risk: microscopic extra-thyroidal extension, cervical lymph node metastases, radioiodine-avid disease in the neck outside the thyroid bed region, vascular invasion or unfavorable tumour histology.
- High-risk: gross extra-thyroidal extension, incomplete tumour resection, distant metastases or unfavorable thyroglobulin (Tg) values after thyroidectomy.

the absence of diffuse lung metastases [10]. The European association of nuclear medicine dosimetry committee has published a standard operational procedure guideline on blood absorbed dose assessment in differentiated thyroid cancer therapy [26]. In the lesion-based dosimetry approach, the amount of therapeutic radioiodine activity is optimized to ensure a lesion absorbed dose above established threshold values reported to yield high therapeutic response, whilst minimising the risk to the patient. The generally accepted absorbed dose threshold values are 300 Gy for thyroid remnants and 85 Gy for lymph node metastases [27, 28]. Despite the fact that the biological effectiveness of dosimetry guided approaches is not proven yet [10] and, consequently, personalized radioiodine treatment is not globally adopted, the use of pre-therapeutic lesion absorbed dose assessment based on ^{124}I positron emission tomography/computed tomography (PET/CT) imaging has been reported to change patient management in 25%-50% of DTC patients [29, 30].

Hybrid PET/CT and PET/MRI

PET is a three-dimensional (3D) non-invasive nuclear imaging technique that uses the unique decay characteristics of radionuclides that disintegrate via β^+-decay [31]. These radionuclides can be labelled to chemical compounds of biological interest, so-called radiopharmaceuticals. Depending on the (patho)physiological process of interest, a specific radiopharmaceutical is administered to a patient. In the patient's body, β^+-decay takes place during which a positron is emitted. This positron combines with a nearby electron followed by an annihilation process in which two so-called annihilation photons are emitted in opposite directions. Using coincidence detection, the annihilation process can be localized somewhere along the straight line joining the two locations of the photon detection. Using advanced reconstruction algorithms, quantitative 3D images of the radiopharmaceutical distribution in the patient's body can be obtained.

Since the introduction of hybrid PET/CT systems in 2001 [32], the integration of PET and CT in one single device has been shown to provide important additional information compared to stand-alone PET and CT or PET/CT carried out using two stand-alone (non-hybrid) systems in combination with software-based co-registration [33, 34]. Apart from improved anatomical localization of PET findings on morphological CT images and improvement of PET attenuation correction, the combination of contrast-enhanced, full diagnostic CT images with PET has been demonstrated to change patient management in specific clinical conditions [35]. In fact, within a decade after the introduction of hybrid PET/CT systems, stand-alone clinical PET devices were no longer commercially available.

In spite of the success of hybrid PET/CT systems, the technique has certain limitations and shortcomings. As full integration of PET and CT, allowing simultaneous acquisi-

tion of both modalities, is inherently difficult, PET and CT scans are acquired sequentially which can result in problematic artefacts or spatial registration errors resulting from intra- and inter-scan patient or organ motion [36]. Moreover, hybrid PET/CT examinations result in an increased patient radiation burden compared to stand-alone PET, in particular when full diagnostic CT imaging is performed [37]. Due to the superior soft-tissue contrast of magnetic resonance imaging (MRI) compared to CT and large variety of MR acquisition sequences resulting in various organ and tissue representations, there are numerous clinical indications where MRI is preferred over CT.

Although the idea of a combined PET/MRI system was already suggested and patented in 1990 [38], human PET/MRI systems capable of simultaneous whole body PET and MRI acquisitions became only commercially available from 2010 [39]. The most important reasons for this delay are the technical challenges encountered in the integration of PET and MRI into a single hybrid system, the initial lack of industrial interest and concerns about the price of hybrid PET/MRI systems [40]. The main technical challenges originate from the mutual interference of the two imaging modalities, the requirement of using compact MRI-compatible PET detectors to be integrated inside the main MRI magnet and the development of MRI-based PET attenuation correction methods [41].

As the performance of photomultiplier tubes is severely degraded by even a weak magnetic field, conventional photomultiplier tube-based PET detectors cannot be used in simultaneous PET/MRI systems. Conversely, placement of conventional PET scanner components inside the magnet bore degrades both the static magnetic field homogeneity and the performance of the MRI gradient system causing image artefacts [42]. The development of compact magnetic field insensitive solid-state photo-detectors (such as avalanche photodiodes and silicon photomultipliers) allowed for direct integration of PET detectors inside the bore of an essentially unmodified MRI system with minimal sacrifice in PET or MRI performance [41].

Quantitative PET imaging requires accurate corrections for photon attenuation and scatter during PET image reconstruction. Whereas PET/CT allows for a straightforward transformation of CT Hounsfield units (HU) to linear attenuation coefficients at 511 keV, MRI-based PET attenuation and scatter correction is more challenging. At present, the most widely adopted PET attenuation and scatter correction techniques implemented in clinical PET/MRI systems are segmentation-based methods in which MR images are segmented into different tissue types to which fixed pre-defined linear attenuation coefficients are assigned [43]. However, standard whole body MRI segmentation-based methods do not allow for the detection of bone resulting in underestimation of the PET radioactivity concentration in bone up to 22.5% [44]. The development of novel MR-based attenuation correction techniques using bone mask pairs has been shown to improve PET/MRI quantification in bone and these techniques are expected to be clinically implemented in the nearby future [45, 46]. Finally, the presence of radiofrequency (RF) MRI coils in the PET field of view can result in significant photon attenuation [47].

For rigid, stationary RF coils, coil attenuation correction using pre-defined CT-based attenuation maps is automatically integrated in the PET image reconstruction algorithm upon detection of the coil. Although for flexible RF surface coils various attenuation correction techniques have been proposed [48, 49], in general these coils are optimized for PET-transparency by stripping the coils from as much of its PET attenuation materials as possible. As further improvements in PET/MRI attenuation correction are essential for accurate diagnosis and treatment monitoring, the application of new improved MRI-based attenuation correction techniques are still investigated [43].

Pre-therapeutic absorbed lesion dose assessment using ^{124}I PET

^{18}F-fluorodeoxyglucose (FDG) is the most used PET tracer nowadays. The physical half-life of 110 minutes of ^{18}F allows for distribution of FDG among nearby PET facilities obviating the need of an on-site cyclotron. In addition, the half-life of ^{18}F is sufficiently long to study organ and tissue glucose metabolism, often affected in many disease types, whilst maintaining the radiation dose to patients at an acceptable level. Finally, the pure β^+-decay (yield: 0.967), low positron energy (0.63 MeV), resulting in a short average positron range in soft-tissue [50], and absence of interfering gamma photons make ^{18}F the ideal radionuclide for quantitative PET imaging.

The last decades, ^{124}I PET(/CT) has been used to investigate iodine metabolism in a quantitative way. With a half-life of 4.18 days, ^{124}I is suitable for PET imaging in DTC. However, unlike ^{18}F, ^{124}I is a far from ideal radionuclide for quantitative PET imaging. Due to its relatively low positron yield of 22.5%, the count rate sensitivity is over 4 times lower compared to ^{18}F. Moreover, as a result of the high energy of the emitted positrons (2.14 MeV, yield 10.7%; 1.54 MeV, yield 11.7 %), the effective spatial resolution of ^{124}I is degraded by 0.5-1.0 mm in soft-tissue compared to ^{18}F [51-53]. Furthermore, emitting a cascade of gamma photons as shown in Figure 1.1, ^{124}I is not a pure positron emitter. In fact, approximately half of all emitted positrons are directly followed by a so-called prompt gamma photon of 603 keV. Since the cascade gamma photon energy is close to the energy of the 511 keV annihilation photons, it falls within the energy window of current PET systems. This results in detection of both random coincidences, due to detection of one or two cascade gamma photons originating from different disintegration events, and true coincidences of one annihilation photon and a prompt gamma photon from the same disintegration, or even a coincidence caused by two cascading high-energy prompt gamma photons. Whereas the random coincidences are accurately corrected for by standard random correction algorithms such as the delayed window technique, the prompt gamma coincidences are not [54]. In fact, it has been shown that the conventionally applied scatter correction algorithms result in an underestimation of the measured ^{124}I radioactivity concentration in the central part of the image due to overestimation of the amount of scatter [55].

Despite these challenges, several expert groups have concluded that quantitation of ^{124}I PET images is feasible [56-60]. Furthermore, compared to ^{123}I and ^{131}I SPECT imaging, ^{124}I PET offers a better image spatial resolution (shown in Figure 1.2) and higher count rate sensitivity. As a result, ^{124}I PET has been used for the application of pre-therapeutic lesion-based dosimetry in radioiodine therapy in DTC [29, 30, 61-63]. However, to date, the only study addressing the dose-response relationship in radioiodine therapy in DTC by means of pre-therapeutic ^{124}I PET/CT in a large number of patients was recently published by Jentzen et al. [64]. In order to globally establish pre-therapeutic ^{124}I PET lesion dosimetry as a valuable prognostic tool in personalized radioiodine therapy in DTC, further clinical investigations and improvements in ^{124}I PET quantification are required.

Intermezzo: Concept of lesion dosimetry in DTC

The term internal dosimetry is often used to describe the science of internal radiation dose assessment. Whereas this term contains the suffix *metry*, implying that the radiation dose is directly determined from measurements, radiation dose assessment resulting from the administration of radiopharmaceuticals is in fact entirely founded in theoretical calculations and models [65].

The principal quantity used to express the amount of radiation that is received by the tissues of a person's body is the absorbed radiation dose *D*, defined as the amount of energy from ionizing radiation deposited per unit mass of tissue and expressed in the international system of units (SI) in Gray (1 Gy = 1 J/kg). Although assessment of the absorbed radiation dose can be rather complicated in practice, the medical internal radiation dose (MIRD) system provides a conceptually simple methodology based on both the physical properties of the radionuclide and biologic distribution data. In this methodology the mean absorbed dose $D(r_k)$ to target organ r_k resulting from radioactivity accumulated in nearby source organs r_h per unit of administered amount of radioactivity A_0 [MBq] is given by [66]

$$D(r_k)/A_0 = \sum_h \tau_h S(r_k \leftarrow r_h), \qquad \text{Eq. 1}$$

with τ_h [s] the residence time defined as the total number of disintegrations $\tilde{A}_h$ [MBq·s] in the source organ per administered unit activity

$$\tau_h = \int_0^\infty \frac{A_h(t)}{A_0} dt = \frac{\tilde{A}_h}{A_0}, \qquad \text{Eq. 2}$$

and $S(r_k \leftarrow r_h)$ [Gy·MBq^{-1}·s^{-1}] the absorbed dose to the target organ r_k per unit cumulated radioactivity in source organ r_h

$$S(r_k \leftarrow r_h) = \frac{C \sum_i y_i E_i \emptyset_i(r_k \leftarrow r_h)}{m_k}, \qquad \text{Eq. 3}$$

with y_i the yield of the emitted radiation type *i* having energy E_i [MeV], $\emptyset_i(r_k \leftarrow r_h)$ the fraction of energy emitted from the source organ r_h that is absorbed in the target organ r_k, m_k [kg] the mass of the target organ and *C* [Gy·kg·MBq^{-1}·s^{-1}·MeV^{-1}] some proportionality constant.

As in ^{131}I radioiodine therapy in DTC, the main part of the absorbed radiation dose is delivered by the so-called non-penetrating β^--particles and the radioiodine distribution is characterized by a high focal lesion uptake and very little uptake in other tissues, the lesion absorbed dose is primarily caused by the self-absorbed dose resulting from the radioiodine activity present in the lesion itself. As a result, equation 1 can be approximated to

$$D(r_k)/A_0 = \tau_k S(r_k \leftarrow r_k). \quad \text{Eq. 4}$$

Under the assumption that ^{124}I and ^{131}I exhibit identical pharmacokinetics, the ^{131}I residence time can be assessed from quantitative ^{124}I PET imaging in which the ^{124}I lesion activity is typically measured 1 and 4-5 days after oral administration. As the physical half-life of ^{124}I (4.18 d) is shorter than the half-life of ^{131}I (8.02 d), the measured ^{124}I radioactivity must be corrected for physical decay

$$A_{131I}(t) = \frac{A_{131I}(t_0)}{A_{124I}(t_0)} A_{124I}(t) e^{(\lambda_{124I} - \lambda_{131I})t}, \quad \text{Eq. 5}$$

with $A_{131I}(t)$ and $A_{124I}(t)$ the ^{131}I and ^{124}I radioactivity at time *t* and λ the decay constant calculated from the physical half-life $T_{1/2}$ by

$$\lambda = \frac{\ln 2}{T_{1/2}}. \quad \text{Eq. 6}$$

Jentzen et al. [67] demonstrated that the residence time τ_k can in good approximation be determined from the 24 and 96 hours ^{131}I uptake after administration using a single exponential fit through both measurements and assuming linear uptake during the first 8 hours after iodine intake as shown in Figure 1.3.

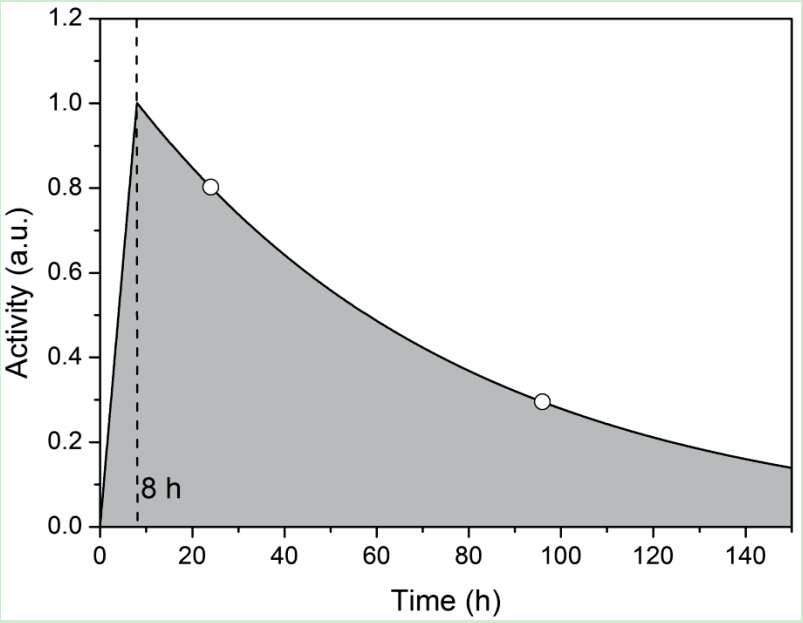

FIGURE 1.3. Iodine residence time determined from the 24-96 hours approach developed by Jentzen et al [67]. The residence time is equal to the area under the curve (grey) divided by the administered amount of radioiodine.

According to equation 2 the residence time τ_k is determined by dividing the (grey) area under the time-activity-curve $\tilde{A}_k$ by the administered amount of radioiodine A_0.

After assessment of the lesion volume, which is in practice often determined from the ^{124}I PET images, the self-absorbed dose per unit cumulated activity $S(r_k \leftarrow r_k)$ can be estimated using the assumption of a spherically shaped lesion, for instance in Olinda [68]. Finally, the lesion absorbed dose during radioiodine therapy is calculated using equation 4.

Radiation protection in radioiodine treatment

Except for the application of personalized radioiodine therapy, dosimetry is also required to assess radiation dose of other people, for instance visitors and personnel, as a result of the exposure to ionizing radiation. Due to the large amounts of radioactivity used in radionuclide therapy, protective measures such as the placement of shielding material in the walls are required to protect people outside the treatment rooms. As the materials used for this shielding (typically lead) are in general rather expensive and heavy, the application of accurate dosimetry methods is essential to achieve an optimal shielding design that fulfills the legal requirements in a cost-effective way. In general,

analytical shielding calculations are performed using the readily available narrow beam linear attenuation coefficients of the shielding material [69, 70] in combination with broad beam buildup factors [71] to account for the contribution of radiation scattered in the shielding material itself. In practice, however, shielding is often only applied to heights below the suspended ceiling resulting in typical shielding heights of 2 – 2.5 m. It was shown that it can be important to take the contribution of ceiling scatter into account for the shielding of X-ray facilities such as CT-scanners [72]. However, data on the contribution of ceiling scatter of γ-radiation commonly encountered in nuclear medicine radionuclide therapy are lacking. Moreover, as the amount of ceiling scatter cannot easily be analytically calculated, the amount of ceiling scatter is often neglected.

Monte Carlo-based modeling has become a widely used technique in radiation protection calculations [73]. In Monte Carlo methods the various interaction processes of ionizing radiation with materials can be modeled from known probability density functions [74]. Simulation of the physical process is then performed by using random sampling from the probability density functions. To obtain accurate calculations, large numbers of individual events (histories) are required. Generally, Monte Carlo simulations allow to study photon interaction effects that cannot easily be determined from direct measurements. For the application of radioprotection, the radiation dose resulting from ionizing radiation traveling over the shielding materials present in the walls and scattering of the ceiling can be determined using Monte Carlo simulations. This allows for cost-effective improved shielding designs in nuclear medicine facilities.

Aim and outline of the thesis

The overall aim of this thesis is to improve radiation dose assessment in radioiodine treatment in DTC, both for the application of personalized patient treatment using quantitative ^{124}I PET imaging and radiation protection of personnel and the general population. With respect to patient management, the application of lesion dosimetry based on pre-therapeutic ^{124}I PET may provide valuable prognostic information and allow for personalized treatment, minimizing the risk of under- or overdosing. From the perspective of radiation protection, accurate dosimetry may result in improved shielding designs in radionuclide therapy facilities and substantially reduce construction costs.

In Chapter 2 an overview of personalized dosimetry approaches and relevant developments for molecular nuclear therapy is presented. Due to the complicated nature of radionuclide therapy, establishment of dose-effect relations require multidisciplinary efforts directed at patient specific techniques, using advanced equipment and (post-)processing. In Chapter 3 the dose-response relationship is retrospectively investigated in DTC patients who underwent radioiodine treatment by means of ^{124}I PET/CT. Using receiver-operating-characteristic curve analysis, the prognostic value for predicting lesion-based ^{131}I therapy response based on ^{124}I PET/CT lesion dose assessment is de-

termined. As ^{124}I PET quantification, and thus lesion dose assessment, is affected by the detected prompt gamma coincidences (PGC) of ^{124}I, different techniques for PGC correction have been developed. In Chapter 4 the influence of PGC correction on ^{124}I PET/CT quantification and dosimetry in DTC is therefore studied in a clinical setting. ^{124}I PET/MRI may become increasingly important for lesion dose assessment in DTC patients. However, compared to ^{124}I PET/CT, in which a relatively straightforward CT-based PET attenuation correction is applied, quantitative ^{124}I PET/MRI is more challenging, in particular for bone. Therefore, in Chapter 5 the quantitative performance characteristics of ^{124}I PET/MRI with the aim of performing lesion-based dosimetry in DTC patients is investigated.

Radiation dose calculations are also important in the shielding design of nuclear medicine examination and treatment rooms. In practice, the shielding in the walls is limited to a height lower than the actual ceiling height and radiation traveling over the shielding material and scattered by the ceiling may result in radiation dose that is often not accounted for in radiation dose calculations. In Chapter 6, the contribution of ceiling scatter to the radiation outside nuclear medicine rooms is determined by means of Monte Carlo simulations.

References

1. International Agency or Research on Cancer, W.H.O., Available from: http://eco.iarc.fr/eucan. 2012.
2. Wiltshire, J.J., et al., *Systematic Review of Trends in the Incidence Rates of Thyroid Cancer.* Thyroid, 2016. **26**(11): p. 1541-1552.
3. Davies, L. and H.G. Welch, *Increasing incidence of thyroid cancer in the United States, 1973-2002.* JAMA, 2006. **295**(18): p. 2164-7.
4. Davies, L. and H.G. Welch, *Current thyroid cancer trends in the United States.* JAMA Otolaryngol Head Neck Surg, 2014. **140**(4): p. 317-22.
5. Morris, L.G. and D. Myssiorek, *Improved detection does not fully explain the rising incidence of well-differentiated thyroid cancer: a population-based analysis.* Am J Surg, 2010. **200**(4): p. 454-61.
6. Cooper, D.S., et al., *Revised American Thyroid Association management guidelines for patients with thyroid nodules and differentiated thyroid cancer.* Thyroid, 2009. **19**(11): p. 1167-214.
7. Gilliland, F.D., et al., *Prognostic factors for thyroid carcinoma. A population-based study of 15,698 cases from the Surveillance, Epidemiology and End Results (SEER) program 1973-1991.* Cancer, 1997. **79**(3): p. 564-73.
8. Durante, C., et al., *Long-term outcome of 444 patients with distant metastases from papillary and follicular thyroid carcinoma: benefits and limits of radioiodine therapy.* J Clin Endocrinol Metab, 2006. **91**(8): p. 2892-9.
9. Dinneen, S.F., et al., *Distant metastases in papillary thyroid carcinoma: 100 cases observed at one institution during 5 decades.* J Clin Endocrinol Metab, 1995. **80**(7): p. 2041-5.
10. Luster, M., et al., *Guidelines for radioiodine therapy of differentiated thyroid cancer.* Eur J Nucl Med Mol Imaging, 2008. **35**(10): p. 1941-59.
11. Silberstein, E.B., *Radioiodine: the classic theranostic agent.* Semin Nucl Med, 2012. **42**(3): p. 164-70.
12. Anger, H.O., *Use of a gamma-ray pinhole camera for in vivo studies.* Nature, 1952. **170**(4318): p. 200-1.
13. Rault, E., et al., *Comparison of image quality of different iodine isotopes (I-123, I-124, and I-131).* Cancer Biother Radiopharm, 2007. **22**(3): p. 423-30.
14. Sherman, S.I., *Thyroid carcinoma.* Lancet, 2003. **361**(9356): p. 501-11.
15. Lassmann, M., et al., *Impact of 131I diagnostic activities on the biokinetics of thyroid remnants.* J Nucl Med, 2004. **45**(4): p. 619-25.
16. Medvedec, M., *Thyroid stunning in vivo and in vitro.* Nucl Med Commun, 2005. **26**(8): p. 731-5.
17. *Council Directive 2013/59/Euratom of 5 December 2013 laying down basic safety standards for protection against the dangers arising from exposure to ionising radiation, and repealing Directives 89/618/Euratom, 90/641/Euratom, 96/29/Euratom, 97/43/Euratom and 2003/122/Euratom.* Official Journal of the European Union, 2014: p. L13/1-L13/73.
18. Stokkel, M.P., *^{131}I therapy for treatment of differentiated thyroid carcinoma*, in *Procedure guidelines of nuclear medicine 2016.* 2016.
19. Lassmann, M., et al., *The use of dosimetry in the treatment of differentiated thyroid cancer.* Q J Nucl Med Mol Imaging, 2011. **55**(2): p. 107-15.
20. Clement, S.C., et al., *Intermediate and long-term adverse effects of radioiodine therapy for differentiated thyroid carcinoma--a systematic review.* Cancer Treat Rev, 2015. **41**(10): p. 925-34.
21. Qu, Y., R. Huang, and L. Li, *Low- and high-dose radioiodine therapy for low-/intermediate-risk differentiated thyroid cancer: a preliminary clinical trial.* Ann Nucl Med, 2017. **31**(1): p. 71-83.
22. Ben Ghachem, T., et al., *A comparison of low versus high radioiodine administered activity in patients with low-risk differentiated thyroid cancer.* Eur Arch Otorhinolaryngol, 2017. **274**(2): p. 655-660.
23. Han, J.M., et al., *Effects of low-dose and high-dose postoperative radioiodine therapy on the clinical outcome in patients with small differentiated thyroid cancer having microscopic extrathyroidal extension.* Thyroid, 2014. **24**(5): p. 820-5.
24. Schlumberger, M., et al., *Strategies of radioiodine ablation in patients with low-risk thyroid cancer.* N Engl J Med, 2012. **366**(18): p. 1663-73.

25. Kulkarni, K., et al., *The relative frequency in which empiric dosages of radioiodine would potentially overtreat or undertreat patients who have metastatic well-differentiated thyroid cancer.* Thyroid, 2006. **16**(10): p. 1019-23.
26. Lassmann, M., et al., *EANM Dosimetry Committee series on standard operational procedures for pre-therapeutic dosimetry I: blood and bone marrow dosimetry in differentiated thyroid cancer therapy.* Eur J Nucl Med Mol Imaging, 2008. **35**(7): p. 1405-12.
27. Maxon, H.R., et al., *Relation between effective radiation dose and outcome of radioiodine therapy for thyroid cancer.* N Engl J Med, 1983. **309**(16): p. 937-41.
28. Maxon, H.R., 3rd, et al., *Radioiodine-131 therapy for well-differentiated thyroid cancer--a quantitative radiation dosimetric approach: outcome and validation in 85 patients.* J Nucl Med, 1992. **33**(6): p. 1132-6.
29. Freudenberg, L.S., et al., *124I-PET dosimetry in advanced differentiated thyroid cancer: therapeutic impact.* Nuklearmedizin, 2007. **46**(4): p. 121-8.
30. Pettinato, C., et al., *Pretherapeutic dosimetry in patients affected by metastatic thyroid cancer using 124I PET/CT sequential scans for 131I treatment planning.* Clin Nucl Med, 2014. **39**(8): p. e367-74.
31. Cherry, S.R. and M. Dahlbom, *PET: Physics, Instrumentation, and scanners*, in *PET Molecular imaging and its biological applications*, M.E. Phelps, Editor. 2004.
32. Beyer, T., et al., *A combined PET/CT scanner for clinical oncology.* J Nucl Med, 2000. **41**(8): p. 1369-79.
33. Bar-Shalom, R., et al., *Clinical performance of PET/CT in evaluation of cancer: additional value for diagnostic imaging and patient management.* J Nucl Med, 2003. **44**(8): p. 1200-9.
34. Antoch, G., et al., *Accuracy of whole-body dual-modality fluorine-18-2-fluoro-2-deoxy-D-glucose positron emission tomography and computed tomography (FDG-PET/CT) for tumor staging in solid tumors: comparison with CT and PET.* J Clin Oncol, 2004. **22**(21): p. 4357-68.
35. Pfannenberg, A.C., et al., *Value of contrast-enhanced multiphase CT in combined PET/CT protocols for oncological imaging.* Br J Radiol, 2007. **80**(954): p. 437-45.
36. Pichler, B.J., et al., *Positron emission tomography/magnetic resonance imaging: the next generation of multimodality imaging?* Semin Nucl Med, 2008. **38**(3): p. 199-208.
37. Huang, B., M.W. Law, and P.L. Khong, *Whole-body PET/CT scanning: estimation of radiation dose and cancer risk.* Radiology, 2009. **251**(1): p. 166-74.
38. Hammer, B.E., *NMR-PET scanner apparatus.* Magn. Reson. Imag, 1990. **9**(4).
39. Delso, G., et al., *Performance measurements of the Siemens mMR integrated whole-body PET/MR scanner.* J Nucl Med, 2011. **52**(12): p. 1914-22.
40. Cherry, S.R., *Multimodality imaging: beyond PET/CT and SPECT/CT.* Semin Nucl Med, 2009. **39**(5): p. 348-53.
41. Vandenberghe, S. and P.K. Marsden, *PET-MRI: a review of challenges and solutions in the development of integrated multimodality imaging.* Phys Med Biol, 2015. **60**(4): p. R115-54.
42. Muzic, R.F., Jr. and F.P. DiFilippo, *Positron emission tomography-magnetic resonance imaging: technical review.* Semin Roentgenol, 2014. **49**(3): p. 242-54.
43. Jung, J.H., Y. Choi, and K.C. Im, *PET/MRI: Technical Challenges and Recent Advances.* Nucl Med Mol Imaging, 2016. **50**(1): p. 3-12.
44. Aznar, M.C., et al., *Whole-body PET/MRI: the effect of bone attenuation during MR-based attenuation correction in oncology imaging.* Eur J Radiol, 2014. **83**(7): p. 1177-83.
45. Paulus, D.H., et al., *Whole-Body PET/MR Imaging: Quantitative Evaluation of a Novel Model-Based MR Attenuation Correction Method Including Bone.* J Nucl Med, 2015. **56**(7): p. 1061-6.
46. Koesters, T., et al., *Dixon Sequence with Superimposed Model-Based Bone Compartment Provides Highly Accurate PET/MR Attenuation Correction of the Brain.* J Nucl Med, 2016. **57**(6): p. 918-24.
47. Delso, G., et al., *Evaluation of the attenuation properties of MR equipment for its use in a whole-body PET/MR scanner.* Phys Med Biol, 2010. **55**(15): p. 4361-74.
48. Eldib, M., et al., *Markerless attenuation correction for carotid MRI surface receiver coils in combined PET/MR imaging.* Phys Med Biol, 2015. **60**(12): p. 4705-17.
49. Paulus, D.H., et al., *Simultaneous PET/MR imaging: MR-based attenuation correction of local radiofrequency surface coils.* Med Phys, 2012. **39**(7): p. 4306-15.

50. Cherry S.R., S.J.A., Phelps M.E, *Physics in nuclear medicine: 3rd edition*. 2003: Elsevier Health Sciences.
51. Kemerink, G.J., et al., *Effect of the positron range of 18F, 68Ga and 124I on PET/CT in lung-equivalent materials.* Eur J Nucl Med Mol Imaging, 2011. **38**(5): p. 940-8.
52. Jentzen, W., et al., *Iodine-124 PET dosimetry in differentiated thyroid cancer: recovery coefficient in 2D and 3D modes for PET(/CT) systems.* Eur J Nucl Med Mol Imaging, 2008. **35**(3): p. 611-23.
53. Gregory, R.A., et al., *Optimization and assessment of quantitative 124I imaging on a Philips Gemini dual GS PET/CT system.* Eur J Nucl Med Mol Imaging, 2009. **36**(7): p. 1037-48.
54. Surti, S., R. Scheuermann, and J.S. Karp, *Correction technique for cascade gammas in I-124 imaging on a fully-3D, Time-of-Flight PET Scanner.* IEEE Trans Nucl Sci, 2009. **56**(3): p. 653-660.
55. Conti, M. and L. Eriksson, *Physics of pure and non-pure positron emitters for PET: a review and a discussion.* EJNMMI Phys, 2016. **3**(1): p. 8.
56. Pentlow, K.S., et al., *Quantitative imaging of iodine-124 with PET.* J Nucl Med, 1996. **37**(9): p. 1557-62.
57. Herzog, H., et al., *PET quantitation and imaging of the non-pure positronemitting iodine isotope I-124.* Applied Radiation and Isotopes, 2002. **56**(5): p. 673-679.
58. Lubberink, M. and H. Herzog, *Quantitative imaging of 124I and 86Y with PET.* Eur J Nucl Med Mol Imaging, 2011. **38 Suppl 1**: p. S10-8.
59. Jentzen, W., *Experimental investigation of factors affecting the absolute recovery coefficients in iodine-124 PET lesion imaging.* Phys Med Biol, 2010. **55**(8): p. 2365-98.
60. Preylowski, V., et al., *Is the image quality of I-124-PET impaired by an automatic correction of prompt gammas?* PLoS One, 2013. **8**(8): p. e71729.
61. Flower, M.A., et al., *Radiation dose assessment in radioiodine therapy. 2. Practical implementation using quantitative scanning and PET, with initial results on thyroid carcinoma.* Radiother Oncol, 1989. **15**(4): p. 345-57.
62. Erdi, Y.E., et al., *Radiation Dose Assessment for I-131 Therapy of Thyroid Cancer Using I-124 PET Imaging.* Clin Positron Imaging, 1999. **2**(1): p. 41-46.
63. Sgouros, G., et al., *Patient-specific dosimetry for 131I thyroid cancer therapy using 124I PET and 3-dimensional-internal dosimetry (3D-ID) software.* J Nucl Med, 2004. **45**(8): p. 1366-72.
64. Jentzen, W., et al., *Assessment of lesion response in the initial radioiodine treatment of differentiated thyroid cancer using 124I PET imaging.* J Nucl Med, 2014. **55**(11): p. 1759-65.
65. Stabin, M.G., *Fundamentals of Nuclear Medicine Dosimetry*. 2008: Springer Science+Business Media.
66. Loevinger, R., T.F. Budinger, and E.E. Watson, *MIRD Primer of Absorbed Dose Calculations*. 1988, New York: Society of Nuclear Medicine.
67. Jentzen, W., et al., *Optimized 124I PET dosimetry protocol for radioiodine therapy of differentiated thyroid cancer.* J Nucl Med, 2008. **49**(6): p. 1017-23.
68. Stabin, M.G., R.B. Sparks, and E. Crowe, *OLINDA/EXM: the second-generation personal computer software for internal dose assessment in nuclear medicine.* J Nucl Med, 2005. **46**(6): p. 1023-7.
69. Shleien, B., L. Slaback, and B. Birky, *Handbook of Health Physics and Radiological Health*. 1998, Baltimore: Lippincott Williams & Wilkins.
70. Berger, M.J., et al. *XCOM: Photon Cross Section Database (version 1.5)*. 2010; Available from: http://physics.nist.gov/xcom.
71. Shimizu, A., T. Onda, and Y. Sakamoto, *Calculation of Gamma-Ray Buildup Factors up to Depths of 100 mfp by the Method of Invariant Embedding.* J Nucl Sci Technol, 2004. **41**: p. 413-424.
72. Martin, C.J., et al., *Derivation of factors for estimating the scatter of diagnostic x-rays from walls and ceiling slabs.* J Radiol Prot, 2012. **32**(4): p. 373-96.
73. Zaidi, H., *Quantitative Analysis in Nuclear Medicine Imaging*. 2006, New York: Springer Science + Business Media, Inc.
74. Ljungberg, M., S.E. Strand, and M.A. King, *Monte Carlo Calculations in Nuclear Medicine, second edition, Appliations in Diagnostic Imaging*. 2013, Boca Raton: Taylor & Francis Group, LLC.

Chapter 2

Dosimetry in molecular nuclear therapy

R. Wierts, C.D.J.M. de Pont, B. Brans, F.M. Mottaghy, G.J. Kemerink

Methods. 2011 Nov;55(3): 196-202. doi: 10.1016/ymeth.2011.09.016

Abstract

Advanced personalized dosimetry for molecular nuclear therapy has been shown to be feasible in clinical practice. At the same time instrumentation and dosimetric software are still evolving at a high pace. Procedures developed so far differ in approach and sophistication, and standard operating procedures necessary for accurate specific dosimetry do not yet exist. For this reason we restricted ourselves to reviewing the literature and highlighting relevant developments.

Introduction

Dosimetry in molecular nuclear therapy is still greatly in development. The number of cases where biological outcome correlates with calculated dose has risen promisingly (see e.g. the reviews by Stabin [1] and Bardiès and Buvat [2]), after a long period in which such correlations hardly appeared existent [3]. These findings, the growing application of molecular nuclear therapy, and the success of dosimetry in external beam radiotherapy, explain the current interest in the subject and emphasize the importance of further efforts to improve dosimetry in radionuclide therapy.

Dosimetry basically entails two steps, first, the determination of the spatial distribution of the radionuclide in the patient as a function of time, and second, the use of this distribution in the calculation of the distribution of the absorbed or biologically effective dose (BED). No generally accepted approach has yet been developed, and large differences exist in the dosimetric methods and their degree of sophistication [2, 4]. Planar scintigraphy, SPECT/CT and PET/CT are all used for the acquisition of images for deriving activity distributions [5-8]. Many computer codes have been developed for the calculation of dose distributions. Some are very fast and based on simple mathematical phantoms, not necessarily representative for the individual patient, others are highly accurate but time consuming, using personalized Monte Carlo simulations taking the patient's own anatomy into account [4, 9, 10].

In analogy to the personalized approach in external beam dosimetry, it is to be expected that radionuclide dosimetry will also only reach its ultimate potential when accurate 3D-activity distributions and the patient's own anatomy are used in the dose calculations [4, 11-13]. In fact a personalized approach is required by the EURATOM 97/43 directive [14], but is too rarely implemented today. According to Stabin [15] generic models for patients may result in dose estimates that are off by a factor of at least 2, whereas by using optimized personalized methods the uncertainty can be reduced to a value of perhaps 10-20%. The accuracy needed to predict biological outcome – on the one hand tumour control and on the other toxicity to organs at risk – still needs to be investigated.

As no real standard methods exist, we will discuss relevant components of molecular nuclear therapy, and try to give sufficient insights into the literature.

What is known on radionuclide dosimetry: basic literature

A classic source of techniques for the quantitative assessment of activity distributions is MIRD pamphlet no. 16 from 1999 [16], in which emphasis is still on planar imaging techniques. A general introduction to dosimetry for molecular nuclear therapy, based on the MIRD schema, is given by Stabin [17]. Two other relevant documents are the "EANM Dosimetry Committee guidance document: good practice of clinical dosimetry

reporting" [18] and "MIRD pamphlet no. 21: a generalized schema for radiopharmaceutical dosimetry – standardization of nomenclature" [19]. The theory of a dosimetric model which also considers the effects of protracted exposure and varying dose rate, which are characteristics of radionuclide therapy, can be found in the work of Dale [20, 21].

Nearly the complete field of radionuclide therapy was recently covered in reviews in a single issue of the Quarterly Journal of Nuclear Medicine and Molecular Imaging [2, 22-30].

Determination of the activity distribution as a function of time

Independent of the imaging technique to be applied, decisions have to be made with respect to the number and the timing of image acquisitions after administration of the activity to the patient. The criterion is that the number of radioactive decays that occurred in any organ (or voxel) in the patient can be determined to a sufficient degree of accuracy.

In many studies the number of time points is restricted to three for practical reasons. Some studies showed that in special cases two [31] or even one [32] point in time could provide dosimetric results comparable to those of more elaborate sampling schemes. In fact the number of points required depends on the pattern in which the activity increases and decreases in the patient's organ or tissue after administration. Often this pattern can be described by a sum of exponential functions, and the number of data points should at least be twice the number of exponentials needed in the fit. Compartmental modelling can be advantageous [16, 23]. MIRD pamphlet 16 advises to use "one or two data points taken at some fraction of T_e; one near $T_{e;}$ and one or two other data points taken a ~3 × T_e and 5 × T_e", with T_e the effective half-time of the decrease of the radioactivity in the patient. Instructive considerations on the timing of sampling are given in Appendix D of MIRD pamphlet 16 [16].

Image acquisition: PET/CT

In principle, clinical PET/CT systems today have the highest potential for accurately determining three dimensional activity distributions in patients [7]. PET scanners have a sensitivity that is of the order of 100 times higher than that of a gamma camera (see e.g. Rault et al. [33]), and the corrections necessary for the various imperfections inherent in the PET-technology, i.e. attenuation, scattered radiation, random coincidences, variations in individual detector element sensitivity and dead time, have been implemented by all manufacturers. The high sensitivity allows the implementation of a good spatial resolution of about 5-7 mm and short acquisition times of a few minutes per bed

position. Whole body scanning is possible, even repeatedly as generally necessary for dosimetry. The CT-data, by the scanner's hybrid design co-registered with the PET data, also facilitate image registration of scans at different time points.

For the successful application of PET/CT in radionuclide therapy one needs a pair of nuclides with the following properties: (i) one nuclide is suitable for therapy and the other for PET, and (ii) after coupling to the pharmaceutical to be used in imaging and therapy, the two radiopharmaceuticals have biologically identical properties or identical distributions. This will automatically be the case if both nuclides are of the same element, but this is not a necessary condition. The lack of such pairs limits the use of PET/CT. The most favourable combination currently is that of the widely therapeutically used ^{131}I and the positron emitter ^{124}I. For dosimetric studies ^{124}I has a conveniently long half-life of 4.176 days, but it suffers from a relatively low positron abundance of 23% and the presence of additional gamma radiation (mainly of 603 keV) which is partially in coincidence with positron emission. Coincidences between gammas exist too, for instance between the 603 and 723 keV gammas [34]. The quantification of activity in ^{124}I PET(/CT) has been studied in considerable detail [9, 13, 22, 35-41].

Another suitable therapy-PET imaging pair is ^{90}Y and ^{86}Y, where ^{90}Y is a nearly pure β^-emitter, with maximum β-energy of 2.26 MeV [34]. PET using ^{86}Y has been studies by several authors [37, 38, 41-43]. Recently, also the presence of internal positron-electron pair production in ^{90}Y itself was utilized for patient imaging [44, 45]. The internal pair production, of which the positron is the relevant particle, has a probability of $(31.86 \pm 0.47) \times 10^{-6}$ [46]. This phenomenon might especially be used to verify the activity distribution after administration of large amounts of activity for therapy, e.g. after selective internal radiotherapy using resin or glass spheres. Other therapy-PET pairs are ^{67}Cu-^{64}Cu, and ^{89}Sr-^{83}Sr [47].

The problem of the presence of additional gammas in ^{124}I and ^{86}Y can be overcome [37, 41]. These radiations result in a uniform background in the sinogram, which, at least for ^{124}I is already rather well removed by the standard single scatter simulation correction algorithm [22, 48, 49]. The result of the scatter simulation is scaled with the tails of the sinogram, and this step, although not strictly correct for removing a constant background, accounts for the elimination of gamma-annihilation coincidences [22], probably even causing some overcorrection [41]. The delayed-window random coincidence correction also takes care of the random gamma-gamma coincidences. Narrowing the energy window around 511 keV within which gamma radiation is accepted, might also help to improve both image quality and quantification by reducing the contribution of 603 keV gamma events [37, 50].

The 3D-activity distributions obtained are used for the calculation of the absorbed dose and other dose parameters. When the classical MIRD scheme is to be applied, organ volumes of interest (VOIs) have to be defined around all source organs, and the activities as a function of time within these VOIs have to be derived. VOIs can be defined either on PET or CT, or on an overlay of both. This generally only has to be done at

one time point, as the VOIs can be copied to the other image sets. Before copying the VOIs to the PET images, these should be co-registered by using e.g. the low-dose CT data sets. Small shifts of VOIs may still be necessary. Alternatively one could also shift all VOIs without image co-registration. Normalized time activity curves have to be calculated for all organs and tissues of interest by dividing the activity in a given VOI by the activity given to the patient.

When using a (personalized) voxel model in the calculations, the image sets must again be co-registered carefully to ensure that a certain voxel in image space corresponds with the same piece of tissue at the different time points. In this way normalized time activity curves per voxel become available. These can be used as input for personalized dose calculations, using CT data as a personal template for the patient. VOI definition is in principle only necessary for the target organs including tumours, on the one hand to define radiobiological parameters for that organ, on the other hand to be able to evaluate to dosimetric results (e.g. the dose-volume histogram) within the target [13, 20, 21, 23, 51, 52].

Image acquisition: SPECT/CT

It has been shown in many phantom studies that SPECT/CT allows a relatively accurate absolute quantification of activity [53-62], typically within about 10-20%. CT-based corrections for attenuation and scatter, and some resolution recovery by modelling the detector response and collimator properties, have been implemented by all major vendors.

Due to the lower sensitivity of a gamma camera, acquisition times in SPECT mode are long, in clinical practice probably too long for single or repeated whole body acquisitions. This remains true even if the acquisition time would be halved, as has been shown to be possible for dosimetry [63]. Hybrid acquisition solutions have been proposed to overcome these long scan times [62, 64]. In the hybrid approach one or more SPECT studies are made at one point in time, and at all other time points only conjugate view planar images are acquired. Using the 3D-information from the SPECT or CT acquisition, volumes of interest can be defined around all source organs and tissues of interest. Assuming that at all times the activity distribution within a given VOI is uniform, the actual concentration can be estimated in an iterative process. The activity in the VOIs, in the to-be-reconstructed image at the times where the 3D-information is missing, is iteratively adjusted until the projections match the measured planar images. Alternatively one can assume that the activities in a VOI at different points in time only differ by a scaling factor. In this reconstruction process, corrections for attenuation, scatter and system limitations can be implemented. In computer simulations and phantom studies the results were very similar to those obtained in a full SPECT study [62, 64]. However,

in patient studies the distribution pattern of the activity within an organ or tumour might change over time.

Normalized time activity curves can be reconstructed in the same way as described for PET/CT. Effects of small changes in size and position of volumes of interest on activity estimation have also been studied by He and Frey. In their simulations the effects were of limited magnitude, and largest for small organs [65].

Image acquisition: planar whole body scintigraphy

Whole body imaging using a conjugate pair of detectors of a gamma camera [16] is even today probably the mainstay of image acquisition for dosimetry. Whole body acquisition can be performed relatively fast, typically in about 10-20 min. Many implementations for the analysis of the images exist, which differ in the way in which the various corrections that are required for absolute quantification of activity are realized. Many details can be found in MIRD pamphlet 16 [16] and the work of Geworski et al. [8].

Attenuation correction can be done by means of a transmission scan using a flood source with activity of the radionuclide used for dosimetry, in combination with a blank scan to define 100% transmission. Alternatively, the thickness of the patient can be estimated, and together with an experimentally determined effective attenuation coefficient, be used for attenuation correction. In the latter approach scatter correction is then taken into account by an attenuation correction that is lower than the narrow-beam value. Scatter correction can also be performed using the double or triple energy-window method.

A method for the non-trivial correction for dead time (or count loss) during whole body scanning with a continuously moving bed, as might be necessary for patients receiving high therapeutic activities, has been proposed by Hobbs et al. [66].

There are several shortcomings inherent in the whole body conjugate view method. Corrections for scatter and attenuation are only approximate, and there are the problems of organ-overlap and properly choosing a background region to correct for overlying tissue. Many studies have shown that the accuracy of this planar method is poor [55, 56, 62, 64, 67-71]. Note that in the studies of He et al. [56, 64] a relatively simple version of the whole body method was applied. Remarkably, more satisfactory findings were reported in a number of older studies [72-74]. The current consensus appears to be that the planar approach is not suitable for therapy, but that the limited accuracy might be acceptable for the evaluation of general dosimetric properties of radiopharmaceuticals (like biodistribution and organ and effective dose per unit of activity).

More recently, several improvements of the conjugate view technique have been tested, generally involving special reconstruction software. One is to use a single set of 3D image data, e.g. from CT, for defining volumes of interest around all organs and tissues of interest, as proposed by He et al. [56, 64]. By assuming uniform activity in all

VOIs, and taking system properties into account, one can iteratively estimate the activities in the various VOIs from the conjugate anterior and posterior images by using a suitable reconstruction algorithm, as was already explained above for a hybrid planar/SPECT method. The assumption of uniform activity distributions remains a limitation. The accuracy appears to be limited especially for small organs. The effect of misregistration of volumes of interest has been investigated by Song et al. [75].

Determination of the residence time

Once sets of images with an estimate of the activity in the patient have been calculated at different time points, quantification of activity in all relevant organs and tissues has to be performed. Alternatively, activity can be assessed at the voxel level. The choice depends on the method to be applied for the dose calculation. The residence time for an organ or voxel is obtained by integration over time of the normalized time activity curve. Effectively it is the hypothetical time that a source of constant strength, with the activity equal to what is administered to the patients, has to stay at that location to provide as many disintegrations as the actually present, over-time-varying activity did.

In some cases it may be possible to use a known biokinetic model and determine the model parameters from several time activity curves together (e.g. from blood and some organs). The fitted model parameters can be used to calculate the time activity curves in the various compartments (e.g. organs), and from those curves the corresponding residence times can in turn be calculated.

MIRD pamphlet 16 [16] in its Appendix D considers when potential errors may be introduced: (i) uptake is not instantaneous whilst assuming is was, (ii) a fast wash-out component is missed due to undersampling, and (iii) the long-term retention is not completely determined. Appendix E of the pamphlet gives calculational examples for these cases. Flux et al. [76] described how to estimate uncertainties in absorbed dose calculations due to inconsistent or inaccurate activity retention measurements.

Calculation of absorbed dose or biological effective dose (BED) for molecular therapy

The simplest approach applied in radionuclide therapy is not to perform any dosimetry at all, a procedure that might be characterized as “one dose fits all”. This is, for instance, still applied in many places in the radioiodine treatment of thyroid disorders. The activity given to a patient for one and the same disease may also differ greatly between institutions. There is also no dosimetry advised for the treatment of lymphoma using ^{90}Y Zevalin. Note that this is against European guidelines which require individualized do-

simetry [14]. Moreover, many authors have given convincing arguments for a personalized approach [1, 11, 12, 77].

Absorbed dose calculations over the years have been performed using the MIRD methodology as implemented in the Mirdose program [78], and more recently, in its successor Olinda/EXM [79]. These software codes take the residence times of activity in all source organs as input. Both have models for anthropomorphic phantoms of different age and sex, as well as models of pregnant woman at 3, 6 and 9 month pregnancy.

Olinda/EXM allows for adjustment of organ mass, however, this adjustment is only used to adapt the self-dose. It also has a module for the estimation of the self-dose of spherical tumours.

Radiobiological modelling was introduced in radionuclide therapy, as in external beam therapy, to account for dose rate and tissue repair effects [4, 20, 21, 23]. Central to this approach are the parameters α and β, the coefficients of the linear and quadratic dose terms in the linear-quadratic dose response model, and μ, the time constant characterizing tissue repair (instead of μ an effective half-time $t_e = \ln(2)/\mu$ may be seen). The model permits the calculation of a hypothetical reference dose for any practical exposure, the so-called biologically effective dose (BED), which, given with a very low dose-rate or in infinitely small dose fractions, would have the same biological effect as the actual exposure. This model allows for instance the use of data from external beam therapy to estimate the effect of radionuclide therapy (or vice versa). For a tissue consisting of similar units ("parallel organization", or "function scaling with size"), as in e.g. the liver or possibly a tumour, the BED-distribution allows the calculation of an equivalent uniform dose (EUD), the uniform dose that would have to be given to the organ or tumour to give the same effect (e.g. cell killing or organ failure) as the actual non-uniform distribution would do.

For the determination of organ doses and the effective dose of a radiopharmaceutical for diagnostic imaging, the MIRD approach as implemented in Mirdose/Olinda is believed to give an acceptable accuracy, notwithstanding the fact that a patient's anatomy generally will not match with that of one of the phantoms. In therapy a higher accuracy is required which cannot be guaranteed by this standard approach. Marine et al. [80] calculated specific absorbed fractions (SAFs) for adults with statures between the 10^{th} and 90^{th} percentile of the general population. Differences in SAFs amounted up to 15-30% for self-irradiation of organs in the trunk, and were up to about 8-33% for organs irradiating other organs. In another study by Divoli et al. patient specific SAFs were calculated with OEDIPE [81] and compared with the SAFs from Olinda/EXM. Relatively large differences were found as well, but when organ mass was correctly taken into account in Olinda/EXM, the differences were smaller than 26%. These authors also showed that using a dose kernel derived for water density can result in large errors of up to 60% in the calculated absorbed dose in the lungs. Clark et al. showed that obesity had a very small effect on SAFs, only in the abdomen did mesenteric adipose tissue increase the distance between organs and lower the SAFs [82].

Using 3D-information, available from PET/CT or SPECT/CT, patient specific dose calculations have been performed by several groups. Several methods can be distinguished, but they all rely in some way or another on Monte Carlo simulations: (i) SAF-based methods, (ii) dose kernel methods, and (iii) Monte Carlo calculations for the individual patient. SAF-based methods apply either fixed mathematical phantoms, or they are voxel based, but then they pertain to soft-tissue only. A dose kernel describes the absorbed dose as a function of the distance of a point source. Kernel methods derive absorbed dose distributions by the convolution of a dose kernel and the patient's activity distribution [83]. The commercially available Stratos software, which is part of the translational and research workstation Imalytics (Philips Technology GmbH, Aachen, Germany), is also based on this approach. Stratos includes tools for segmentation, image co-registration, 3D visualization, fusion display, and the calculation of dose tables and dose volume histograms. It will support hybrid imaging [84]. The disadvantage of the kernel approach is that is does not easily allow taking local differences in tissue (in composition and density) into account, e.g. between soft-tissue, lung and bone. Loudos et al. [85] described a kernel method in which these density differences are taken into account to some extent.

Several groups have developed different 3D software packages: 3D-ID/3D-RD by the group at Johns Hopkins [51], now based on EGS and including biological dose modelling and already used in clinical applications; RMDP from the Royal Marsden group, uses either beta kernels or voxel SAFs, and includes a routine to simulate photon interactions in a collimator and the gamma camera crystal [86]; DOSE3D from the Institut Gustave-Roussy uses the EGS4 Monte Carlo code to calculate doses for anthropomorphic phantoms with organs whose shape can be changed and to which spheres can be added [87, 88]; OEDIPE uses MCNP to calculate either doses at the organ or voxel level [81, 89, 90]; MINERVA is an extension to the external beam treatment planning program PEREGRINE developed at Lawrence Livermore National Laboratory, and includes tools for radionuclide therapy [91, 92].

Personalized dosimetry using 3D PET/CT or SPECT/CT data is still an area of active research, and it still may take some time before a widely accepted standard package has found its way to the users who now still apply Olinda/EXM or refrain from any form of dosimetry at all.

Dosimetry of organs at risk

When trying to maximize the dose to tumour tissue, a limit to the maximum activity that can be given to a patient is usually set by toxicity to a critical organ, often the red marrow or the kidney. For organs containing a tumour, like the liver or the lung, the host organ itself could also be the critical organ. Estimation of an acceptable dose is

complicated because radiation tolerance in radionuclide therapy varies among individuals, with influence of genetic makeup, age and previous therapies.

Meredith et al. reviewed the risks to normal tissue from radionuclide therapy [93]. They noted that the tolerance of normal tissue often appeared to be greater than in external beam radiotherapy, but at the same time more variable. These findings were largely attributed to differences in dosimetry methodology and to heterogeneous dose distributions of the radionuclides. They further pointed out the importance of an individualized approach, the application of radiobiological modelling and the use of dose-volume histograms. The latter are relevant because toxicity is not only dependent on dose, but also on the relative volume that receives a given dose. In addition, Meredith et al. provided a valuable overview with a comparison of normal organ radiation tolerance for external beam and beta-emitter radionuclide therapy.

Red marrow

Red marrow is widely distributed over the skeleton, its amount and distribution change with age, and it has a complicated microstructure which also changes over time. These characteristics cause red marrow dosimetry to be complicated [94]. At the same time it is the most radiosensitive tissue in the body, making red marrow dosimetry often necessary in radionuclide therapy.

The method for determining the dose to the red marrow depends on the distribution of the radiopharmaceutical used [95]. Decisive is whether there is specific binding of activity in the red marrow or bone, either by normal physiology or by pathology. If no activity is specifically bound, the activity in the red marrow is due to activity in the blood plasma or blood cells (or both), and blood-based dosimetry can in principle be performed. Instead of applying such blood-based dosimetry, whole body dosimetry has been used in some cases for the prediction of red marrow toxicity as well [96, 97]. If activity is bound to marrow or bone, imaging-based methods are normally applied [98].

Several authors assessed available methods to estimate red marrow dose. Wessels et al. [99] performed a multi-institutional comparison of blood-based models [100], finding a mean ratio of 0.920 ± 0.259 for dose estimates according to the participating institutions compared with the central laboratory value. Hindorf et al. evaluated seven methods, of which four blood-based techniques, a method based on the imaging of the sacrum, and two total body approximations, to obtain estimates of the red marrow dose [101]. The ratio of the maximum and the minimum absorbed dose to red marrow, calculated using the four blood and sacral imaging methods for one and the same patient, varied between 1.8 and 2.8. Ferrer et al. studied two blood-based methods and a lumbar vertebrae imaging-based method and found that doses from imaging predicted haematological toxicity best [102]. A risk of using blood-based methods is the underestimation of the red marrow dose due to bound activity that goes undetected. Even

small amounts of e.g. ^{90}Y bound in the marrow can increase the absorbed dose substantially [103, 104].

Although quantification of the red marrow dose is of limited accuracy at present, standardization of dose assessment methods has its value as it allows comparison of results from different institutions. In this light, guidelines from professional societies are very important. The EANM issued two documents, "EANM Dosimetry Committee guidelines for bone marrow and whole-body dosimetry" [95], and "Blood and bone marrow dosimetry in differentiated thyroid cancer therapy" [105]. The reader is referred to these detailed documents for all practical information needed for performing bone marrow dosimetry in clinical practice. Both guidelines allow for some patient specific adjustments (e.g. based on weight or bone marrow mass), but as discussed by Hindorf et al. this could be taken further to 3D-measurements using PET/CT or SPECT/CT imaging and patient specific voxel-based calculations [95].

Hindorf et al. [95] state "Demonstration of the relationships between absorbed dose and biological effect for bone marrow toxicity from radionuclide therapy have proven elusive, although it is likely that these exist for radionuclide therapy also". In part this lack of correlation will be due to inaccuracies in the difficult dosimetry, but two additional points with respect to this dosimetry still have to be considered here. In most of the literature on red marrow dosimetry cited above only the absorbed dose is considered, not the biologically effective dose as should be. However, Baechler et al. showed that for four commonly applied radionuclides and normal therapy conditions the BED and the absorbed dose are nearly identical for red marrow [106]. The BED formalism may thus be of limited relevance for red marrow dosimetry (but not taken into account in their study was cell repopulation as might occur in the fast responding red marrow [106]). Further, many authors attribute the poor correlation between red marrow or whole body dose and the commonly used indicators for bone marrow suppression, like thrombocytopenia, leukopenia and neutropenia, at least in part to the damage to red marrow cells and their micro-environment caused by previous treatments [107, 108]. This is corroborated by Siegel et al., who reported improved correlations between haematological toxicity and bone marrow dose if the plasma FLT3-L cytokine level – considered as a marker of radiosensitivity – was taken into account [109].

Kidney

The kidney is generally the organ most at risk in peptide receptor radionuclide therapy (PRRT), as low molecular-weight radionuclide conjugates are mainly excreted by the kidney where a fraction is reabsorbed, causing potentially high doses locally [27, 110, 111]. This uptake can be reduced to some extent by the co-infusion of certain amino-acids (lysine, arginine), albumin fragments or Gelofusin, depending on the peptide used for therapy [112].

Dosimetry is commonly based on the MIRD approach. A very large variability in kidney toxicity was observed when the traditional approach was applied whereby the kidney is considered a single unit with a uniform uptake of activity. To improve accuracy, patient specific kidney mass, the locoregional distribution of the radioactivity retained, transit times through the kidneys, and dose rate effects should be taken into account [113]. Other factors affecting kidney radiation toxicity which may be more difficult to take into account are hypertension, diabetes, age, chemotherapy and loss of renal function [112, 114].

In 2003 MIRD-pamphlet 19 appeared in which six age-dependent multiregion models for the kidney were presented [115], including specific absorbed fractions for dosimetric calculations. The regions distinguished were the renal cortex, the medullary pyramids, the papillae and the renal pelvis. For ^{90}Y-compounds used in adults, the absorbed dose to the renal cortex was about 1.29 times the dose predicted by the single-kidney region model, while the dose to the medulla was 0.26 times that for the single-kidney dose. High quality imaging, preferably 3D, is required for the application of this approach. One PET-based method, applied to ^{90}Y PRRT but probably also useful for other PET nuclides, was described by Walrand et al. [116].

For the kidney, biological modelling is important under the circumstances that are typical for radionuclide therapy. This was shown using the linear-quadratic (LQ) model [106, 113, 117], and a model based on time-dose fractionating (TDF) [118]. MIRD pamphlet 20 gives instructive examples for the LQ model. Improved correlation between radiation dose and toxicity was obtained after biological modelling had been introduced and functional differences in the kidney had been taken into account [119].

Current challenges

In comparison to dosimetry for external beam radiotherapy, radionuclide dosimetry faces several additional challenges. First the quantification of the source of radiation, i.e. the activity distribution, is affected by the finite spatial resolution of current nuclear medicine imaging equipment. Activity recovery-coefficients for spheres or ellipsoids with volumes of about 1 cm^3 are substantially below one, even with PET [39]. Small-scale activity inhomogeneities remain undetected, implying that the activity distribution in small irregular structures of e.g. a tumour will be unknown. Depending on the radiation emitted by the radionuclide used for therapy, small scale inhomogeneities can have a large effect on the local absorbed dose [120, 121]. There are still additional issues related to microdosimetry, especially when the therapeutic nuclide emits low-energy electrons or α-particles [15, 122, 123]. Another potential problem is the high amount of activity used in therapy affecting the binding properties of the target, causing another biodistribution than previously observed after administration of the small amount of activity for dosimetry. Finally, pretargeted radioimmunotherapy [124], combinational

therapy, for instance with two different targeting radiopharmaceuticals [125], or with a targeting radionuclide and external beam therapy [126, 127], are still largely unexplored fields.

Conclusion

Dosimetry in molecular nuclear therapy is currently a field of very active research. Given the complicated nature of radionuclide therapy, multidisciplinary efforts should be directed at patient specific techniques, using the most advanced instrumental and numerical methods available. Only then may it be possible to establish useful dose-effect relations in molecular nuclide therapy.

Acknowledgment

The authors thank Dr. A.J. van der Molen, Leiden University Medical Center, for his assistance in gathering part of the relevant literature.

References

1. Stabin, M.G., *Update: the case for patient-specific dosimetry in radionuclide therapy.* Cancer Biother Radiopharm, 2008. **23**(3): p. 273-84.
2. Bardies, M. and I. Buvat, *Dosimetry in nuclear medicine therapy: what are the specifics in image quantification for dosimetry?* Q J Nucl Med Mol Imaging, 2011. **55**(1): p. 5-20.
3. Brans, B., et al., *Clinical radionuclide therapy dosimetry: the quest for the "Holy Gray".* Eur J Nucl Med Mol Imaging, 2007. **34**(5): p. 772-86.
4. Sgouros, G., et al., *Three-dimensional imaging-based radiobiological dosimetry.* Semin Nucl Med, 2008. **38**(5): p. 321-34.
5. Stabin, M.G. and A.B. Brill, *State of the art in nuclear medicine dose assessment.* Semin Nucl Med, 2008. **38**(5): p. 308-20.
6. Stabin, M.G. and G.D. Flux, *Internal dosimetry as a tool for radiation protection of the patient in nuclear medicine.* Biomed Imaging Interv J, 2007. **e28**.
7. Flux, G., et al., *The impact of PET and SPECT on dosimetry for targeted radionuclide therapy.* Z Med Phys, 2006. **16**(1): p. 47-59.
8. Geworski, L., et al., *Physical aspects of scintigraphy-based dosimetry for nuclear medicine therapy.* Nuklearmedizin, 2010. **49**(3): p. 85-95.
9. Sgouros, G., et al., *Three-dimensional radiobiological dosimetry (3D-RD) with 124I PET for 131I therapy of thyroid cancer.* Eur J Nucl Med Mol Imaging, 2011. **38 Suppl 1**: p. S41-7.
10. Tsougos, I., et al., *Patient-specific internal radionuclide dosimetry.* Nucl Med Commun, 2010. **31**(2): p. 97-106.
11. Thierens, H.M., M.A. Monsieurs, and K. Bacher, *Patient dosimetry in radionuclide therapy: the whys and the wherefores.* Nucl Med Commun, 2005. **26**(7): p. 593-9.
12. Flux, G., et al., *Clinical radionuclide therapy dosimetry: the quest for the "Holy Gray".* Eur J Nucl Med Mol Imaging, 2007. **34**(10): p. 1699-700.
13. Hobbs, R.F., et al., *124I PET-based 3D-RD dosimetry for a pediatric thyroid cancer patient: real-time treatment planning and methodologic comparison.* J Nucl Med, 2009. **50**(11): p. 1844-7.
14. *Health protection of individuals against the dangers of ionising radiation in relation to medical exposure: Council Directive 97/43 EURATOM 1997.*
15. Stabin, M.G., *Uncertainties in internal dose calculations for radiopharmaceuticals.* J Nucl Med, 2008. **49**(5): p. 853-60.
16. Siegel, J.A., et al., *MIRD pamphlet no. 16: Techniques for quantitative radiopharmaceutical biodistribution data acquisition and analysis for use in human radiation dose estimates.* J Nucl Med, 1999. **40**(2): p. 37S-61S.
17. Stabin, M.G., *Fundamentals of nuclear medicine dosimetry*. 2008, New York: Springer.
18. Lassmann, M., et al., *EANM Dosimetry Committee guidance document: good practice of clinical dosimetry reporting.* Eur J Nucl Med Mol Imaging, 2011. **38**(1): p. 192-200.
19. Bolch, W.E., et al., *MIRD pamphlet No. 21: a generalized schema for radiopharmaceutical dosimetry--standardization of nomenclature.* J Nucl Med, 2009. **50**(3): p. 477-84.
20. Dale, R.G., *The application of the linear-quadratic dose-effect equation to fractionated and protracted radiotherapy.* Br J Radiol, 1985. **58**(690): p. 515-28.
21. Dale, R.G., *Dose-rate effects in targeted radiotherapy.* Phys Med Biol, 1996. **41**(10): p. 1871-84.
22. Jentzen, W., L. Freudenberg, and A. Bockisch, *Quantitative imaging of (124)I with PET/ CT in pretherapy lesion dosimetry. Effects impairing image quantification and their corrections.* Q J Nucl Med Mol Imaging, 2011. **55**(1): p. 21-43.
23. Konijnenberg, M., *From imaging to dosimetry and biological effects.* Q J Nucl Med Mol Imaging, 2011. **55**(1): p. 44-56.
24. Lassmann, M., et al., *The use of dosimetry in the treatment of differentiated thyroid cancer.* Q J Nucl Med Mol Imaging, 2011. **55**(2): p. 107-15.

25. Flux, G.D., et al., *Clinical applications of dosimetry for mIBG therapy.* Q J Nucl Med Mol Imaging, 2011. **55**(2): p. 116-25.
26. Sjogreen-Gleisner, K., et al., *Dosimetry in patients with B-cell lymphoma treated with [(90)Y]ibritumomab tiuxetan or [(131)I]tositumomab.* Q J Nucl Med Mol Imaging, 2011. **55**(2): p. 126-54.
27. Cremonesi, M., et al., *Recent issues on dosimetry and radiobiology for peptide receptor radionuclide therapy.* Q J Nucl Med Mol Imaging, 2011. **55**(2): p. 155-67.
28. Chiesa, C., et al., *Need, feasibility and convenience of dosimetric treatment planning in liver selective internal radiation therapy with (90)Y microspheres: the experience of the National Tumor Institute of Milan.* Q J Nucl Med Mol Imaging, 2011. **55**(2): p. 168-97.
29. Hindorf, C., et al., *Clinical dosimetry in the treatment of bone tumors: old and new agents.* Q J Nucl Med Mol Imaging, 2011. **55**(2): p. 198-204.
30. Strigari, L., et al., *Dosimetry in nuclear medicine therapy: radiobiology application and results.* Q J Nucl Med Mol Imaging, 2011. **55**(2): p. 205-21.
31. Jentzen, W., et al., *Optimized 124I PET dosimetry protocol for radioiodine therapy of differentiated thyroid cancer.* J Nucl Med, 2008. **49**(6): p. 1017-23.
32. Hanscheid, H., et al., *Blood dosimetry from a single measurement of the whole body radioiodine retention in patients with differentiated thyroid carcinoma.* Endocr Relat Cancer, 2009. **16**(4): p. 1283-9.
33. Rault, E., et al., *Comparison of image quality of different iodine isotopes (I-123, I-124, and I-131).* Cancer Biother Radiopharm, 2007. **22**(3): p. 423-30.
34. *National Nuclear Data Center, Brookhaven National Laboratory*. Available from: http://www.nndc.bnl.gov/chart/decaysearchdirect.jsp?nuc=90Y&unc=nds. Note: to get data from another nuclide, e.g. ^{124}I, change "…nuc=90Y…" to "…nuc=124I…"
35. Pentlow, K.S., et al., *Quantitative imaging of iodine-124 with PET.* J Nucl Med, 1996. **37**(9): p. 1557-62.
36. Robinson, S., et al., *Performance of a block detector PET scanner in imaging non-pure positron emitters--modelling and experimental validation with 124I.* Phys Med Biol, 2004. **49**(24): p. 5505-28.
37. Vandenberghe, S., *Three-dimensional positron emission tomography imaging with 124I and 86Y.* Nucl Med Commun, 2006. **27**(3): p. 237-45.
38. Herzog, H., et al., *PET imaging problems with the non-standard positron emitters Yttrium-86 and Iodine-124.* Q J Nucl Med Mol Imaging, 2008. **52**(2): p. 159-65.
39. Jentzen, W., *Experimental investigation of factors affecting the absolute recovery coefficients in iodine-124 PET lesion imaging.* Phys Med Biol, 2010. **55**(8): p. 2365-98.
40. Freudenberg, R., M. Wendisch, and J. Kotzerke, *Geant4-Simulations for cellular dosimetry in nuclear medicine.* Z Med Phys, 2011. **21**(4): p. 281-9.
41. Lubberink, M. and H. Herzog, *Quantitative imaging of 124I and 86Y with PET.* Eur J Nucl Med Mol Imaging, 2011. **38 Suppl 1**: p. S10-8.
42. Walrand, S., et al., *Quantitation in PET using isotopes emitting prompt single gammas: application to yttrium-86.* Eur J Nucl Med Mol Imaging, 2003. **30**(3): p. 354-61.
43. Kull, T., et al., *Quantitative imaging of yttrium-86 PET with the ECAT EXACT HR+ in 2D mode.* Cancer Biother Radiopharm, 2004. **19**(4): p. 482-90.
44. Gates, V.L., et al., *Internal pair production of 90Y permits hepatic localization of microspheres using routine PET: proof of concept.* J Nucl Med, 2011. **52**(1): p. 72-6.
45. Walrand, S., et al., *Dosimetry of yttrium-labelled radiopharmaceuticals for internal therapy: 86Y or 90Y imaging?* Eur J Nucl Med Mol Imaging, 2011. **38 Suppl 1**: p. S57-68.
46. Selwyn, R.G., et al., *A new internal pair production branching ratio of 90Y: the development of a non-destructive assay for 90Y and 90Sr.* Appl Radiat Isot, 2007. **65**(3): p. 318-27.
47. Ott, R.J., *Imaging technologies for radionuclide dosimetry.* Phys Med Biol, 1996. **41**(10): p. 1885-94.
48. Lodge, M.A., et al., *Developing ^{124}I PET for applications in diagnostic and pharmacokinetic drug studies.* J Nucl Med, 2005. **46**(suppl 2): p. 113.
49. Kemerink, G.J., et al., *Effect of the positron range of 18F, 68Ga and 124I on PET/CT in lung-equivalent materials.* Eur J Nucl Med Mol Imaging, 2011. **38**(5): p. 940-8.

50. Gregory, R.A., et al., *Optimization and assessment of quantitative 124I imaging on a Philips Gemini dual GS PET/CT system.* Eur J Nucl Med Mol Imaging, 2009. **36**(7): p. 1037-48.
51. Prideaux, A.R., et al., *Three-dimensional radiobiologic dosimetry: application of radiobiologic modeling to patient-specific 3-dimensional imaging-based internal dosimetry.* J Nucl Med, 2007. **48**(6): p. 1008-16.
52. Grudzinski, J.J., et al., *Patient specific treatment planning for systemically administered radiopharmaceuticals using PET/CT and Monte Carlo simulation.* Appl Radiat Isot, 2010. **68**(1): p. 59-65.
53. Assié, K., et al., *A preliminary study of quantitative protocols in Indium 111 SPECT using computational simulations and phantoms.* IEEE Trans Nucl Sci, 2010. **57**: p. 1096-1104.
54. Ljungberg, M., et al., *3D absorbed dose calculations based on SPECT: evaluation for 111-In/90-Y therapy using Monte Carlo simulations.* Cancer Biother Radiopharm, 2003. **18**(1): p. 99-107.
55. Green, A.J., et al., *Accurate quantification of 131I distribution by gamma camera imaging.* Eur J Nucl Med, 1990. **16**(4-6): p. 361-5.
56. He, B. and E.C. Frey, *Comparison of conventional, model-based quantitative planar, and quantitative SPECT image processing methods for organ activity estimation using In-111 agents.* Phys Med Biol, 2006. **51**(16): p. 3967-81.
57. He, B., et al., *A Monte Carlo and physical phantom evaluation of quantitative In-111 SPECT.* Phys Med Biol, 2005. **50**(17): p. 4169-85.
58. He, B., et al., *Evaluation of quantitative imaging methods for organ activity and residence time estimation using a population of phantoms having realistic variations in anatomy and uptake.* Med Phys, 2009. **36**(2): p. 612-9.
59. Ljungberg, M., et al., *A 3-dimensional absorbed dose calculation method based on quantitative SPECT for radionuclide therapy: evaluation for (131)I using monte carlo simulation.* J Nucl Med, 2002. **43**(8): p. 1101-9.
60. Koral, K.F., A. Yendiki, and Y.K. Dewaraja, *Recovery of total I-131 activity within focal volumes using SPECT and 3D OSEM.* Phys Med Biol, 2007. **52**(3): p. 777-90.
61. Pereira, J.M., et al., *Image quantification for radiation dose calculations--limitations and uncertainties.* Health Phys, 2010. **99**(5): p. 688-701.
62. He, B., et al., *Comparison of residence time estimation methods for radioimmunotherapy dosimetry and treatment planning--Monte Carlo simulation studies.* IEEE Trans Med Imaging, 2008. **27**(4): p. 521-30.
63. He, B. and E.C. Frey, *Effects of shortened acquisition time on accuracy and precision of quantitative estimates of organ activity.* Med Phys, 2010. **37**(4): p. 1807-15.
64. He, B., et al., *Comparison of organ residence time estimation methods for radioimmunotherapy dosimetry and treatment planning--patient studies.* Med Phys, 2009. **36**(5): p. 1595-601.
65. He, B. and E.C. Frey, *The impact of 3D volume of interest definition on accuracy and precision of activity estimation in quantitative SPECT and planar processing methods.* Phys Med Biol, 2010. **55**(12): p. 3535-44.
66. Hobbs, R.F., et al., *A gamma camera count rate saturation correction method for whole-body planar imaging.* Phys Med Biol, 2010. **55**(3): p. 817-31.
67. Assie, K., et al., *Comparison between 2D and 3D dosimetry protocols in 90Y-ibritumomab tiuxetan radioimmunotherapy of patients with non-Hodgkin's lymphoma.* Cancer Biother Radiopharm, 2008. **23**(1): p. 53-64.
68. Garkavij, M., et al., *177Lu-[DOTA0,Tyr3] octreotate therapy in patients with disseminated neuroendocrine tumors: Analysis of dosimetry with impact on future therapeutic strategy.* Cancer, 2010. **116**(4 Suppl): p. 1084-92.
69. Sandstrom, M., et al., *Individualized dosimetry in patients undergoing therapy with (177)Lu-DOTA-D-Phe (1)-Tyr (3)-octreotate.* Eur J Nucl Med Mol Imaging, 2010. **37**(2): p. 212-25.
70. Norrgren, K., et al., *Accuracy of the quantification of organ activity from planar gamma camera images.* Cancer Biother Radiopharm, 2003. **18**(1): p. 125-31.
71. Jonsson, L., M. Ljungberg, and S.E. Strand, *Evaluation of accuracy in activity calculations for the conjugate view method from Monte Carlo simulated scintillation camera images using experimental data in an anthropomorphic phantom.* J Nucl Med, 2005. **46**(10): p. 1679-86.

72. Hammond, N.D., et al., *External imaging techniques for quantitation of distribution of I-131 F(ab')2 fragments of monoclonal antibody in humans.* Med Phys, 1984. **11**(6): p. 778-83.
73. Eary, J.F., et al., *Preliminary validation of the opposing view method for quantitative gamma camera imaging.* Med Phys, 1989. **16**(3): p. 382-7.
74. Sjogreen, K., M. Ljungberg, and S.E. Strand, *An activity quantification method based on registration of CT and whole-body scintillation camera images, with application to 131I.* J Nucl Med, 2002. **43**(7): p. 972-82.
75. Song, N., B. He, and E.C. Frey, *The effect of volume-of-interest misregistration on quantitative planar activity and dose estimation.* Phys Med Biol, 2010. **55**(18): p. 5483-97.
76. Flux, G.D., et al., *Estimation and implications of random errors in whole-body dosimetry for targeted radionuclide therapy.* Phys Med Biol, 2002. **47**(17): p. 3211-23.
77. Siegel, J.A., M.G. Stabin, and A.B. Brill, *The importance of patient-specific radiation dose calculations for the administration of radionuclides in therapy.* Cell Mol Biol (Noisy-le-grand), 2002. **48**(5): p. 451-9.
78. Stabin, M.G., *MIRDOSE: personal computer software for internal dose assessment in nuclear medicine.* J Nucl Med, 1996. **37**(3): p. 538-46.
79. Stabin, M.G., R.B. Sparks, and E. Crowe, *OLINDA/EXM: the second-generation personal computer software for internal dose assessment in nuclear medicine.* J Nucl Med, 2005. **46**(6): p. 1023-7.
80. Marine, P.M., et al., *Changes in radiation dose with variations in human anatomy: larger and smaller normal-stature adults.* J Nucl Med, 2010. **51**(5): p. 806-11.
81. Divoli, A., et al., *Effect of patient morphology on dosimetric calculations for internal irradiation as assessed by comparisons of Monte Carlo versus conventional methodologies.* J Nucl Med, 2009. **50**(2): p. 316-23.
82. Clark, L.D., et al., *Changes in radiation dose with variations in human anatomy: moderately and severely obese adults.* J Nucl Med, 2010. **51**(6): p. 929-32.
83. Furhang, E.E., G. Sgouros, and C.S. Chui, *Radionuclide photon dose kernels for internal emitter dosimetry.* Med Phys, 1996. **23**(5): p. 759-64.
84. Berker, Y., et al., *Activity quantification combining conjugate-view planar scintigraphies and SPECT/CT data for patient-specific 3-D dosimetry in radionuclide therapy.* Eur J Nucl Med Mol Imaging, 2011. **38**(12): p. 2173-85.
85. Loudos, G., et al., *A radionuclide dosimetry toolkit based on material-specific Monte Carlo dose kernels.* Nucl Med Commun, 2009. **30**(7): p. 504-12.
86. Guy, M.J., et al., *RMDP: a dedicated package for 131I SPECT quantification, registration and patient-specific dosimetry.* Cancer Biother Radiopharm, 2003. **18**(1): p. 61-9.
87. Clairand, I., et al., *DOSE3D: EGS4 Monte Carlo code-based software for internal radionuclide dosimetry.* J Nucl Med, 1999. **40**(9): p. 1517-23.
88. Coulot, J., M. Ricard, and B. Aubert, *Validation of the EGS usercode DOSE3D for internal beta dose calculation at the cellular and tissue levels.* Phys Med Biol, 2003. **48**(16): p. 2591-602.
89. Aubineau-Laniece, I., et al., *Current developments at IRSN on computational tools dedicated to assessing doses for both internal and external exposure.* Radiat Prot Dosimetry, 2005. **115**(1-4): p. 522-9.
90. Chiavassa, S., et al., *Validation of a personalized dosimetric evaluation tool (Oedipe) for targeted radiotherapy based on the Monte Carlo MCNPX code.* Phys Med Biol, 2006. **51**(3): p. 601-16.
91. Wemple, C.A., et al., *MINERVA: a multi-modality plugin-based radiation therapy treatment planning system.* Radiat Prot Dosimetry, 2005. **116**(1-4 Pt 2): p. 202-7.
92. Lehmann, J., et al., *Monte Carlo treatment planning for molecular targeted radiotherapy within the MINERVA system.* Phys Med Biol, 2005. **50**(5): p. 947-58.
93. Meredith, R., B. Wessels, and S. Knox, *Risks to normal tissues from radionuclide therapy.* Semin Nucl Med, 2008. **38**(5): p. 347-57.
94. Stabin, M.G., et al., *Evolution and status of bone and marrow dose models.* Cancer Biother Radiopharm, 2002. **17**(4): p. 427-33.
95. Hindorf, C., et al., *EANM Dosimetry Committee guidelines for bone marrow and whole-body dosimetry.* Eur J Nucl Med Mol Imaging, 2010. **37**(6): p. 1238-50.

96. Wahl, R.L., S. Kroll, and K.R. Zasadny, *Patient-specific whole-body dosimetry: principles and a simplified method for clinical implementation.* J Nucl Med, 1998. **39**(8 Suppl): p. 14S-20S.
97. Wahl, R.L., *The clinical importance of dosimetry in radioimmunotherapy with tositumomab and iodine I 131 tositumomab.* Semin Oncol, 2003. **30**(2 Suppl 4): p. 31-8.
98. Siegel, J.A., et al., *Sacral scintigraphy for bone marrow dosimetry in radioimmunotherapy.* Int J Rad Appl Instrum B, 1989. **16**(6): p. 553-9.
99. Wessels, B.W., et al., *Bone marrow dosimetry using blood-based models for radiolabeled antibody therapy: a multiinstitutional comparison.* J Nucl Med, 2004. **45**(10): p. 1725-33.
100. Sgouros, G., *Bone marrow dosimetry for radioimmunotherapy: theoretical considerations.* J Nucl Med, 1993. **34**(4): p. 689-94.
101. Hindorf, C., et al., *Evaluation of methods for red marrow dosimetry based on patients undergoing radioimmunotherapy.* Acta Oncol, 2005. **44**(6): p. 579-88.
102. Ferrer, L., et al., *Three methods assessing red marrow dosimetry in lymphoma patients treated with radioimmunotherapy.* Cancer, 2010. **116**(4 Suppl): p. 1093-100.
103. Stabin, M.G., J.A. Siegel, and R.B. Sparks, *Sensitivity of model-based calculations of red marrow dosimetry to changes in patient-specific parameters.* Cancer Biother Radiopharm, 2002. **17**(5): p. 535-43.
104. Walrand, S., et al., *Experimental facts supporting a red marrow uptake due to radiometal transchelation in 90Y-DOTATOC therapy and relationship to the decrease of platelet counts.* Eur J Nucl Med Mol Imaging, 2011. **38**(7): p. 1270-80.
105. Lassmann, M., et al., *EANM Dosimetry Committee series on standard operational procedures for pretherapeutic dosimetry I: blood and bone marrow dosimetry in differentiated thyroid cancer therapy.* Eur J Nucl Med Mol Imaging, 2008. **35**(7): p. 1405-12.
106. Baechler, S., et al., *Extension of the biological effective dose to the MIRD schema and possible implications in radionuclide therapy dosimetry.* Med Phys, 2008. **35**(3): p. 1123-34.
107. Buckley, S.E., et al., *Whole-body dosimetry for individualized treatment planning of 131I-MIBG radionuclide therapy for neuroblastoma.* J Nucl Med, 2009. **50**(9): p. 1518-24.
108. Baechler, S., et al., *Predicting hematologic toxicity in patients undergoing radioimmunotherapy with 90Y-ibritumomab tiuxetan or 131I-tositumomab.* J Nucl Med, 2010. **51**(12): p. 1878-84.
109. Siegel, J.A., et al., *Red marrow radiation dose adjustment using plasma FLT3-L cytokine levels: improved correlations between hematologic toxicity and bone marrow dose for radioimmunotherapy patients.* J Nucl Med, 2003. **44**(1): p. 67-76.
110. Cremonesi, M., et al., *Dosimetry for treatment with radiolabelled somatostatin analogues. A review.* Q J Nucl Med Mol Imaging, 2010. **54**(1): p. 37-51.
111. Cremonesi, M., et al., *Dosimetry in Peptide radionuclide receptor therapy: a review.* J Nucl Med, 2006. **47**(9): p. 1467-75.
112. Rolleman, E.J., et al., *Kidney protection during peptide receptor radionuclide therapy with somatostatin analogues.* Eur J Nucl Med Mol Imaging, 2010. **37**(5): p. 1018-31.
113. Wessels, B.W., et al., *MIRD pamphlet No. 20: the effect of model assumptions on kidney dosimetry and response--implications for radionuclide therapy.* J Nucl Med, 2008. **49**(11): p. 1884-99.
114. Valkema, R., et al., *Long-term follow-up of renal function after peptide receptor radiation therapy with (90)Y-DOTA(0),Tyr(3)-octreotide and (177)Lu-DOTA(0), Tyr(3)-octreotate.* J Nucl Med, 2005. **46 Suppl 1**: p. 83S-91S.
115. Bouchet, L.G., et al., *MIRD Pamphlet No 19: absorbed fractions and radionuclide S values for six age-dependent multiregion models of the kidney.* J Nucl Med, 2003. **44**(7): p. 1113-47.
116. Walrand, S., et al., *4-Step renal dosimetry dependent on cortex geometry applied to 90Y peptide receptor radiotherapy: evaluation using a fillable kidney phantom imaged by 90Y PET.* J Nucl Med, 2010. **51**(12): p. 1969-73.
117. O'Donoghue, J., *Relevance of external beam dose-response relationships to kidney toxicity associated with radionuclide therapy.* Cancer Biother Radiopharm, 2004. **19**(3): p. 378-87.
118. Siegel, J.A., M.G. Stabin, and R.M. Sharkey, *Renal dosimetry: ready for biological effective dose?* Cancer Biother Radiopharm, 2010. **25**(5): p. 589-91.

119. Barone, R., et al., *Patient-specific dosimetry in predicting renal toxicity with (90)Y-DOTATOC: relevance of kidney volume and dose rate in finding a dose-effect relationship.* J Nucl Med, 2005. **46 Suppl 1**: p. 99S-106S.
120. O'Donoghue, J.A., M. Bardies, and T.E. Wheldon, *Relationships between tumor size and curability for uniformly targeted therapy with beta-emitting radionuclides.* J Nucl Med, 1995. **36**(10): p. 1902-9.
121. Stabin, M., *Nuclear medicine dosimetry.* Phys Med Biol, 2006. **51**(13): p. R187-202.
122. Cai, Z., et al., *Cellular dosimetry of (111)In using monte carlo N-particle computer code: comparison with analytic methods and correlation with in vitro cytotoxicity.* J Nucl Med, 2010. **51**(3): p. 462-70.
123. Sgouros, G., et al., *MIRD Pamphlet No. 22 (abridged): radiobiology and dosimetry of alpha-particle emitters for targeted radionuclide therapy.* J Nucl Med, 2010. **51**(2): p. 311-28.
124. Meredith, R.F. and D.J. Buchsbaum, *Pretargeted radioimmunotherapy.* Int J Radiat Oncol Biol Phys, 2006. **66**(2 Suppl): p. S57-9.
125. Kunikowska, J., et al., *Clinical results of radionuclide therapy of neuroendocrine tumours with 90Y-DOTATATE and tandem 90Y/177Lu-DOTATATE: which is a better therapy option?* Eur J Nucl Med Mol Imaging, 2011. **38**(10): p. 1788-97.
126. Hobbs, R.F., et al., *A treatment planning method for sequentially combining radiopharmaceutical therapy and external radiation therapy.* Int J Radiat Oncol Biol Phys, 2011. **80**(4): p. 1256-62.
127. Israel, I., et al., *Validation of an amino-acid-based radionuclide therapy plus external beam radiotherapy in heterotopic glioblastoma models.* Nucl Med Biol, 2011. **38**(4): p. 451-60.

Chapter 3

Dose-response relationship in differentiated thyroid cancer patients undergoing radioiodine treatment assessed by means of ^{124}I PET/CT

R. Wierts, B. Brans, B. Havekes, G.J. Kemerink, S. G. Halders, N.N. Schaper, W.H. Backes, F.M. Mottaghy, W. Jentzen

J Nucl Med. 2016 Jul;57(7): 1027-32. doi: 10.2967/jnumed.115.168799

Abstract

The dose-response relationship in a fixed-activity approach generally applied in the treatment of differentiated thyroid cancer was assessed using ^{124}I PET/CT.

Methods

Pre-therapeutic ^{124}I PET/CT images of 47 patients scheduled for radioiodine therapy were retrospectively analysed. ^{124}I PET/CT images were acquired 24 and 96 hours after oral administration of approximately 28 MBq ^{124}I-sodium iodide. Lesions were identified as thyroid remnants or metastases (lymph node, lung, bone). After a neoteric segmentation technique allowing accurate volume estimation down to the ^{124}I PET spatial resolution of 0.15 mL was applied, lesions were divided into a known-volume group and a small-volume group. For the known-volume group, average lesion absorbed dose (AD) values were calculated, whereas for the small-volume group a minimum lesion AD was estimated. Lesion response was determined on the basis of ^{124}I PET/CT and ^{131}I SPECT(/CT) follow-up images. A lesion not detectable on any of the follow-up images was considered a completely responding lesion. Differences in lesion AD estimations between completely and incompletely responding lesions were evaluated by Mann-Whitney *U* test. Moreover, receiver-operator-characteristic curves were used to test the performance of pre-therapeutic ^{124}I PET/CT lesion AD for prediction of complete lesion response.

Results

In the approach of fixed radioiodine activity (3.0 ± 1.0 GBq), 89% of thyroid remnants and 69% of metastases responded completely. Except for the small-volume groups, the lesion AD of completely responding lesions was significantly higher than that of incompletely responding lesions. Using receiver-operator-characteristic curve analysis, it was shown that for the known-volume group, pre-therapeutic ^{124}I PET/CT lesion dosimetry can be used as a prognostic tool to predict lesion-based ^{131}I therapy response with an area under the curve of 0.76 for remnants and 0.97 for metastases. The corresponding lesion AD threshold value maximizing correct complete response prediction was 90 Gy for remnants and 40 Gy for metastases.

Conclusion

In a fixed-activity approach, a statistically significant dose-response relationship for both thyroid remnants and metastases using pre-therapeutic ^{124}I PET/CT lesion dosimetry was found. The findings may be useful in patient management.

Introduction

Radioiodine therapy is the standard adjuvant therapy, after total thyroidectomy in patients with differentiated thyroid cancer (DTC) [1, 2]. The purpose of radioiodine therapy is 2-fold: ablation of thyroid remnants and treatment of radioiodine-avid metastases.

The generally accepted threshold for lesion absorbed dose (AD) to achieve high therapy response is 85 Gy for metastases and 300 Gy for thyroid remnants [3, 4]. To predict therapy response, a reliable AD estimation requires, inter alia, accurate lesion volume determination, which is hampered by the often small lesion volumes with respect to the spatial resolution of ^{131}I scintigraphy and lesion segmentation difficulties encountered in ultrasonography, CT, or other imaging modalities [1, 5]. As a result, personalized radioiodine therapy based on lesion dosimetry is not globally adopted. In general, a fixed ^{131}I activity is administered on the basis of disease characteristics and patient age, with the risk of under- or overtreatment [6].

Several groups have concluded that quantitation of ^{124}I PET images is feasible [7-11]. Compared with ^{131}I SPECT, ^{124}I PET imaging offers a higher image spatial resolution, increased counting rate sensitivity, and higher quantitative capacity, resulting in the application of pre-therapeutic ^{124}I PET/CT-based lesion dosimetry [12-17].

To date, the only study assessing the dose-response relationship using ^{124}I PET/CT in a larger number of patients was recently published by Jentzen et al. [17]. Pre-therapeutic ^{124}I PET/CT lesion AD estimation and toxicity assessment were taken into consideration in patient management, allowing the administration of an optimized therapeutic activity (8.0 ± 4.3 GBq). However, using a fixed-activity approach in the absence of toxicity assessment generally results in lower administered ^{131}I activity than the optimized therapeutic activity. Consequently, it is expected that the lesion ADs in the fixed-activity approach are lower than the values published by Jentzen et al. [17], possibly resulting in more lesions that receive a lesion AD below the established threshold values.

Therefore, the aim of this study was to assess the dose-response relationship in an approach of a fixed therapeutic ^{131}I activity in a large group of patients using pre-therapeutic ^{124}I PET/CT lesion dosimetry. Moreover, a new segmentation technique allowing volume estimation down to the PET spatial resolution of ^{124}I was used [18]. In addition, we assessed the feasibility of performing pre-therapeutic ^{124}I PET/CT lesion dosimetry as a prognostic tool to predict therapy response in DTC patients in a fixed-activity approach.

Materials and methods

Patient population

This study was approved by the institutional review board, and the requirement to obtain informed consent was waived. In the Maastricht University Medical Centre, pre-therapeutic imaging with ^{124}I was introduced as a clinical standard in 2007. A retrospective analysis of DTC patients who underwent ^{124}I PET/CT examinations, followed by ^{131}I therapy, between January 2007 and December 2012 was performed. All patients had histologically confirmed papillary or follicular DTC and underwent total thyroidectomy prior to ^{124}I PET/CT examinations. None of the patients received additional treatment such as surgery or external-beam radiation therapy. Patients were included if (post-therapy) follow-up imaging with either (pre-therapeutic) ^{124}I PET/CT or ^{131}I planar whole body scintigraphy and ^{131}I SPECT/CT as part the radioiodine therapy was available. For patients who underwent multiple radioiodine therapies preceded by ^{124}I PET/CT examinations, only the data of the first radioiodine therapy were included. Patient TNM status was characterized in 4 stages according to the American Joint Committee on Cancer Staging Atlas [19]. Moreover, the maximum thyroglobulin value recorded within 1 y after ^{131}I ablation therapy was reported. Until March 2011, thyroglobulin was measured using a time-resolved fluoroimmunoassay (Autodelfia; PerkinElmer) with a limit of detection of 0.5 pmol/L. From March 2011, thyroglobulin was measured using a time-resolved amplified cryptate emission assay (Brahms GmbH; Thermo Fisher) with a limit of detection of 0.25 pmol/L. Abnormal (positive) results were recorded if thyroglobulin was greater than 1.5 pmol/L. In the case of incomplete recovery of the antibody used in the assay, additional testing was done for specific antithyroglobulin antibodies.

Patient preparation was done by thyroid hormone withdrawal or recombinant human thyroid-stimulating hormone (rhTSH) and was similar for the pre- and follow-up ^{124}I PET/CT examinations. In the case of thyroid hormone withdrawal, patients were withdrawn from thyroxine medication for 4-6 weeks, or remained without medication post-operatively. In the cases of rhTSH preparation, 0.9 mg of thyrotropin alfa or rhTSH (Thyrogen; Genzyme Ltd.) was injected intramuscularly on days 1 and 2, afterward ^{124}I was orally administered on day 4, and ^{124}I PET/CT was performed on day 5 (24 h after ^{124}I administration) and day 8 (96 h after ^{124}I administration). For radioiodine therapy, a fixed-activity protocol was performed according to the Dutch guidelines, using 2.8 GBq (75 mCi) for simple thyroid remnant ablation and 5.6 GBq (150 mCi) for regional nodal disease or distant metastases.

Image acquisition and reconstruction

^{124}I PET/CT was performed in 3-dimensional mode using a PET camera equipped with time-of-flight (Gemini TF PET/64-slice CT scanner; Philips) at 24 and 96 h after oral ad-

ministration of 28.0 ± 3.3 MBq of ^{124}I-sodium iodide. ^{124}I radioactivity was measured using a 3-mL syringe filled with approximately 1 mL of ^{124}I solution that was placed in a validated dose calibrator (Isomed 2000; Nuklear Medizin Technik GmbH). ^{124}I PET scans were acquired from the head, neck and thorax comprising 4-5 bed positions of 4 min each. In selected cases, imaging was continued until the pelvis. A low-dose spiral CT scan from the head to thigh was acquired (tube voltage, 120 kVp; effective tube current, 30 mAs; slice thickness, 4 mm), followed by the PET acquisition and supplemental high-dose CT without contrast (neck, 120 kV; 150 mAs, slice thickness, 2 mm; increment, 1.8; and thorax, 120 kV; 175 mAs; slice thickness, 5 mm; increment, 4.0). All CT images were reconstructed using the filtered backprojection algorithm. PET images were reconstructed using the line of response-based, time-of-flight reconstruction algorithm provided by the manufacturer with a voxel size of 4 × 4 × 4 mm^3. In addition, for accurate lesion volume assessment and quantification purposes, PET images were retrospectively reconstructed with a voxel size of 2 × 2 × 2 mm^3. For all PET images, standard corrections for attenuation, scatter, decay, and dead-time were performed.

The ^{131}I whole-body scintigraphy was made as a total-body scan from top until toe using a table speed of 10 cm/min. SPECT/CT was acquired immediately after whole-body scintigraphy. ^{131}I SPECT/CT was acquired using a standard SPECT/CT camera, (Precedence SPECT/6-slice CT scanner; Philips) equipped with dual 1.6 cm γ-detectors with high-energy general-purpose collimators. SPECT data were obtained by a noncircular orbit, a 128 × 128 matrix (voxel size, 4.7 × 4.7 × 4.7 mm^3) and 32 angles over 180° and 45 s per stop, using a 364-keV photo peak with 10% window (total acquisition time, 24 min). Reconstruction space and width was 3 mm using the Philips Astonish algorithm.

Lesion volume calculation

The volume of each lesion with focal uptake, present on both of the pre-therapeutic ^{124}I PET images (24 and 96 h after administration) was semi-automatically determined using an in-house-built software algorithm (Matlab; The Mathworks) based on a recently published iterative thresholding method [18]. The method assumes a spherically shaped lesion with homogeneous ^{124}I uptake. Accounting for the reconstructed ^{124}I PET spatial resolution of 6.7 mm (expressed as full-width at half maximum), background-corrected relative boundary-reproducing values used for lesion delineation were calculated. The smallest diameter or volume that can be determined using this method corresponds to the PET spatial resolution or its equivalent sphere volume of 0.15 mL. Consequently, lesions were classified into 2 groups in line with a previous study [17]: lesions with reliable volume estimation larger than 0.15 mL, the so-called known-volume group, and lesions with a volume smaller than 0.15 mL, the small-volume group. For the known-volume group, the lesion volume was calculated as the average value of the lesion vol-

ume determined on the 24 and 96 h ^{124}I PET images. Lesions for which the average lesion volume differed more than 30% with respect to the 24 or 96 h volume were excluded. Lesions for which either the 24 or 96 h volume was smaller than 0.15 mL were classified into the small-volume group. For the small-volume group, the lesion volume used for lesion AD estimation was assumed to be equal to the PET spatial resolution volume of 0.15 mL.

Lesion-absorbed dose estimation

For each ^{124}I PET image, lesion uptake was calculated as the average activity concentration of the segmented volume, corrected for partial volume effect, using measured (absolute) recovery coefficients [18], which effectively corrects for prompt γ-coincidence effect as well [20]. Assuming identical ^{124}I and ^{131}I pharmacokinetics, half-life correction was performed on the ^{124}I activity concentration to assess the projected ^{131}I activity concentration. ^{131}I residence time was determined according to the adapted 2-points approach [21]. In the case the effective half-life was less than the physical ^{131}I half-life, the lesion time-activity curve was parameterized using a combination of a linear uptake function and a mono-exponential decay function (interception time at 8 h after ^{131}I administration). In the case the effective half-life was greater than the ^{131}I physical half-life, physical decay was assumed beyond the 96 h time point. The (self-irradiation) lesion AD was calculated using the sphere model in the Olinda software package (Olinda version 1.1; Vanderbilt University) [22]. For all lesions, a density of 1.0 g/mL was used, resulting in an average and a minimum lesion AD per administered ^{131}I activity for the known-volume and small-volume groups, respectively. The predicted average and minimum lesion AD delivered in radioiodine therapy were estimated by multiplication with the therapeutic ^{131}I activity.

Therapy response assessment

Lesion-based analysis

Lesions were classified as either thyroid remnants or metastases including lymph node or distant metastases (lymph node, lung, bone). Both the thyroid remnants and the metastases were subdivided into a known-volume group and a small-volume group. Each individual lesion was either defined as completely or incompletely responding by an experienced nuclear medicine physician and medical physicist. Specifically, the completely responding lesion did not show ^{124}I uptake on subsequent follow-up scanning within 1 y and no ^{131}I uptake on subsequent post-therapeutic planar and SPECT/CT scanning. In contrast, the incompletely responding lesion did show focal ^{124}I or ^{131}I uptake on the day-4 scan (in the absence of significant level of background noise), not contributable to physiologic uptake according to visual assessment. For each lesion group, the predicted lesion AD in radioiodine therapy of the completely responding

lesions was compared with that of the incompletely responding lesions. Moreover, the performance of pre-therapeutic ^{124}I PET/CT to predict complete lesion response was assessed using receiver-operating-characteristic (ROC) curve analysis [23].

Patient-based analysis

Patients were classified as incompletely responding if persisting disease after radioiodine therapy was demonstrated, either by functional imaging (^{124}I PET/CT, ^{131}I SPECT/CT, ^{18}F-FDG), anatomic imaging (ultrasonography, MRI), histology or increased thyroglobulin value. Otherwise patients were classified as completely responding. The average patient-based lesion AD was calculated as the mean lesion AD of all radioiodine-avid lesions observed per patient.

Statistics

Statistical analysis was performed using SPSS version 22 (IBM Corp.). Descriptive data are shown as mean ± SD (median; range). Differences between 2 groups were assessed using the Mann-Whitney *U* test. Values for *P* less than 0.05 were considered statistically significant. ROC curves were used to test the performance of pre-therapeutic ^{124}I PET/CT lesion AD for the prediction of complete lesion response.

Results

Patient and lesion characteristics

Detailed patient characteristics are provided in Table 3.1. Of the in total 67 patients satisfying the inclusion criteria, 1 patient was excluded because this patient received a diagnostic CT with iodine- containing contrast agent before the ^{124}I PET/CT scan. Three patients were excluded because of the lack of either the 24 or 96 h ^{124}I PET/CT examination. Furthermore, 12 patients were excluded because of the unavailability of the PET raw data required for the additional retrospective 2 × 2 × 2 mm^3 voxel image reconstruction. Four patients did not show any visible lesions on the ^{124}I PET images. Of the remaining 47 patients, 29 patients were classified as completely responding and 18 patients as incompletely responding.

Detailed lesion characteristics are given in Table 3.2. In total, 168 lesions were suitable for AD estimation. Nine lesions were excluded because of lesion volume discrepancies in the 24 and 96 h scans. For the thyroid remnants and metastases, 89% (109/123) and 69% (31/45) of the lesions showed a complete response, respectively.

Lesion-based therapy response

Figure 3.1 illustrates the calculated lesion AD in radioiodine therapy for both thyroid remnants and metastases for all lesions (including known- and small-volume group), the known-volume group and the small-volume group. A statistically significant higher lesion AD was observed for the completely responding lesions than the incompletely responding lesions for all lesions and the known-volume group, but not for the small-volume remnants group. Because there were only 2 incompletely responding lesions in the small-volume metastases group, no statistical tests were performed for this group. Detailed lesion data are provided in the supplemental materials (available at http://jnm.snmjournals.org).

TABLE 3.1. Characteristics of analysed (N=47) patients. Descriptive data are shown as mean ± SD, with median and range in parentheses.

Characteristic	Completely responding	Incompletely responding
Age (y)	51 ± 11 (52; 23–70)	50 ± 18 (53; 18–79)
Sex		
Male	4	7
Female	25	11
Number of lesions		
Thyroid remnants	74	49
Metastases	6	39
Variant		
Papillary	21	11
Follicular	8	7
TNM stage		
1	13	8
2	4	-
3	12	4
4	-	6
Maximum thyroglobulin value in FU (pmol/L)	11 ± 55 (<0.5; 0.25–290)	$2.5 \cdot 10^3 \pm 7.0 \cdot 10^3$ (5.7; <0.2 –2.510^4)
First ^{131}I radionuclide therapy		
Yes	26	16
No	3	2
Single therapeutic ^{131}I activity (GBq)	3.0 ± 0.7 (2.8; 2.8–5.5)	3.0 ± 1.0 (2.8; 1.1–5.5)
Follow-up period (mo)	19 ± 16 (10; 4.5–61)	17 ± 17 (9; 3.5–64)

TABLE 3.2. Overview of analysed lesions.

Characteristic	Completely responding	Incompletely responding
Thyroid remnants	109	14
Known-volume group	39	8
Paratracheal	12	5
Thyroid bed	7	-
Cervical high	20	3
Small-volume group	70	6
Paratracheal	45	1
Thyroid bed	11	1
Cervical high	14	4
Metastases	31	14
Known-volume group	6	12
Thyroid bed	-	-
Neck lateral (II-V)	5	1
Cervical high	-	-
Cervical low (VI)	1	-
Distant	-	11
Small-volume group	25	2
Thyroid bed	2	1
Neck lateral (II-V)	18	-
Cervical high	4	-
Cervical low	1	-
Distant	-	1

Figure 3.2 shows the ROC curves for both the thyroid remnants and the metastases. Except for the metastatic small-volume group, all area under the curve values were significantly higher than 0.5. The area under the curve values were highest for the known-volume group. The arrow in Figure 3.2 corresponds to the established threshold values for the lesion AD of 300 Gy for thyroid remnants and 85 Gy for metastases [3, 4]. For the known-volume group, these threshold values resulted in sensitivity values of 0.69 and 0.67 and specificity values of 0.75 and 0.92 for the thyroid remnants and metastases, respectively. The Youden index [24], defined as the value that gives the maximum correct classification, was calculated as being 90 Gy for thyroid remnants and 40 Gy for metastases, resulting in respective sensitivity values of 0.85 and 1.0, and specificity values of 0.75 and 0.92.

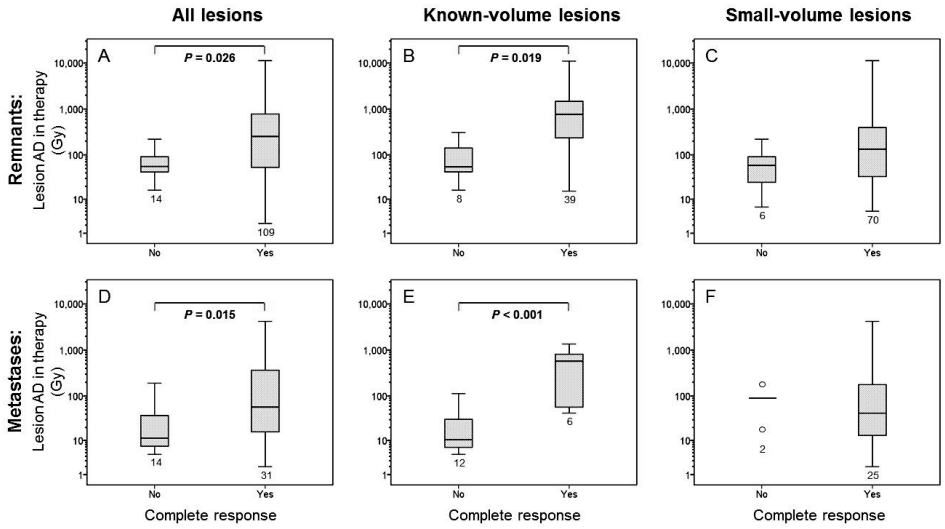

FIGURE 3.1. Box plots of lesion AD for both remnants (A-C) and metastases (D-F). Box plots are provided for all lesions (A and D), the known-volume group (B and E) and the small-volume group (C and F). Statistically significant differences are characterized by $P < 0.05$. Numbers close to whiskers represent the number of lesions.

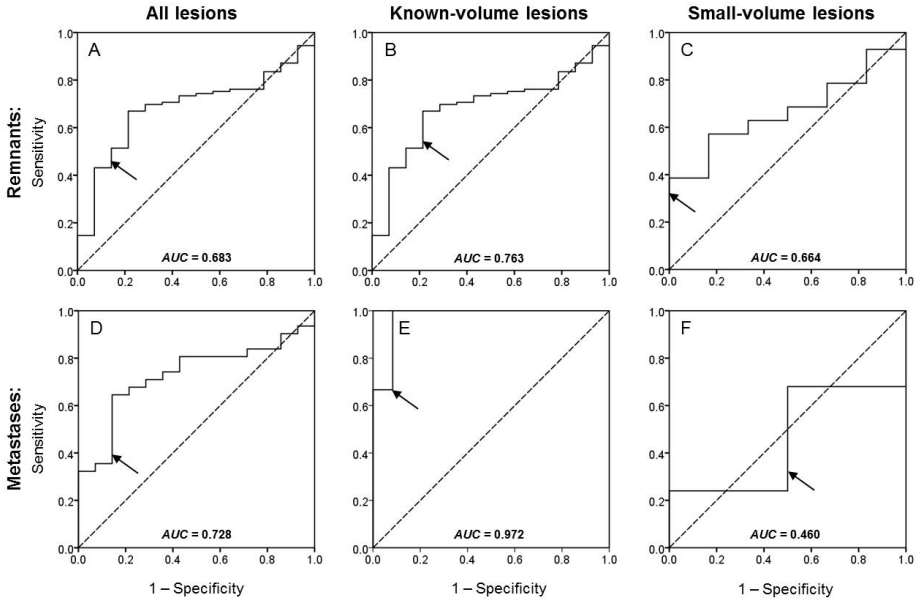

FIGURE 3.2. ROC curves for both remnants (A,B,C) and metastases (D,E,F). ROC curves are provided for all lesions (A,D), the known-volume group (B,E) and small-volume group (C,F). The arrows correspond to a threshold value of 300 Gy for remnants and 85 Gy for metastases. The dashed line represents the line of equality.

Patient-based therapy response

In Table 3.1, it can be derived that the incompletely responding patients had a higher TNM status and considerably more radioiodine-avid metastases than the completely responding patients. The median patient-based thyroid remnant lesion AD was higher for the completely responding patients (370 Gy) than the incompletely responding patients (180 Gy) but this was not statistically significant. For metastases, the median patient-based lesion AD was higher for the incompletely responding patients (63 Gy) compared to the completely responding patients (39 Gy) but also not statistically significant. In 7 patients a complete response of all radioiodine-avid lesions was seen at the lesion-based analysis. However, in the patient-based analysis these did not have a complete response because during follow-up new lesions in other anatomic areas were detected with ^{18}F-FDG PET/CT, ^{124}I PET/CT or ultrasound in combination with cytology.

Discussion

Maxon et al. [3, 4] demonstrated that a lesion AD threshold of 300 Gy for thyroid remnants and 85 Gy for lymph node metastases was associated with a high complete lesion response rate of 80–90%, establishing the lesion AD as an important quantity for prediction of lesion response in radioiodine treatment. Several groups have identified ^{124}I PET/CT as a promising modality for performing lesion-based dosimetry [12-17]. Applying an empirically fixed radioiodine activity approach, Flower et al. [12] were the first to assess lesion AD in 3 patients using ^{124}I PET. In agreement with our findings, they reported that the administration of fixed activities (3.0–5.5 GBq) resulted in a large variation of lesion AD to both thyroid remnants (16–400 Gy) and involved neck nodes (2.5–33 Gy). In contrast, Erdi et al. [13] developed a method to estimate lesion AD of thyroid remnants based on pre-therapeutic ^{124}I PET imaging at maximum-tolerated activity of ^{131}I using a dose constraint of 2 Gy to blood. Performing this method in 3 patients, they observed a large lesion AD range (5–248 Gy) at maximum-tolerated activity (10–15.5 GBq). Indeed, an approach of maximum-tolerated activity applying a maximum blood dose of 2 Gy has been reported to be safe and well-tolerated [25-27]. Alternatively, several groups have reported on an optimal activity approach using pre-therapeutic ^{124}I PET/CT lesion AD calculations [14-16]. In this approach, ^{131}I therapeutic activity was chosen to achieve lesion AD values above the established threshold values, considering toxicity estimations. Although this approach has been reported to result in change in patient management in 25–50% of DTC patients [14, 16], the biologic effectiveness of dosimetry-guided approaches is not proven yet [1].

To date, the only study assessing the dose-response relationship by means of ^{124}PET/CT in a larger number of patients was recently published by Jentzen et al. [17]. Therapy response for thyroid remnant and metastatic lesions above the accepted lesion

AD was assessed using an optimum activity approach. This approach resulted in relatively high therapeutic ^{131}I activity (median, 10 GBq; range, 2–20 GBq) and most lesions, as expected, received an AD above the established threshold values. In our study, therapeutic activity was almost 4 times lower (median, 2.8 GBq; range, 1.1 – 5.5 GBq), and the estimated lesion AD range extended to the lower lesion AD values. As a result, we observed a statistically significant dose-response relationship, confirming a higher calculated lesion AD of completely responding lesions than the incompletely responding lesions. Interestingly, for thyroid remnants we observed a complete lesion response of 89% which is in good agreement with a complete response of 91% found by Jentzen et al. [17], whereas for metastases our study showed a complete lesion response of 69% compared with 88%. These findings suggest that an optimized activity approach might be most beneficial in DTC patients presenting with metastatic disease.

Using ROC curve analysis, we showed that for lesions larger than 0.15 mL, pre-therapeutic ^{124}I PET/CT lesion dosimetry can be used as a prognostic tool to predict lesion-based ^{131}I therapy response. For these lesions, the optimal threshold value was 90 Gy for thyroid remnants and 40 Gy for metastases. These values are considerably lower than the accepted threshold values of 300 Gy and 85 Gy. However, it is important to note that these optimum lesion AD thresholds are defined as the values that give the maximum correct classification combining both sensitivity and specificity. In DTC patient management, a correct prediction of incompletely responding lesions is important. Consequently, for patient's management decision making, higher AD threshold values may be preferred.

Reliable lesion dosimetry requires accurate radioactivity quantification and volume estimation, which are affected by the finite spatial resolution of current nuclear medicine imaging equipment [28], in particular for the small lesion volumes often encountered in DTC patients. In addition, high-spatial-resolution images obtained by ultrasonography or CT are considered unreliable because of a lack of differentiation between thyroid tissue and hematoma on these modalities [1]. As a result, lesion AD calculations are considered unreliable for small lesions. Using an established PET-based thresholding method yielding reliable volume estimation for lesions larger than 0.80 mL, Jentzen et al. [17] were able to accurately calculate lesion AD for 24% and 27% of all analysed thyroid remnants and metastases, respectively. In our study, we used a more advanced segmentation technique allowing volume estimation down to the ^{124}I PET spatial resolution volume of 0.15 mL. Consequently, reliable lesion AD estimation was obtained in 38% of thyroid remnants and 40% of metastases. Despite the improved volume segmentation technique, for most lesions only the minimum lesion AD could be calculated. In the future, further developments in PET/MRI might contribute to additional improvements of the dosimetry in small-volume disease [29].

Using voxel-based 3-dimensional dose distribution calculations, several studies have reported on the AD distribution heterogeneity within lesions [13, 14]. In these studies, substantial variability in intra-tumour AD was observed, possibly resulting in underdos-

ing of tumour subregions and ultimately therapy failure [13]. Although in our study correction for partial-volume effect was performed by means of the recovery coefficient, heterogeneity of the lesion AD distribution was not considered because most lesions included in our study were small compared with the ^{124}I PET spatial resolution.

A limitation of our study was its retrospective nature. However, a high concordance with other studies using ^{124}I likely confirms the validity of our results. In fact, to date, no prospective randomized study addressing the optimal activity approach has been published, and the optimal therapeutic activity is not established yet [1, 2]. The results of our study indicate that pre-therapeutic ^{124}I PET/CT lesion dosimetry can be used as a prognostic tool to predict lesion response. Therefore, we would strongly advocate cooperative efforts to establish a multicenter prospective ^{124}I trial to confirm our findings.

Conclusion

This study provides evidence of a statistically significant dose-response relationship assessed by means of pre-therapeutic ^{124}I PET/CT dosimetry in both thyroid remnants and metastases. This will be a clinically useful contribution in patient management.

Disclosure

The costs of publication of this article were defrayed in part by the payment of page charges. Therefore, and solely to indicate this fact, this article is hereby marked “advertisement” in accordance with 18 USC section 1734. No potential conflict of interest relevant to this article was reported.

References

1. Luster, M., et al., *Guidelines for radioiodine therapy of differentiated thyroid cancer.* Eur J Nucl Med Mol Imaging, 2008. **35**(10): p. 1941-59.
2. American Thyroid Association (ATA) Guidelines Taskforce on Thyroid Nodules and Differentiated Thyroid Cancer, Cooper, D.S., et al., *Revised American Thyroid Association management guidelines for patients with thyroid nodules and differentiated thyroid cancer*. Thyroid, 2009. **19**(11): p. 1167-214..
3. Maxon, H.R., et al., *Relation between effective radiation dose and outcome of radioiodine therapy for thyroid cancer.* N Engl J Med, 1983. **309**(16): p. 937-41.
4. Maxon, H.R., 3rd, et al., *Radioiodine-131 therapy for well-differentiated thyroid cancer--a quantitative radiation dosimetric approach: outcome and validation in 85 patients.* J Nucl Med, 1992. **33**(6): p. 1132-6.
5. Eschmann, S.M., et al., *Evaluation of dosimetry of radioiodine therapy in benign and malignant thyroid disorders by means of iodine-124 and PET.* Eur J Nucl Med Mol Imaging, 2002. **29**(6): p. 760-7.
6. Lassmann, M., et al., *The use of dosimetry in the treatment of differentiated thyroid cancer.* Q J Nucl Med Mol Imaging, 2011. **55**(2): p. 107-15.
7. Pentlow, K.S., et al., *Quantitative imaging of iodine-124 with PET.* J Nucl Med, 1996. **37**(9): p. 1557-62.
8. Herzog, H., et al., *PET quantitation and imaging of the non-pure positron-emitting iodine isotope 124I.* Appl Radiat Isot, 2002. **56**(5): p. 673-9.
9. Lubberink, M. and H. Herzog, *Quantitative imaging of 124I and 86Y with PET.* Eur J Nucl Med Mol Imaging, 2011. **38 Suppl 1**: p. S10-8.
10. Jentzen, W., *Experimental investigation of factors affecting the absolute recovery coefficients in iodine-124 PET lesion imaging.* Phys Med Biol, 2010. **55**(8): p. 2365-98.
11. Preylowski, V., et al., *Is the image quality of I-124-PET impaired by an automatic correction of prompt gammas?* PLoS One, 2013. **8**(8): p. e71729.
12. Flower, M.A., et al., *Radiation dose assessment in radioiodine therapy. 2. Practical implementation using quantitative scanning and PET, with initial results on thyroid carcinoma.* Radiother Oncol, 1989. **15**(4): p. 345-57.
13. Erdi, Y.E., et al., *Radiation Dose Assessment for I-131 Therapy of Thyroid Cancer Using I-124 PET Imaging.* Clin Positron Imaging, 1999. **2**(1): p. 41-46.
14. Sgouros, G., et al., *Patient-specific dosimetry for 131I thyroid cancer therapy using 124I PET and 3-dimensional-internal dosimetry (3D-ID) software.* J Nucl Med, 2004. **45**(8): p. 1366-72.
15. Freudenberg, L.S., et al., *124I-PET dosimetry in advanced differentiated thyroid cancer: therapeutic impact.* Nuklearmedizin, 2007. **46**(4): p. 121-8.
16. Pettinato, C., et al., *Pretherapeutic dosimetry in patients affected by metastatic thyroid cancer using 124I PET/CT sequential scans for 131I treatment planning.* Clin Nucl Med, 2014. **39**(8): p. e367-74.
17. Jentzen, W., et al., *Assessment of lesion response in the initial radioiodine treatment of differentiated thyroid cancer using 124I PET imaging.* J Nucl Med, 2014. **55**(11): p. 1759-65.
18. Jentzen, W., *An improved iterative thresholding method to delineate PET volumes using the delineation-averaged signal instead of the enclosed maximum signal.* J Nucl Med Technol, 2015. **43**(1): p. 28-35.
19. Greene, F.L., et al., *AJCC Cancer Staging Atlas*. 2006, New York: Springer.
20. Jentzen, W., L. Freudenberg, and A. Bockisch, *Quantitative imaging of (124)I with PET/ CT in pretherapy lesion dosimetry. Effects impairing image quantification and their corrections.* Q J Nucl Med Mol Imaging, 2011. **55**(1): p. 21-43.
21. Jentzen, W., et al., *Optimized 124I PET dosimetry protocol for radioiodine therapy of differentiated thyroid cancer.* J Nucl Med, 2008. **49**(6): p. 1017-23.
22. Stabin, M.G., R.B. Sparks, and E. Crowe, *OLINDA/EXM: the second-generation personal computer software for internal dose assessment in nuclear medicine.* J Nucl Med, 2005. **46**(6): p. 1023-7.
23. Hanley, J.A. and B.J. McNeil, *The meaning and use of the area under a receiver operating characteristic (ROC) curve.* Radiology, 1982. **143**(1): p. 29-36.
24. Youden, W.J., *Index for rating diagnostic tests.* Cancer, 1950. **3**(1): p. 32-5.

25. Lassmann, M., et al., *EANM Dosimetry Committee series on standard operational procedures for pre-therapeutic dosimetry I: blood and bone marrow dosimetry in differentiated thyroid cancer therapy.* Eur J Nucl Med Mol Imaging, 2008. **35**(7): p. 1405-12.
26. Verburg, F.A., et al., *I-131 activities as high as safely administrable (AHASA) for the treatment of children and adolescents with advanced differentiated thyroid cancer.* J Clin Endocrinol Metab, 2011. **96**(8): p. E1268-71.
27. Verburg, F.A., et al., *Dosimetry-guided high-activity (131)I therapy in patients with advanced differentiated thyroid carcinoma: initial experience.* Eur J Nucl Med Mol Imaging, 2010. **37**(5): p. 896-903.
28. Wierts, R., et al., *Dosimetry in molecular nuclear therapy.* Methods, 2011. **55**(3): p. 196-202.
29. Nagarajah, J., et al., *Diagnosis and dosimetry in differentiated thyroid carcinoma using 124I PET: comparison of PET/MRI vs PET/CT of the neck.* Eur J Nucl Med Mol Imaging, 2011. **38**(10): p. 1862-8.

Supplemental materials

TABLE S3.1. Primary data of all patients and all analysed lesions

Patient number	Gender: Male (M) / Female (F)	Variant: Papillary (P) / Follicular (F)	TNM Stage	Lesion number	Lesion type: Remnant (R)/ Metastasis (M)	Lesion volume (mL)	Lesion absorbed dose per I-131 activity (Gy/GBq)	Lesion absorbed dose (Gy)	Complete lesion response (Y/N)
1	M	P	1	1	R	0.47	187	519	Y
				2	R	0.37	23.2	64.4	N
2	F	P	4	1	R	0.15	72.3	201	Y
				2	R	0.15	2.3	6.5	N
				3	R	0.15	19.1	53.1	Y
				4	M	0.15	1.0	2.8	Y
				5	M	0.15	0.7	2.0	Y
3	M	P	3	1	R	0.39	20.7	57.3	N
				2	R	0.43	5.9	16.3	N
4	F	F	4	1	M	0.73	6.7	37.2	N
				2	M	2.91	2.1	11.8	N
				3	M	0.66	2.0	10.9	N
				4	R	4.34	5.7	31.7	Y
				5	M	9.81	1.2	6.4	N
				6	M	0.50	1.8	9.9	N
				7	M	19.4	1.3	7.3	N
				8	M	1.73	1.6	8.7	N
				9	M	12.9	0.9	5.0	N
				10	M	1.83	6.9	38.4	N
5	F	P	1	1	R	0.96	370	$1.03 \cdot 10^3$	Y
				2	R	0.15	10.7	29.6	Y
				3	M	0.15	13.4	37.2	Y
				4	M	0.15	6.2	17.3	N
				5	M	0.24	1.6	4.5	N
				6	M	0.15	2.0	5.6	Y
6	M	F	1	1	R	5.65	111	309	N
				2	R	2.22	150	416	Y
				3	R	0.15	22.0	61.1	Y
				4	R	0.15	19.4	53.9	N
				5	R	0.26	18.7	51.9	N
7	F	F	1	1	R	0.36	15.4	42.7	N
				2	R	0.15	2.1	5.8	Y
				3	R	0.15	1.8	5.0	Y
8	F	F	4	1	R	1.11	311	$1.72 \cdot 10^3$	Y
				2	R	0.84	268	$1.49 \cdot 10^3$	N
				3	M	0.60	147	813	Y

Patient number	Gender: Male (M) / Female (F)	Variant: Papillary (P) / Follicular (F)	TNM Stage	Lesion number	Lesion type: Remnant (R)/ Metastasis (M)	Lesion volume (mL)	Lesion absorbed dose per I-131 activity (Gy/GBq)	Lesion absorbed dose (Gy)	Complete lesion response (Y/N)
				4	M	2.16	20.4	113	N
				5	M	0.15	34.6	192	N
9	M	P	1	1	R	1.44	258	286	Y
				2	R	0.15	197	219	N
				3	R	0.23	37.7	41.9	N
				4	R	0.15	57.3	63.6	N
				5	R	0.15	22.1	24.6	N
10	F	P	3	1	M	0.15	2.2	6.2	Y
				2	R	0.26	189	523	Y
				3	R	0.34	276	766	Y
				4	R	0.15	108	301	Y
11	M	P	4	1	R	0.28	228	634	Y
				2	R	0.15	5.8	16.1	Y
				3	R	0.15	47.9	133	Y
12	F	F	1	1	R	0.15	89.2	247	Y
				2	R	0.15	160	443	Y
13	F	P	1	1	M	1.01	487	$1.35 \cdot 10^3$	Y
				2	M	0.15	234	650	Y
				3	M	0.15	181	502	Y
				4	M	0.15	84.3	234	Y
				5	M	0.65	190	528	Y
				6	M	0.35	225	624	Y
				7	R	0.92	483	$1.34 \cdot 10^3$	Y
14	F	F	4	1	M	0.15	$1.50 \cdot 10^3$	$4.62 \cdot 10^3$	Y
				2	M	0.15	629	$1.75 \cdot 10^3$	Y
				3	R	0.15	665	$1.85 \cdot 10^3$	Y
				4	R	0.19	$3.99 \cdot 10^3$	$1.11 \cdot 10^4$	Y
15	M	P	1	1	M	0.15	24.0	66.5	Y
				2	R	0.55	$1.46 \cdot 10^3$	$4.05 \cdot 10^3$	Y
				3	R	0.15	$2.31 \cdot 10^3$	$6.41 \cdot 10^3$	Y
				4	R	0.15	23.1	64.2	Y
				5	R	0.15	238	659	Y
16	F	F	4	1	M	0.52	6.8	25.2	N
17	F	F	2	1	R	0.15	1.6	8.8	Y
18	F	P	1	1	R	0.15	124	344	Y
				2	R	0.38	105	292	Y
				3	R	0.15	72.1	200	Y
				4	R	0.46	406	$1.13 \cdot 10^3$	Y
				5	R	0.15	300	832	Y

Patient number	Gender: Male (M) / Female (F)	Variant: Papillary (P) / Follicular (F)	TNM Stage	Lesion number	Lesion type: Remnant (R)/ Metastasis (M)	Lesion volume (mL)	Lesion absorbed dose per I-131 activity (Gy/GBq)	Lesion absorbed dose (Gy)	Complete lesion response (Y/N)
19	F	P	1	1	R	0.26	848	$2.35 \cdot 10^3$	Y
				2	R	0.15	58.2	162	Y
				3	R	0.15	98.4	273	Y
				4	R	0.15	8.2	22.7	Y
20	F	F	1	1	R	0.15	36.6	101	Y
				2	R	0.15	2.7	7.4	Y
21	F	F	3	1	R	0.15	178	493	Y
				2	R	0.15	91.3	253	Y
				3	R	0.15	8.7	24.2	Y
				4	R	0.15	3.8	10.6	Y
22	F	P	3	1	M	0.15	64.0	177	Y
				2	M	0.15	17.6	48.7	Y
				3	M	0.15	23.0	63.9	Y
				4	M	0.15	23.1	64.0	Y
				5	M	0.15	3.1	8.7	Y
				6	M	0.15	6.3	17.6	Y
				7	R	0.15	21.2	58.8	Y
				8	M	0.15	15.1	42.0	Y
				9	R	0.15	26.5	79.5	Y
				10	R	0.24	5.9	16.4	Y
				11	R	0.15	11.9	33.1	Y
				12	R	0.15	2.0	5.4	Y
				13	R	0.34	5.5	15.4	Y
23	F	P	1	1	R	0.15	2.6	7.2	Y
				2	R	0.15	27.4	76.1	Y
				3	R	0.15	5.7	15.8	Y
24	F	P	3	1	R	0.15	32.8	91.1	Y
				2	R	0.15	66.5	185	N
25	M	P	3	1	M	0.15	95.8	266	Y
				2	M	0.15	4.7	13.1	Y
				3	M	0.15	1.7	4.6	Y
				4	M	0.15	5.2	14.4	Y
				5	R	0.15	117	325	Y
				6	R	0.15	48.4	134	Y
				7	R	0.15	14.6	40.4	Y
				8	R	0.15	49.7	138	Y
26	F	P	3	1	R	0.32	69.9	194	Y
				2	R	0.15	2.3	6.3	Y
27	F	P	2	1	R	0.24	48.1	133	Y
				2	R	0.19	110	305	Y

Patient number	Gender: Male (M) / Female (F)	Variant: Papillary (P) / Follicular (F)	TNM Stage	Lesion number	Lesion type: Remnant (R)/ Metastasis (M)	Lesion volume (mL)	Lesion absorbed dose per I-131 activity (Gy/GBq)	Lesion absorbed dose (Gy)	Complete lesion response (Y/N)
28	F	P	1	1	R	0.15	143	396	Y
				2	R	0.15	52.3	145	Y
				3	R	0.15	1.8	5.0	Y
29	M	P	3	1	R	0.15	29.2	81.0	Y
				2	R	0.15	19.7	54.8	Y
				3	M	0.28	20.6	57.1	Y
				4	R	0.29	60.8	169	Y
				5	R	0.15	90.8	252	Y
30	F	P	1	1	R	0.25	277	769	Y
				2	R	0.15	240	666	Y
				3	R	0.15	3.6	10.1	Y
31	F	F	1	1	M	0.15	13.9	38.5	Y
				2	R	1.52	12.9	35.7	Y
				3	R	0.15	10.2	28.2	Y
32	F	F	3	1	R	0.28	250	694	Y
				2	R	0.15	104	289	Y
				3	R	0.15	42.0	116	Y
33	F	F	3	1	R	1.40	279	775	Y
34	M	P	3	1	R	0.15	143	396	Y
				2	R	0.93	141	391	Y
				3	M	0.15	12.2	33.8	Y
				4	R	0.15	7.3	20.3	Y
35	F	P	3	1	M	1.77	15.1	42.0	Y
				2	M	0.15	38.5	107	Y
				3	R	0.30	0.8	2.3	Y
				4	R	0.15	51.6	59.9	Y
36	F	P	3	1	R	0.15	12.2	34.0	Y
37	F	F	3	1	R	1.18	580	$1.61 \cdot 10^3$	Y
				2	R	0.23	462	$1.28 \cdot 10^3$	Y
				3	R	0.20	41.3	115	Y
38	F	P	2	1	R	0.15	$1.13 \cdot 10^3$	$3.15 \cdot 10^3$	Y
				2	R	0.15	35.5	98.5	Y
				3	R	0.15	56.4	156	Y
39	F	F	1	1	R	0.15	$4.07 \cdot 10^3$	$1.13 \cdot 10^4$	Y
				2	R	0.15	339	941	Y
40	F	P	1	1	R	0.61	$1.37 \cdot 10^3$	$3.81 \cdot 10^3$	Y
				2	R	0.48	363	$1.01 \cdot 10^3$	Y
41	M	P	3	1	R	0.53	804	$2.23 \cdot 10^3$	Y
				2	R	0.15	17.4	48.2	Y

Patient number	Gender: Male (M) / Female (F)	Variant: Papillary (P) / Follicular (F)	TNM Stage	Lesion number	Lesion type: Remnant (R)/ Metastasis (M)	Lesion volume (mL)	Lesion absorbed dose per I-131 activity (Gy/GBq)	Lesion absorbed dose (Gy)	Complete lesion response (Y/N)
42	M	P	1	1	R	0.58	12.7	35.2	Y
	F	P	1	1	R	1.10	$1.15 \cdot 10^3$	$3.20 \cdot 10^3$	Y
				2	R	0.15	177	491	Y
				3	R	0.15	325	903	Y
				4	R	0.15	192	533	Y
44	F	F	2	1	R	0.97	478	$1.33 \cdot 10^3$	Y
				2	R	0.48	$1.29 \cdot 10^3$	$3.58 \cdot 10^3$	Y
45	F	P	1	1	R	0.34	732	$2.03 \cdot 10^3$	Y
				2	R	0.56	281	781	Y
46	F	F	1	1	R	0.15	496	$1.38 \cdot 10^3$	Y
				2	R	0.15	$2.31 \cdot 10^3$	$6.41 \cdot 10^3$	Y
				3	R	0.15	526	$1.46 \cdot 10^3$	Y
				4	R	0.15	650	$1.80 \cdot 10^3$	Y
47	F	P	3	1	R	0.15	23.4	130	Y

Chapter 4

Impact of prompt gamma coincidence correction on absorbed dose estimation in differentiated thyroid cancer using ^{124}I PET/CT

R. Wierts, M. Conti, A.G.G. Claessen, K. Herrmann, G.J. Kemerink, I. Binse, J.E. Wildberger, F.M. Mottaghy, W.H. Backes, W. Jentzen

In submission

Abstract

^{124}I PET/CT is increasingly used in the absorbed dose estimation in the radioiodine treatment of differentiated thyroid cancer (DTC). However, ^{124}I possesses a complicated decay scheme and produces prompt gamma coincidences (PGCs), resulting in a possible bias in the absorbed dose estimation. The aim of this study is to investigate the effect of a sinogram-based PGC correction approach on the absorbed dose estimation in ^{124}I PET/CT DTC imaging.

Methods

First, phantom measurements were performed on a Siemens Biograph mCT PET/CT system. An adapted NEMA IEC body phantom was used containing seven spheres of varying diameters (range: 6.6-37 mm). The spheres and background compartment were filled with a ^{124}I solution, resulting in a low (9.4:1) and high sphere-to-background activity concentration ratio (750:1). Second, ^{124}I PET/CT images of 24 DTC patients showing a total of 66 lesions were included. All images were reconstructed with (PGC_{on}) and without PGC correction (PGC_{off}) implemented on the PET/CT system. For the phantom measurements, sphere recovery coefficient (RC) values were determined and background uniformity was quantified using the coefficient-of-variation (COV). For the patient measurements, the impact of the PGC correction was assessed by calculating the percentage difference in lesion uptake and lesion absorbed dose.

Results

PGC correction provided a lower COV of 14.5% compared to 17.6% for PGC_{off}. Compared to the PGC_{off} values, PGC_{on} sphere RC values were systematically increased with approximately 2.5% for the largest spheres and up to 70% for the smallest spheres. However, even with PGC correction, the RC values were still 15-20% underestimated for the largest spheres. For the patient data, PGC correction resulted on average in a small but significant increase in ^{124}I uptake ($P < 0.005$) and lesion dose ($P = 0.008$) of approximately 3%. However, the percentage difference in lesion dose ranged from -19% to 50% showing that PGC correction had a variable and large impact on calculated lesion absorbed dose for a few single lesions.

Conclusion

PGC correction resulted in significant higher sphere RC values, ^{124}I lesion uptake and lesion dose and should be applied whenever available.

Introduction

Total thyroidectomy is the preferred surgical procedure in differentiated thyroid cancer (DTC) followed by radioiodine treatment 4-6 weeks after surgery [1]. In radioiodine treatment, therapeutic amounts of ^{131}I are administered for 1) eliminating local regional lymph node metastases and distant metastases (lesions) 2) ablation of possible thyroid remnant tissue, 3) elimination of potential residual microscopic tumour deposits [2]. The absorbed (radiation) dose delivered to lesions and thyroid remnants has been established as the most relevant quantity that correlates with lesion response [3-5]. In a theranostic approach, pre-therapeutic ^{124}I PET/CT dosimetry is considered the preferred methodology to assess absorbed dose to lesions in high-risk DTC patients and has been shown to provide prognostic information on lesion response [6].

Compared to the most commonly used PET radionuclide ^{18}F, which is a pure positron (β^+) emitter (β^+ end-point energy: 0.63 MeV, abundance: 97%), ^{124}I exhibits unfavourable decay properties (Figure 4.1A). First, due to its relatively low positron yield of 22.5%, the count rate sensitivity per activity is more than approximately four times lower compared to ^{18}F. Second, due to the high end-point energy of the emitted positrons (β^+_1: 2.138 MeV, 10.7%; β^+_2: 1.535 MeV, 11.7%), the effective spatial resolution of ^{124}I PET imaging is 0.5 – 1.0 mm worse than ^{18}F [7-9]. Third, ^{124}I is not a pure positron emitter. Approximately half of the emitted positrons are in cascade with so-called prompt gamma photons having an energy of 603 keV. As this photon energy is close to the energy of the 511 keV annihilation photons, it falls within the energy window of current clinical PET systems, resulting in the detection of spurious coincidence events which are termed prompt gamma coincidence (PGC) events in reference to the literature [10] (Figure 4.1B). In addition, PGC events can also occur from the cascade of (scattered high-energy) emitted gamma photons following electron capture (EC).

PGC correction is mandatory to improve image quantification and image quality. It has been demonstrated [11] that the location of the PGC events are spread all over the PET field of view and produce higher artificial background level in the sinogram space. The latest generation PET/CT scanners use a single-scatter simulation correction approach that includes a scaling factor to match the model-based scatter contribution to the actual amount of scatter derived from the measured emission sinograms. The scaling factor is derived from sinogram tail fitting outside the patient body. As a consequence, in the presence of higher artificial sinogram background, the single-scatter simulation correction approach overestimates, for instance, the amount of scatter in the central part of the image [12, 13] as well as produces a minor but measurable underestimation of approximately 10% in ^{124}I activity concentration in hot-spot imaging [14, 15].

A

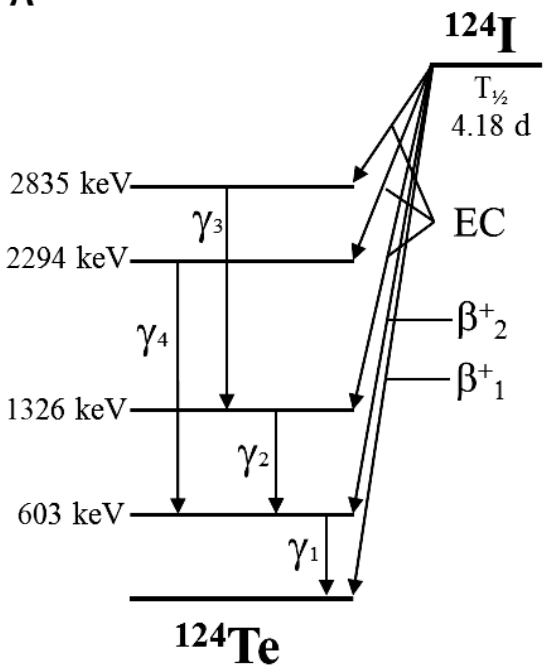

	Energy (keV)	Yield (%)
β^+_1	2138†	10.7
β^+_2	1535†	11.7
$\gamma^{\pm}$	511	45
γ_1	603	62.9
γ_2	723	10.4
γ_3	1509	3.3
γ_4	1691	11.2

B

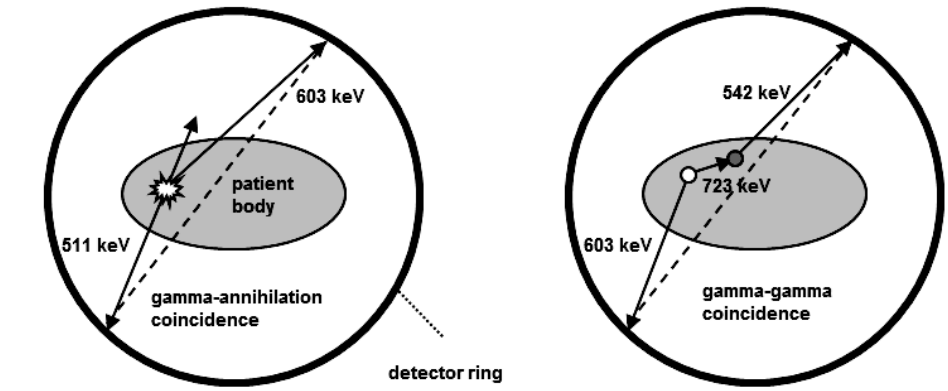

FIGURE 4.1. A) Simplified decay scheme of ^{124}I, including positron emission and electron capture (EC), and decay characteristics. End-point-energies for the beta particles are listed. B) Illustration of PGC event caused by the 603-keV gamma photon in cascade with the β^+_2 positron decay (left) and by a cascade of (scattered high-energy) gamma photons emitted after EC (right).

In recent years, several strategies for reducing or subtracting PGC events have been proposed for ^{124}I and have recently been summarized in a review article [12]. Sinogram-based subtraction of PGC events is a promising approach besides other techniques

(energy window, kernel model, Monte Carlo approach). Basically, the prompt gamma contribution is estimated using the emission data in the radial extremities (tails) of the sinogram data outside the patient, where no source of radioactivity is present. Subtraction of a simple uniform background [16] or a linear or polynomial [17] fit to the tails of the sinogram have been proposed for ^{124}I. A method combining a scaled randoms estimate added to the simulated scatter distribution profile to match the tails of the sinogram has been patented [18] by Siemens and implemented on commercially available PET/CT and PET/MRI systems.

In ^{124}I phantom measurements, the application of PGC correction approaches has been shown to result in both an improvement in image quality, such as background uniformity and lesion contrast recovery, and image quantitation measured by sphere recovery coefficient (RC) values [19, 20]. However, the influence of the PGC correction approach on patient data and, in particular, its impact on lesion dosimetry in DTC patients has not been investigated yet. As in DTC patients ^{124}I uptake is restricted to small foci with negligible background radioactivity, the impact of the PGC correction approach may differ from standard phantom measurements.

Therefore, the aim of this study was to evaluate the impact of the PGC correction method implemented on the Siemens mCT system. First, phantom measurements were performed using a typical clinical imaging protocol and a protocol with a high counting statistics to study the influence of the PGC correction technique on focal ^{124}I lesion uptake. Second, the impact of the PGC correction method on measured ^{124}I lesion uptake and calculated lesion absorbed dose was evaluated using ^{124}I PET/CT images from DTC patients.

Materials and methods

Scanner

All measurements were performed on a Biograph mCT PET/CT system (Siemens Healthcare GmbH, Erlangen, Germany). The system consisted of a 128-slice CT scanner (SOMATOM Definition AS) and a 21.8 cm axial field of view PET system equipped with lutetium oxyorthosilicate (LSO) scintillation detectors allowing PET time-of-flight (ToF) reconstruction. PET acquisitions were performed with an energy window of 435–650 keV and a coincidence timing window of 4.1 ns.

PGC correction method

For the Biograph mCT PET/CT system, a PGC correction method is by default implemented in the PET reconstruction algorithm for radionuclides emitting prompt gammas such as ^{124}I or ^{82}Rb [18]. In the PGC correction approach, first, PET emission sinogram

data normalized for PET detector sensitivity, neither corrected for scatter nor for attenuation, are calculated. A scatter sinogram is estimated from a single-scatter simulation based on the attenuation and the normalized emission sinograms. Next, sinogram tails are located from the attenuation and scatter sinograms. Randoms are estimated from the measured delayed coincidences and then smoothed. The randoms sinogram is used as a model of the prompt gamma contribution. The background signal present in the emission sinogram is modelled as a linear combination of randoms and scatter from least-squares fit performed in the sinogram tail area. Finally, three dimensional PET images are reconstructed using the iterative ordinary Poisson ordered-subsets expectation maximization (OP-OSEM3D) PET reconstruction algorithm, where the sinogram background estimate includes randoms, scatter and prompt gammas.

Phantom measurements

Phantom preparation

Phantom measurements were performed using an adapted NEMA IEC body phantom consisting of a torso-shaped background compartment containing seven fillable spheres (diameter: 6.6, 9.7, 12.6, 15.1, 22.2, 28.0 and 37.0 mm) of which the largest sphere was placed centrally within the torso phantom. ^{124}I activity was determined with a calibrated dose calibrator (CRC-15R; Capintec) using a standardized measurement condition described elsewhere [14]. To simulate high focal ^{124}I lesion uptake and low background radioactivity typically encountered in DTC patients, all spheres were homogeneously filled with an aqueous ^{124}I solution. The sphere and background radioactivity concentrations were 33.81 kBq/mL and 0.045 kBq/mL, respectively, resulting in a signal-to-background ratio of 750:1. In addition, the same phantom was prepared with a higher radioactivity background level (sphere and background radioactivity concentrations of 40.94 kBq/mL and 4.36 kBq/mL, respectively, yielding a signal-to-background ratio of 9.4:1).

Phantom image acquisition and reconstruction

Both the low- and high-background radioactivity phantoms were scanned with a low-dose helical CT scan (120 kVp, 15 mAs) followed by a single-bed PET acquisition of 2 minutes corresponding to a typical PET acquisition time used in clinical routine whole body PET/CT imaging in DTC. These measurements are termed clinical phantom measurements. In addition, single-bed high counting statistics PET acquisitions of 60 minutes were performed for both phantoms and are referred to as high-statistics phantom measurements.

For all phantom measurements, PET images were reconstructed both with (PGC_{on}) and without (PGC_{off}) the PGC correction approach using off-line PET reconstruction software (E7tools; Siemens). PET image reconstruction was performed with the default ToF-based OP-OSEM3D reconstruction algorithm supplied by the manufacturer using 2

iterations, 21 subsets, a 4 mm Gaussian filter and almost cuboid-shaped voxels of 2 × 2 × 2 mm^3.

Phantom analysis

Background quantitative accuracy and uniformity were determined for the high-statistics, high-background phantom measurement for PGC_{on} and PGC_{off} images. Background quantitative accuracy was calculated as the percentage difference in measured mean radioactivity concentration, determined from a circular region of interest (ROI) having a diameter of 18 cm shown in Figure 4.2, with respect to the prepared background radioactivity concentration. In addition, nine circular ROIs with a diameter of 4 cm were drawn as shown in Figure 4.2.

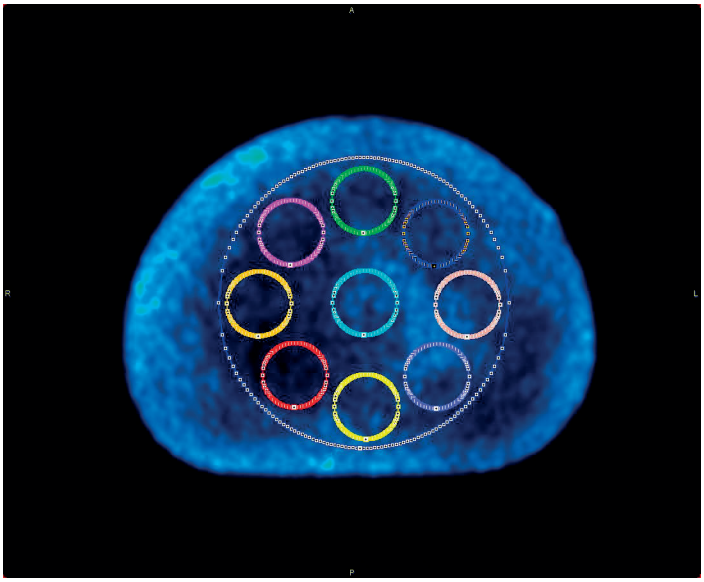

FIGURE 4.2. Axial slice image of phantom background compartment reconstructed with PGC correction. Background quantitative accuracy was assessed using the large 18 cm diameter circular ROI. The nine 4 cm ROIS were used to assess background uniformity.

For each ROI, the mean radioactivity concentration was determined. Background uniformity was assessed using the coefficient of variation (COV) which was calculated from the standard deviation (SD) and average value (μ) of the mean radioactivity concentration measured in the nine ROIs according to COV = SD/μ × 100%.

Sphere RC were determined using three measures for the PET radioactivity concentration. First, the average activity concentration was measured in a 10 mm diameter spherical volume of interest (VOI), located in the center of each sphere and is referred to as peak activity concentration (C_{peak}). Second, the average activity concentration of a VOI, consisting of a 3D isocontour containing all voxels with an activity concentration

equal to or higher than 70% of the maximum voxel value which was termed 70% threshold activity concentration ($C_{70\%}$), was assessed. Third, the maximum voxel value (C_{max}) was determined. To avoid bias in VOI position, all VOIs were drawn on the PGC_{on} images and copied directly to the PGC_{off} images. For the high-statistics phantom measurements, RC values were calculated by dividing the measured activity concentration (C_{max}, C_{peak} and $C_{70\%}$) by the true activity concentration. In addition, for the clinical phantom measurements, the percentage difference in activity concentration measured in the PGC_{on} images was calculated relative to the PGC_{off} images.

Patient measurements

Patients

In total, 24 patients (14 females, 10 males) who underwent ^{124}I PET/CT examination following total thyroidectomy and prior to radioiodine therapy were included. The mean age ± SD was 54.8 ± 23.1 years (females: 54.9 ± 26.6 years, males: 54.5 ± 20.0 years). Patient preparation was performed by recombinant human stimulating hormone (rhTSH) or thyroid hormone withdrawal. Approximately 25 MBq ^{124}I was orally administered. All patients provided written informed consent and the study was approved by the local ethic research committee.

Patient image acquisition and reconstruction

PET/CT acquisition was performed 24 and 120 hours after ^{124}I administration. PET/CT images were performed from head to thigh in supine position with arms up. Low-dose helical CT acquisition (120 kVp, 15 mAs) was followed by whole body PET scanning using a PET acquisition time of 2 minutes per bed position.

PGC_{on} and PGC_{off} PET images were retrospectively reconstructed using identical reconstruction parameters as for the phantom image reconstructions.

Patient image analysis

Each identified iodine-avid lesion was categorized as either a thyroid remnant, a lymph node or a bone metastasis based on its localization. Similar to the phantom measurements, the three types of activity concentration measures (C_{max}, C_{peak}, $C_{70\%}$) were ascertained for each lesion for PGC_{on} and PGC_{off} images. For all activity concentration measures, the percentage difference in activity concentration measured in the PGC_{on} images was calculated relative to the values derived from PGC_{off} images. In addition, Bland-Altman plots were created, showing the percentage differences as a function of the lesion activity concentration.

The impact of the PGC correction approach on the estimated lesion absorbed dose for ^{131}I was also investigated. Specifically, the peak ^{124}I activity concentration (C_{peak}) – as an example for an average activity concentration generally used in the estimation of the lesion absorbed dose – was used to calculate the projected ^{131}I uptake value per gram

of tissue at 24 h and 120 h. For each lesion, the lesion dose per administered activity (LDpA) of a standard 0.52 mL lesion volume was calculated in Gy/GBq using the methodology described by Jentzen et al. [21]. For each lesion, the percentage difference between PGC_{on} and PGC_{off} on the LDpA was determined.

Statistical analysis

For the patient data, statistical significance testing for all percentage difference measures (C_{max}, C_{peak}, $C_{70\%}$ and LDpA) between PGC_{on} and PGC_{off} was performed in SPSS version 23 (IBM Corp.) To correct for the fact that a number of patients showed multiple lesions (repeated measurements), a linear mixed model was applied, using a compound symmetric covariant structure for the repeated measurements, where lesion type was included in the fixed part of the model. Values of *P* less than 0.05 were considered statistically significant.

Results

Phantom measurements

In Figure 4.3 the center slice images of the high-statistics phantom measurements are shown. Without PGC correction, the background radioactivity appeared decreased in the central part of the image, which is especially apparent for the high-background configuration, resulting in an underestimation in measured background activity concentration of 55% and a COV of 17.6%. This effect was explained from the sinogram profiles corresponding to the phantom measurements shown in Figure 4.4. Without PGC correction, the scatter distribution profile did not match the tails of the total emission profile, resulting in an oversubtraction in the central part of the image. With the PGC correction approach, the superposition of the prompt gamma contribution to the estimated scatter distribution profile resulted in an improved scatter correction and background uniformity as can be observed from Figure 4.3 and a lower COV of 14.3%. However, background radioactivity concentration was still underestimated by 30%.

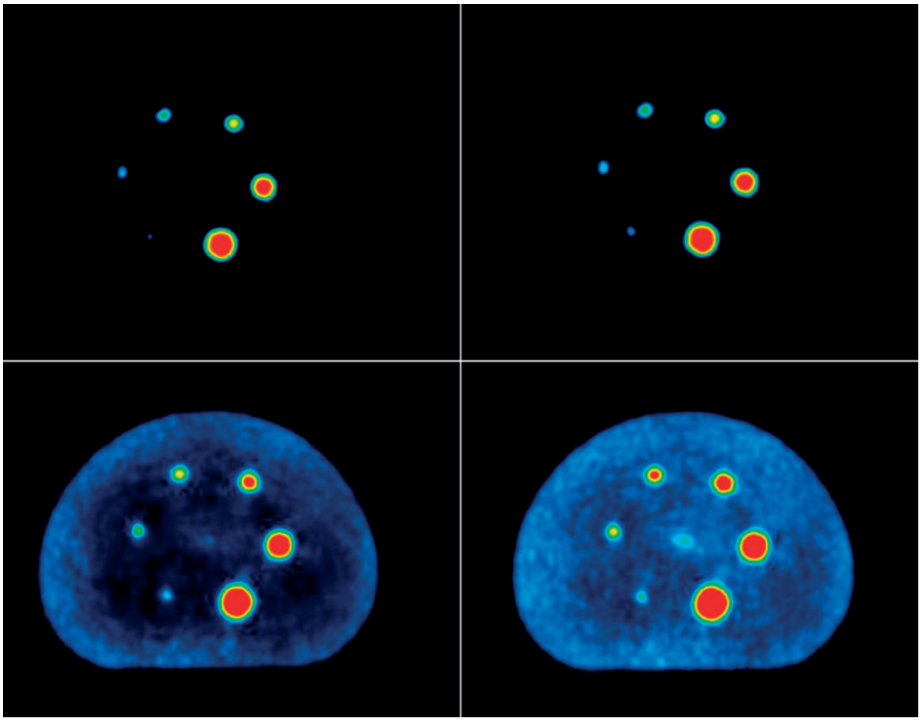

FIGURE 4.3. Center slice images of the high-statistics phantom measurements. The upper figures represent the measurements with low radioactivity background and the lower figures with high radioactivity background. The left figures are reconstructed without PGC correction, whereas in the right figures the default algorithm with PGC correction approach was applied.

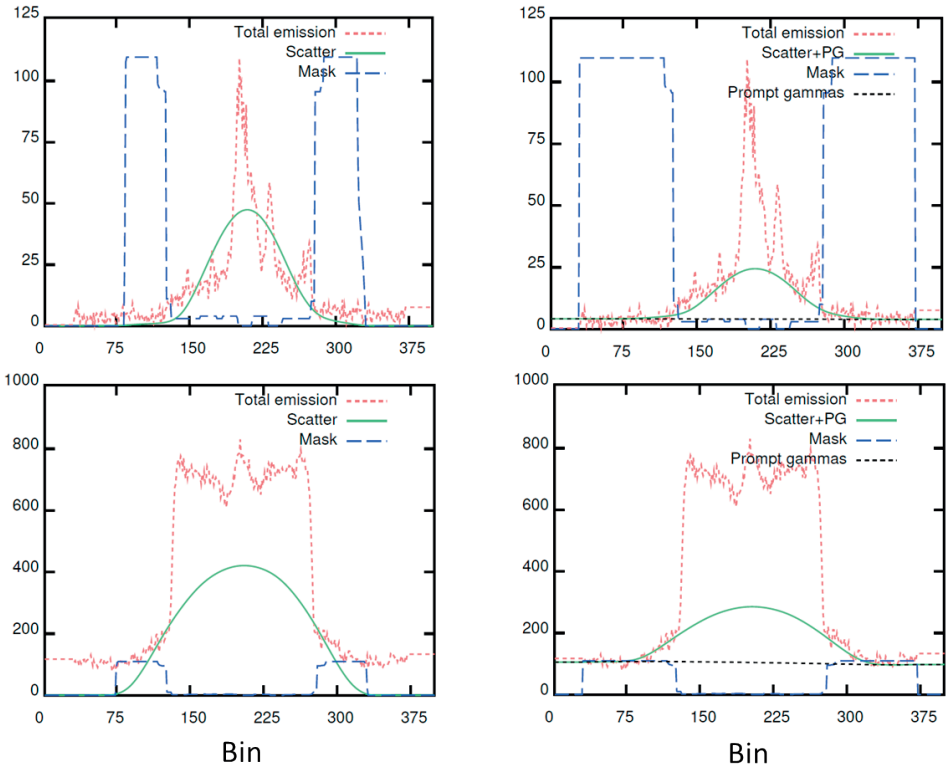

FIGURE 4.4. Sinogram profiles of the high-statistics phantom measurements corresponding to the images shown in Figure 4.3.

The sphere RC calculated from the high-statistics phantom measurements are presented in Figure 4.5. Compared to the PGC_{off} values, PGC_{on} sphere RC values were systematically increased with approximately 2.5% for the largest spheres up to 70% for the smallest spheres both for the measurements with low- and high-background radioactivity concentration. However, even with PGC correction, the RC values were still underestimated with 15-20% for the largest spheres. Similar results were found for the clinical phantom measurements of which the percentage differences between PGC_{on} and PGC_{off} are shown in Table 4.1.

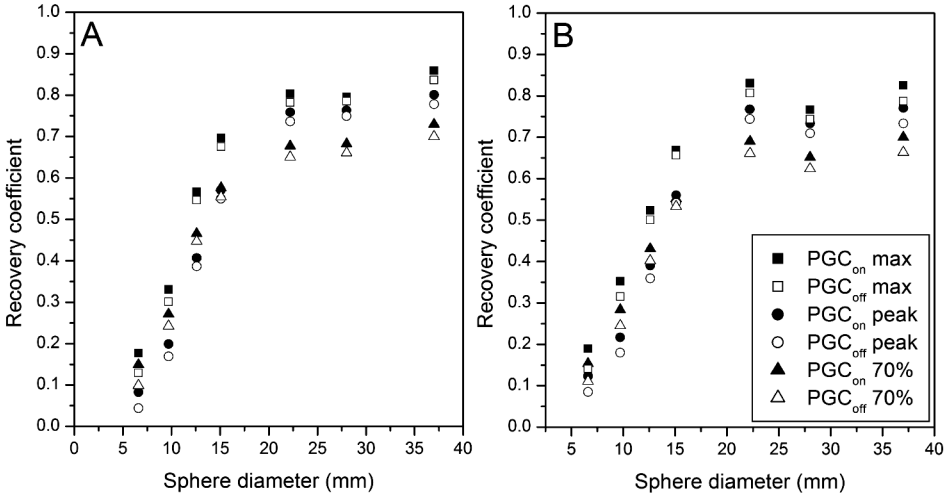

FIGURE 4.5. Recovery coefficients of the high-statistics phantom measurements with low (A) and high (B) background radioactivity concentration as a function of sphere diameter calculated both with (closed symbols) and without (open symbols) PGC correction.

Patient measurements

In total, 66 iodine-avid lesions were identified of which 37 were classified as thyroid remnants, 18 as lymph nodes and 11 as bone metastases. In Figure 4.6 the percentage difference in measured lesion activity concentration (C_{max}, C_{peak} and $C_{70\%}$) between the PGC_{on} and PGC_{off} images is shown for thyroid remnants, lymph nodes and bone lesions for both the 24 and 120 h acquisitions.

As can be seen from Figure 4.6, the percentage difference in C_{max}, C_{peak} and $C_{70\%}$ between PGC_{on} and PGC_{off} is typically smaller than 5% for lesions showing high ^{124}I uptake (activity concentration >50 kBq/mL), whereas for low lesion uptake higher differences up to 350% are observed. These large differences between the two methods in this region can be associated with failures of the background subtraction if the PGC correction is not used.

TABLE 4.1. Percentage difference in activity concentration measured in the PGC_{on} compared to the PGC_{off} images for C_{max}, C_{peak} and $C_{70\%}$.

Sphere diameter (mm)	Difference C_{max} (%)	Difference C_{peak}(%)	Difference $C_{70\%}$(%)
Low-background			
6.6	44.3	70.8	41.9
9.7	8.3	15.2	10.8
12.6	5.3	5.6	4.7
15.1	2.1	3.2	3.4
22.2	2.4	3.4	3.4
28.0	2.7	2.2	2.4
37.0	3.2	3.0	3.6
High-background			
6.6	41.1	48.7	47.4
9.7	14.4	21.2	17.8
12.6	5.3	9.0	7.5
15.1	2.5	4.2	3.7
22.2	4.5	3.9	4.6
28.0	2.9	3.6	3.7
37.0	4.5	5.6	5.2

For both the 24 and 120 h images PGC_{on} resulted in higher values of C_{max} (52/66 and 38/66), C_{peak} (64/66 and 43/66) and $C_{70\%}$ (57/66 and 38/66) compared to PGC_{off} for the majority of lesions (number of lesions for which $PCG_{on} > PGC_{off}$ is shown in parentheses). Although for the 24 h images the percentage difference between PGC_{on} and PGC_{off} was statistically significant for all measurements, the mean percentage difference was less than 3.3% (C_{max}: 1.90%, $P = 0.005$; C_{peak}: 3.29%, $P < 0.001$; $C_{70\%}$: 2.26%, $P = 0.001$). In addition, for bone lesions significantly higher percentage differences in lesion activity concentration were observed than for remnants ($P = 0.014$) and lymph nodes ($P = 0.012$). For the 120 h images the lesion activity concentration was lower compared to the 24 h images, resulting in an increased distribution in percentage difference and no significant differences with respect to either PGC correction or lesion type.

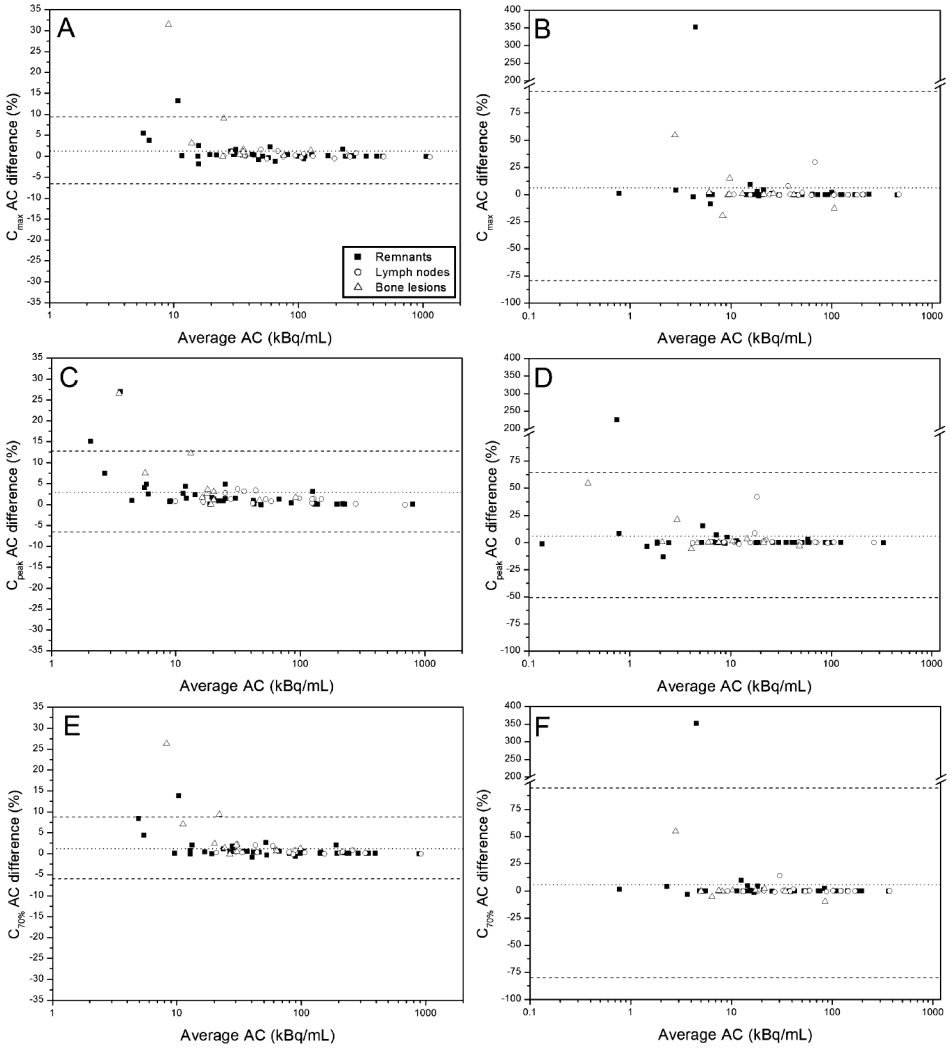

FIGURE 4.6. Bland-Altman plots showing the percentage difference in measured lesion activity concentration (AC) in PGC_{on} and PGC_{off} images for C_{max} (A and B), C_{peak} (C and D) and $C_{70\%}$ (E and F) as a function of the average lesion activity concentration measured with and without PGC correction for both the 24 h (left) and 120 h (right) acquisitions. The dotted line represents the mean percentage difference, the dashed lines the 95% confidence interval.

In Figure 4.7 the percentage difference in calculated ^{131}I LDpA between PGC_{on} and PGC_{off} using the standard volume of 0.52 mL is shown for thyroid remnants, lymph nodes and bone metastases as a function of the LDpA. PGC correction resulted in higher calculated LDpA for the majority of lesions (41/66), resulting in an increase of the mean LDpA of 3.1%, which proved to be statistically significant (P = 0.008). PGC correction did not result in statistically significant differences between the different lesion types. The

impact of PGC correction on the LDpA was highest for low LDpA (< 50 Gy/GBq), resulting in a maximum percentage difference of 50% [range: -19% – 50%].

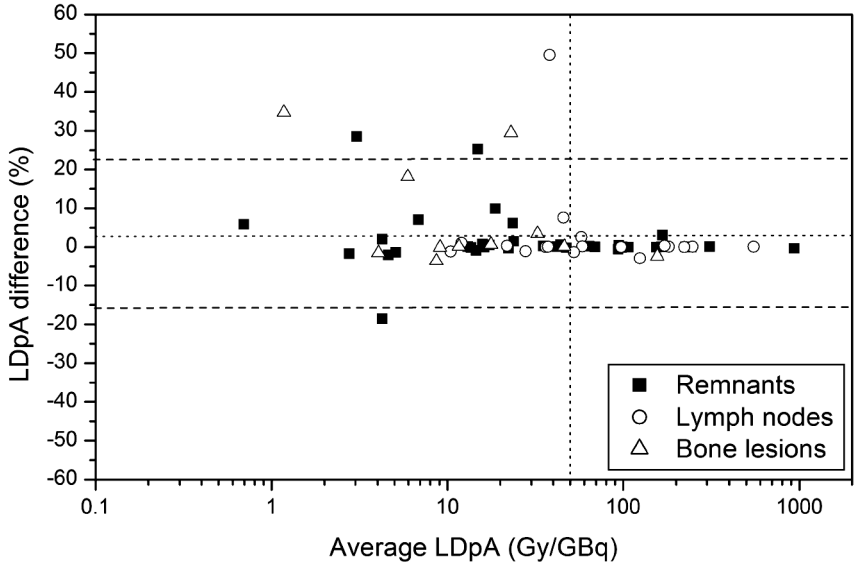

FIGURE 4.7. Bland-Altman plots showing the percentage difference in LDpA between PGC_{on} and PGC_{off} images as a function of the average LDpA measured with and without PGC correction for both remnants, lymph nodes and bone lesions. The horizontal dotted line represents the mean percentage difference, the dashed lines the 95% confidence interval. The vertical dotted line corresponds to LDpA < 50 Gy/GBq below which relatively high differences in calculated lesion absorbed dose between PGC_{on} and PGC_{off} are observed.

Discussion

For the application of personalized radioiodine therapy, accurate pre-therapeutic lesion absorbed dose calculation is essential for estimating the individual therapeutic activity to be administered. Consequently, errors in the predicted lesion absorbed dose calculation may result in under- or overdosing [1, 22]. However, ^{124}I produces a considerable amount of PGC events, resulting in an underestimation of the measured activity concentration [12, 13] and therefore in the absorbed dose estimation. Since the location of PGC events are spread all over the PET field of view [11] it is expected that the impact of PGC events on lesion quantification depends on the ^{124}I radioactivity distribution. As in DTC imaging the ^{124}I radioactivity distribution is limited to a few small foci showing high uptake in the absence of background radiation, the impact of the PGC effect is expected to be less important compared to antibody imaging in which lower lesion uptake is observed in combination with higher background radioactivity levels [13]. Indeed, in our study we found that on average PGC correction resulted only in a small increase in the calculated LDpA of 3.1%, which is considered negligible compared to other sources of uncertainties in the lesion dosimetry calculations (for instance, uncertainties in dose

calibrator measurements, segmented lesion volume and kinetic model used to estimate the residence time). Nonetheless, for a few lesions with a LDpA lower than 50 Gy/GBq, differences up to 50% in the LDpA between PGC_{on} and PGC_{off} are observed. This demonstrates that for these lesions PGC correction is essential and should be applied whenever available.

For the majority of lesions, PGC correction resulted in an increase of ^{124}I lesion uptake (C_{max}, C_{peak} and $C_{70\%}$) lower than 5% for the lesions showing high uptake as shown in Figure 4.6. However, for lesions with low uptake (< 50 kBq/mL) larger differences in measured radioactivity concentration up to 350% were observed. This effect can be explained from the poor counting statistics of these low uptake lesions: in a low counts condition, possible errors in the sinogram tail fitting procedure are amplified if no PGC correction is used, resulting in erroneous scatter correction and more dramatic differences between PGC_{on} and PGC_{off}. Therefore, PGC correction is in particular of importance for lesions showing low ^{124}I uptake, such as bone metastases. In our study we found a significantly higher impact of PGC correction for bone lesions than for thyroid remnants and lymph nodes in the 24 h ^{124}I uptake.

The observed impact of the PGC correction approach in the patient measurements was in good agreement with the phantom measurements. Overall, PGC resulted in a small increase in measured hot spot activity concentration of approximately 2-5%, corresponding to the improvement of PGC correction on ^{124}I RC values reported in literature [19]. However, both for the patient and phantom data relatively large differences between PGC_{on} and PGC_{off} were observed for hot spots with a low amount of total radioactivity, resulting in poor counting statistics as described previously. In phantom data, the largest differences were observed for the smallest spheres as shown in Table 4.1; for patient data we observed an increase in difference with decreasing lesion radioactivity concentration as shown in Figure 4.6. Therefore, we conclude that PGC correction is most important for small lesions showing low ^{124}I uptake.

In the phantom measurements, PGC correction substantially decreased the amount of oversubtraction of the conventional scatter algorithm as reported in literature [12, 13]. This resulted in an improvement of background uniformity as shown by the lower COV values (17.6% versus 14.3%) and systematically higher sphere RC as shown in Figure 4.5 and Table 4.1. However, PGC correction was not perfect as can be observed from some residual background inhomogeneity visible in Figure 4.3. Moreover, even with PGC correction the background radioactivity concentration and RC values of the largest spheres were still underestimated by 30% and 10-15%, respectively, in agreement with values previously reported by Wierts et al. [9]. In contrast to our results, other groups did not report a significant underestimation in measured RC values for ^{124}I compared to ^{18}F [19, 20]. This discrepancy is possibly caused by an inaccurate ^{124}I calibration factor of the dose calibrator, which may have resulted in an under- or overestimation of the true ^{124}I activity concentration. As the low-energy X-ray radiation (27 keV) emitted by ^{124}I are to a substantial degree absorbed in the sample, depending on sam-

ple geometry, sample-specific dose calibrator settings are essential to perform accurate ^{124}I activity measurements [10, 23].

Conclusion

In phantom measurements, PGC correction resulted in significant higher sphere RC values in combination with improved background uniformity. In patients, PGC correction resulted in an overall small increase of 3% in ^{124}I uptake and LDpA. However, for a few lesions showing low LDpA (<50 Gy/GBq), large differences in calculated lesion dose up to 50% were observed, indicating that PGC correction may have an important impact in a personalized radioiodine approach and should be applied whenever available.

Disclosure

M. Conti is an employee of Siemens Healthcare Molecular Imaging.

References

1. Luster, M., et al., *Guidelines for radioiodine therapy of differentiated thyroid cancer.* Eur J Nucl Med Mol Imaging, 2008. **35**(10): p. 1941-59.
2. American Thyroid Association (ATA) Guidelines Taskforce on Thyroid Nodules and Differentiated Thyroid Cancer, Cooper, D.S., et al., *Revised American Thyroid Association management guidelines for patients with thyroid nodules and differentiated thyroid cancer*. Thyroid, 2009. **19**(11): p. 1167-214..
3. Jentzen, W., et al., *Assessment of lesion response in the initial radioiodine treatment of differentiated thyroid cancer using 124I PET imaging.* J Nucl Med, 2014. **55**(11): p. 1759-65.
4. Maxon, H.R., et al., *Relation between effective radiation dose and outcome of radioiodine therapy for thyroid cancer.* N Engl J Med, 1983. **309**(16): p. 937-41.
5. Maxon, H.R., 3rd, et al., *Radioiodine-131 therapy for well-differentiated thyroid cancer--a quantitative radiation dosimetric approach: outcome and validation in 85 patients.* J Nucl Med, 1992. **33**(6): p. 1132-6.
6. Wierts, R., et al., *Dose-Response Relationship in Differentiated Thyroid Cancer Patients Undergoing Radioiodine Treatment Assessed by Means of 124I PET/CT.* J Nucl Med, 2016. **57**(7): p. 1027-32.
7. Kemerink, G.J., et al., *Effect of the positron range of 18F, 68Ga and 124I on PET/CT in lung-equivalent materials.* Eur J Nucl Med Mol Imaging, 2011. **38**(5): p. 940-8.
8. Jentzen, W., et al., *Iodine-124 PET dosimetry in differentiated thyroid cancer: recovery coefficient in 2D and 3D modes for PET(/CT) systems.* Eur J Nucl Med Mol Imaging, 2008. **35**(3): p. 611-23.
9. Wierts, R., et al., *Quantitative performance evaluation of ¹²⁴I PET/MRI lesion dosimetry in differentiated thyroid cancer.* Phys Med Biol, 2017.
10. Jentzen, W., L. Freudenberg, and A. Bockisch, *Quantitative imaging of (124)I with PET/ CT in pretherapy lesion dosimetry. Effects impairing image quantification and their corrections.* Q J Nucl Med Mol Imaging, 2011. **55**(1): p. 21-43.
11. Watson, C.C., et al., *Prompt gamma correction for improved quantification of ^{82}Rb PET.* J Nucl Med, 2008. **49 supplement 1**: p. 64P.
12. Conti, M. and L. Eriksson, *Physics of pure and non-pure positron emitters for PET: a review and a discussion.* EJNMMI Phys, 2016. **3**(1): p. 8.
13. Lubberink, M. and H. Herzog, *Quantitative imaging of 124I and 86Y with PET.* Eur J Nucl Med Mol Imaging, 2011. **38 Suppl 1**: p. S10-8.
14. Jentzen, W., *Experimental investigation of factors affecting the absolute recovery coefficients in iodine-124 PET lesion imaging.* Phys Med Biol, 2010. **55**(8): p. 2365-98.
15. Gregory, R.A., et al., *Optimization and assessment of quantitative 124I imaging on a Philips Gemini dual GS PET/CT system.* Eur J Nucl Med Mol Imaging, 2009. **36**(7): p. 1037-48.
16. Surti, S., R. Scheuermann, and J.S. Karp, *Correction technique for cascade gammas in I-124 imaging on a fully-3D, Time-of-Flight PET Scanner.* IEEE Trans Nucl Sci, 2009. **56**(3): p. 653-660.
17. Sandstrom, M., et al., *Performance of coincidence imaging with long-lived positron emitters as an alternative to dedicated PET and SPECT.* Phys Med Biol, 2004. **49**(24): p. 5419-32.
18. Hayden, C.H.J., M.E. Casey, and C.C. Watsen, *Prompt gamma correction for non-standard I sotopes in a PET scanner.* US Patent 7,894,652, 2011.
19. Preylowski, V., et al., *Is the image quality of I-124-PET impaired by an automatic correction of prompt gammas?* PLoS One, 2013. **8**(8): p. e71729.
20. Braad, P.E., et al., *PET imaging with the non-pure positron emitters: (55)Co, (86)Y and (124)I.* Phys Med Biol, 2015. **60**(9): p. 3479-97.
21. Jentzen, W., et al., *Optimized 124I PET dosimetry protocol for radioiodine therapy of differentiated thyroid cancer.* J Nucl Med, 2008. **49**(6): p. 1017-23.
22. Lassmann, M., et al., *The use of dosimetry in the treatment of differentiated thyroid cancer.* Q J Nucl Med Mol Imaging, 2011. **55**(2): p. 107-15.
23. Beattie, B.J., et al., *A recommendation for revised dose calibrator measurement procedures for 89Zr and 124I.* PLoS One, 2014. **9**(9): p. e106868.

Chapter 5

Quantitative performance evaluation of ^{124}I PET/MRI lesion dosimetry in differentiated thyroid cancer

R. Wierts, W. Jentzen, H.H. Quick, H.J. Wisselink, I.N.A. Pooters, J.E. Wildberger, K. Herrmann, G.J. Kemerink, W.H. Backes, F.M. Mottaghy

Phys Med Biol. 2017 Dec;63(1):015014. doi: 10.1088/1361-6560/aa990b

Abstract

The aim was to investigate the quantitative performance of ^{124}I PET/MRI for pre-therapeutic lesion dosimetry in differentiated thyroid cancer. Phantom measurements were performed on a PET/MRI system (Biograph mMR, Siemens Healthcare) using ^{124}I and ^{18}F. The PET calibration factor and the influence of radiofrequency coil attenuation were determined using a cylindrical phantom homogeneously filled with radioactivity. The calibration factor was 1.00 ± 0.02 for ^{18}F and 0.88 ± 0.02 for ^{124}I. Near the radiofrequency surface coil an underestimation of less than 5% in radioactivity concentration was observed. Soft-tissue sphere recovery coefficients were determined using the NEMA IEC body phantom. Recovery coefficients were systematically higher for ^{18}F compared to ^{124}I. In addition, the six spheres of the phantom were segmented using a PET-based iterative segmentation algorithm. For all ^{124}I measurements, the deviations in segmented lesion volume and mean radioactivity concentration relative to the actual values were smaller than 15% and 25%, respectively. The effect of MR-based attenuation correction (3- and 4-segment μ-maps) on bone lesion quantification was assessed by using radioactive spheres filled with a K_2HPO_4 solution mimicking bone lesions. The 4-segment μ-map resulted in an underestimation of the imaged radioactivity concentration up to 15%, whereas the 3-segment μ-map resulted in an overestimation up to 10%. For twenty lesions identified in six patients, a comparison of ^{124}I PET/MRI to PET/CT was performed with respect to segmented lesion volume and radioactivity concentration. The interclass correlation coefficients showed excellent agreement in segmented lesion volume and radioactivity concentration (0.999 and 0.95, respectively). In conclusion, accurate quantitative ^{124}I PET/MRI with the aim of performing radioiodine pre-therapeutic lesion dosimetry in differentiated thyroid cancer is feasible.

Introduction

Radioiodine therapy, after total thyroidectomy, is the standard adjuvant therapy in differentiated thyroid cancer (DTC) [1]. The radiation absorbed dose delivered to thyroid remnants and lesions (lymph nodes or distant metastases) is considered the most relevant quantity that has been shown to correlate with treatment outcome [2]. In the last decades, several groups have investigated the use of ^{124}I PET(/CT) to assess the lesion absorbed dose delivered in radioiodine therapy [3, 4]. In fact, ^{124}I PET/CT is considered the most accurate method for pre-therapeutic dosimetry assessment in DTC and has been shown to alter patient management [5] and to provide prognostic information on lesion response [6].

Reliable lesion dosimetry requires accurate quantification of lesion volume and ^{124}I uptake at different time points. As a result of the limited soft-tissue contrast, the boundary of tumours and thyroid remnants can generally not be segmented clearly on CT. Therefore, lesion volume segmentation is commonly performed on PET images. However, due to the limited spatial resolution of PET, lesion volume determination, and therefore accurate lesion dosimetry, is only achieved in 25-40% of all iodine-avid lesions [2, 6].

As a result of the superior soft-tissue contrast of MRI over CT, MRI may provide additional diagnostic information in DTC patients. Due to this superiority, Nagarajah et al. [7] concluded that PET/MRI can enhance diagnostic certainty for small lesions and improve pre-therapeutic lesion dosimetry in DTC. However, whereas CT-based PET attenuation correction is straightforward, MR-based attenuation correction is more challenging, in particular for bony structures [8, 9]. Moreover, the presence of radiofrequency (RF) surface coils in the PET field of view (FOV) can degrade PET image quantification [10].

In general, the quantitative performance of PET/MRI systems is assessed for ^{18}F as this is the most commonly used PET radionuclide in clinical practice and readily available. In contrast to ^{18}F which is a pure positron (β^+) emitter (β^+: yield 97%, end-point energy: 0.63 MeV), ^{124}I PET quantification has been shown more difficult mainly due to the higher positron energies (β^+_1: 10.7%, 2.1 MeV; β^+_2: 11.7%, 1.5 MeV) emitted by ^{124}I and the prompt gamma photons (0.603 MeV) emitted in cascade with approximately half of the positrons [11], producing so called prompt gamma coincidences. Although recently the Biograph mMR PET/MRI system image quality of ^{124}I was assessed and compared to ^{18}F [12], quantitative performance for lesion dosimetry in radioiodine treatment has not yet been investigated.

The aim of this study was to investigate the quantitative performance characteristics of PET/MRI with respect to ^{124}I PET lesion dosimetry in radioiodine therapy in DTC patients.

Materials and methods

PET/MRI system

PET/MRI measurements were performed on a 3 Tesla Biograph mMR system having a gradient system with a maximum amplitude of 45 mT/m and a maximum slew rate of 200 (T/m)/s (Siemens Healthcare GmbH, Erlangen, Germany, software version VB20P). PET images were reconstructed using the manufacturer's 3D iterative ordinary Poisson ordered-subsets expectation maximization (OP-OSEM3D) reconstruction algorithm. Unless mentioned otherwise, the default manufacturer's recommendations for image reconstruction were applied: 3 iterations and 21 subsets, cuboid-shaped voxels of 2.0 mm and a 4.0 mm Gaussian smoothing filter. Correction of ^{124}I prompt gamma coincidences was performed using the standard manufacturer's reconstruction software [13].

For attenuation and scatter correction in patients, in general a 4-segment (air, lung, fat and soft-tissue) attenuation map (μ-map) derived from a 3D Dixon-VIBE MR sequence was used. For head-neck imaging, the system provides an alternative 3-segment (air, soft-tissue and bone) μ-map, using an ultrashort echo-time (UTE) MR sequence. For quantitative PET phantom measurements a CT-based (Gemini TF PET/64-slice CT scanner; Philips) μ-map was used for PET attenuation and scatter correction [14].

Radionuclides

All phantom measurements were performed with ^{124}I-sodium iodide (^{124}I-NaI) and compared to ^{18}F-fluorodeoxyglucose (^{18}F-FDG).

Measurement of the absolute ^{124}I activity is crucial for dosimetry quantification and requires a standardized procedure [4, 15]. Radioactivity measurement of syringes used for phantom preparation was performed using a dose calibrator (Isomed 2010; MED, Dresden) that was validated against a high-purity germanium semi-conductor detector (GR1018; Canberra Industries, Connecticut).

Quantitative performance measurements

Calibration factor (CF) and RF coil attenuation

The PET calibration factor was determined using a cylindrical phantom (internal diameter 14 cm, internal length 20 cm) homogeneously filled with radioactivity in aqueous solution. Single-bed PET acquisitions of 7 minutes were performed using a radioactivity concentration of 6.5 kBq/mL for ^{18}F, corresponding to the FDG PET/CT standard operating procedures for quality control of the European association of nuclear medicine (EANM) [16]. As in clinical practice, lower amounts of ^{124}I are administered compared to ^{18}F, an activity concentration of 1.70 kBq/mL was used for ^{124}I. As the CF measurement uncertainty is increased for lower counting statistics, PET acquisition times of

120 minutes were used to obtain similar counting statistics as for the ^{18}F measurements, taking into account both the lower activity concentration and lower positron yield of ^{124}I. For both ^{18}F and ^{124}I, measurements were firstly performed without RF coils as a reference.

To investigate the influence of attenuation of two commercially available Biograph mMR PET-compatible RF coils used for head-neck imaging, the phantom measurements were repeated twice: the first time with the cylindrical phantom placed inside the rigid 16-channel head-neck RF coil, the second time with the small and flexible 4-channel special purpose surface RF coil placed on top of the cylindrical phantom.

For all measurements with and without RF coils, the PET calibration factor *CF* was determined as the mean radioactivity concentration a_{mean} measured in a central cylindrical volume of interest (VOI) (diameter 10 cm, length 15 cm), divided by the prepared or true radioactivity concentration a_{true}:

$$CF = \frac{a_{\mathbf{mean}}}{a_{\mathbf{true}}}. \qquad \text{Eq. 1}$$

The standard deviation (SD) of the CF was determined as the standard deviation of the CF calculated for the individual transversal slices using a circular region of interest with a diameter of 10 cm. Furthermore, for each axial plane five circular regions of interest (ROIs) with a radius of 1.0 cm were drawn as shown in Figure 5.1a. For each ROI and plane number, the ratio of the mean radioactivity concentration measured with RF coil relative to the reference measurement without RF coil was calculated. From these calculated radioactivity concentration ratios, the mean and standard deviation were determined. The 95% uncertainty interval of the radioactivity concentration ratio per plane was calculated as the mean ratio ± 2 standard deviations.

Recovery coefficients using a soft-tissue phantom

Soft-tissue sphere recovery coefficients (RCs) were determined using the NEMA IEC body phantom. This phantom consists of a torso-shaped background compartment containing six fillable spheres (diameter: 10, 13, 17, 22, 28 and 37 mm) and a cylindrical insert filled with polystyrene (internal diameter 44.5 mm). Corresponding to the EANM standard operating procedures for quality control of FDG PET/CT [16], all spheres were homogeneously filled with an aqueous solution having a radioactivity concentration of 13.8 kBq/mL for ^{18}F and 14.0 kBq/mL for ^{124}I. For both radionuclides, measurements were performed without radioactivity present in the background compartment (cold background). In addition, measurements were performed with radioactivity present in the background compartment (hot background), corresponding to a prepared sphere-to-background ratio of 10:1. For accurate assessment of the RC, single-bed PET high counting statistic acquisitions of 30 minutes for ^{18}F and 60 minutes for ^{124}I were performed. The emission time of the ^{124}I measurements was doubled with respect to ^{18}F to (partly) correct for the lower positron yield of ^{124}I.

The mean and maximum radioactivity concentrations were determined by drawing spherical VOIs having a diameter corresponding to the actual sphere diameter. The mean (maximum) recovery coefficients *RC* were calculated by dividing the measured mean (maximum) sphere radioactivity concentration C_{meas} by the prepared or true sphere radioactivity concentration C_{true}:

$$RC = \frac{C_{meas}}{C_{true}}. \quad \text{Eq. 2}$$

Effect of MR-based attenuation correction of bone lesions

Simulation of bone lesions was performed with a bone-tissue phantom by filling the six spheres of the NEMA IEC body phantom with a K_2HPO_4 solution mixed with ^{18}F or ^{124}I. For both radionuclides, a high and low concentration of K_2HPO_4, simulating compact and cancellous bone tissue, was used: 0.84 g/mL and 0.42 g/mL, resulting in CT numbers of 780 HU and 490 HU, respectively. For the high and low concentrations of K_2HPO_4, the radioactivity concentration and acquisition time (within parentheses) was 9.3 kBq/mL (30 min) and 18.8 kBq/mL (15 min) for ^{18}F and 27.9 kBq/mL (20 min) and 14.9 kBq/mL (40 min) for ^{124}I, respectively. The radioactivity concentrations and acquisition times were chosen to obtain similar high counting statistics for the low and high K_2HPO_4 concentration measurements for each radionuclide separately, partly compensating for the lower positron yield of ^{124}I compared to ^{18}F.

PET images were reconstructed using three different μ-maps. First, reference PET images were reconstructed using an original CT-based μ-map of the bone-tissue phantom. Second, to simulate the 4-segment MR-based attenuation correction, in which bone is (incorrectly) classified as soft-tissue, the linear attenuation coefficient of the bony spheres in the original CT-based μ-map was set to that of water. PET images were reconstructed using this adapted μ-map. Third, the 3-segment MR-based attenuation correction was simulated by replacing the linear attenuation correction of the bony spheres with a fixed linear attenuation coefficient of 0.151 cm^{-1}. PET reconstructions were performed using the adapted μ-map.

Spherical VOIs corresponding to the actual sphere dimensions were drawn for all spheres. The percentage deviation in mean radioactivity concentration measured in the reconstructed images using the 3- or 4-segment MR-based μ-map relative to the reference PET images was calculated.

PET-based lesion segmentation

Lesion segmentation method

For reliable lesion dosimetry, accurate volume segmentation of the lesion and its radioactivity concentration are required. In a recent ^{124}I PET/CT study, reliable lesion dosimetry was achieved using a PET-based iterative thresholding algorithm [6]. The method uses the average lesion activity concentration assuming a spherically shaped lesion with

a homogeneous radioactivity concentration [17]. Accounting for the full-width at half maximum (FWHM) spatial resolution of the PET images and background radioactivity level, the segmentation algorithm determines the optimum threshold value for lesion delineation. Besides lesion volume, the method calculates the lesion mean radioactivity concentration, corrected for partial volume effects [17].

PET spatial resolution measurement

The described volume segmentation method requires the effective spatial resolution of the PET images. Therefore, the spatial resolution was measured using a line-source phantom consisting of a cylindrical phantom (diameter 20 cm, length 30 cm) filled with water in which a plastic line source was placed (internal diameter 0.9 mm, length 25 cm). Tangential and radial resolution were measured at 1, 10 and 20 cm distance to the centre of the FOV. Axial resolution was measured at the centre of the FOV and at 9 cm offset. The radioactivity concentration of the line sources was 10 MBq/mL for ^{18}F and 8 MBq/mL for ^{124}I using an acquisition time of 30 minutes and 60 minutes. Except for a 2.0 mm Gaussian smoothing filter, default PET reconstruction settings were used.

For each direction (tangential, radial, axial), the FWHM spatial resolution was calculated by fitting a Gaussian curve through the radioactivity profile of the reconstructed line source using Matlab (The MathWorks Inc). The average spatial resolution was calculated from the spatial resolution values measured at different distances from the centre of the FOV for each direction. Finally, the effective spatial resolution was calculated as the mean value of the average spatial resolution of the three directions.

Lesion volume and radioactivity concentration assessment

The accuracy of the described PET-based iterative segmentation method was investigated for the soft-tissue phantom measurements. To this end, the iterative segmentation method was applied to all spheres using an in-house developed Matlab script. As the segmentation method uses the determined effective spatial resolution, the images were reconstructed with the same reconstruction settings as the spatial resolution measurements. The percentage deviation in segmented lesion volume and mean radioactivity concentration, corrected for partial volume effect, relative to the actual sphere volume and radioactivity concentration were determined.

Clinical ^{124}I PET/MRI lesion quantification using PET/CT as reference

Five DTC patients, who underwent both ^{124}I PET/CT (Biograph mCT; Siemens Healthcare GmbH, Erlangen, Germany) and ^{124}I PET/MRI were analysed. All patients received total thyroidectomy prior to ^{124}I PET imaging. Patient preparation was performed by thyroid hormone withdrawal or recombinant human thyroid stimulating hormone. PET/CT acquisition was performed 24 hours after oral administration of approximately 25 MBq ^{124}I, followed within two hours by PET/MRI acquisition. Patients provided written in-

formed consent to undergo the examinations, and the study was approved by the local ethic research committee.

PET/CT scans were acquired from head to thigh with arms up, using a low-dose CT scan (120 kVp, 15 mAs) and a PET emission time of 2 minutes/bed position typically used in clinical routine whole body PET/CT examinations. In contrast, PET/MRI scans were restricted to the head-neck region with arms down. To achieve optimum PET image quality, PET acquisition was simultaneously performed for the duration of the MRI examinations, which contained a T_1-weighted VIBE sequence (echo time 2.46 ms, repetition time 6.18 ms, flip angle 12°), resulting in long PET acquisition time of 20-30 minutes/bed position. PET image reconstructions were performed with the OP-OSEM3D reconstruction algorithm using 3 iterations, 24 subsets for PET/CT and 3 iterations, 21 subsets for PET/MRI. PET/CT and PET/MRI images had almost cuboid-shaped voxels of 2 mm. For both systems, correction for prompt gamma coincidences was applied for ^{124}I by the manufacturer [13]. As the intrinsic PET spatial resolution of the PET/CT system is slightly lower than the PET/MRI system (5.5 mm versus 5.0 mm at zero smoothing level), different levels of Gaussian smoothing were applied (PET/CT 3.0 mm and PET/MRI 4.0 mm) to achieve almost identical effective spatial resolution (6.3 mm FWHM). As the five DTC patients did not show any bone lesions, additionally one neuro-endocrine patient was included, who was scanned with ^{124}I-meta-iodobenzylguanidine (^{124}I-MIBG) PET/MRI and PET/CT and showed multiple bone lesions. With the exceptions of a higher administered activity of 45 MBq and a whole body PET/MRI acquisition (5 min/bed position), PET acquisition- and reconstruction settings were identical to the DTC patients.

Each ^{124}I-avid lesion identified on both PET/CT and PET/MRI was segmented and the lesion volume and average radioactivity concentration was determined and compared using a Bland-Altman plot. In addition, the interclass correlation coefficient (ICC) was calculated (SPSS, version 23, IBM, Corp.).

Results

Quantitative performance measurements

Calibration factor and MRI coil attenuation

The calibration factors of ^{18}F and ^{124}I without RF coils were 1.00 ± 0.02 and 0.88 ± 0.02, respectively. For both the rigid head-neck coil (^{18}F: 1.02 ± 0.02, ^{124}I: 0.89 ± 0.02) and the flexible RF surface coil (^{18}F: 0.98 ± 0.02, ^{124}I: 0.88 ± 0.02) no substantial deviations of the calibration factor with respect to the reference measurement were observed.

Figure 5.1 shows the ratio of the mean radioactivity concentration measurements with RF coil to the reference measurement without RF coil as a function of the axial plane number. As the ^{18}F and ^{124}I measurements showed comparable results, only the

^{124}I measurements are shown. ^{18}F data are shown in the supplemental material. As can be seen in Figure 5.1a, for the head-neck RF coil no notable deviations of the mean radioactivity concentration with respect to the 95% uncertainty interval were observed for all circular ROIs, indicating that the automatic detection and attenuation correction for the head-neck RF coil worked properly. Figure 5.1b shows at planes 35 to 60, corresponding to the location of the RF surface coil, a small decrease of 5% in mean radioactivity concentration ratio derived from the ROI situated in close proximity to the RF surface coil (ROI1). This decrease is explained by the fact that the PET attenuation caused by the RF surface coil was not taken into account in the attenuation correction during PET image reconstruction.

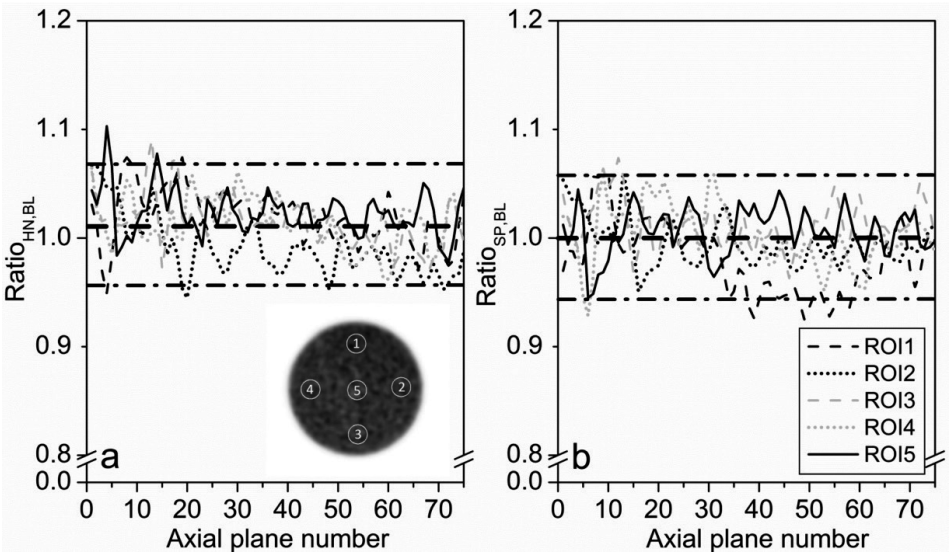

FIGURE 5.1. The influence of RF coil attenuation of the PET signal is assessed using the ratio of the mean ^{124}I radioactivity concentration with RF coil (a: Head-neck coil, b special purpose coil located between plane number 35 and 60) compared to the reference measurement without RF coil measured for all five ROIs shown in the insert of figure a. The horizontal dashed and dash-dotted lines represent the average ratio and 95% uncertainty interval of the radioactivity concentration ratio per plane respectively.

Recovery coefficients

In Figure 5.2 the soft-tissue RC_{mean} and RC_{max} values are shown as a function of the sphere volume. No substantial differences were observed between the measurements with and without background radioactivity. The RC values of ^{18}F are systematically higher compared to ^{124}I. Although for ^{18}F the largest spheres reach an RC_{max} value of unity, for ^{124}I an underestimation of approximately 10% is observed. For ^{124}I larger underestimations up to 38% in RC values with respect to ^{18}F are observed for the smallest sphere, most likely caused by the higher positron range of ^{124}I compared to ^{18}F resulting in a

larger partial volume effect. The centre slice images of the soft-tissue sphere phantom are shown in the supplemental material.

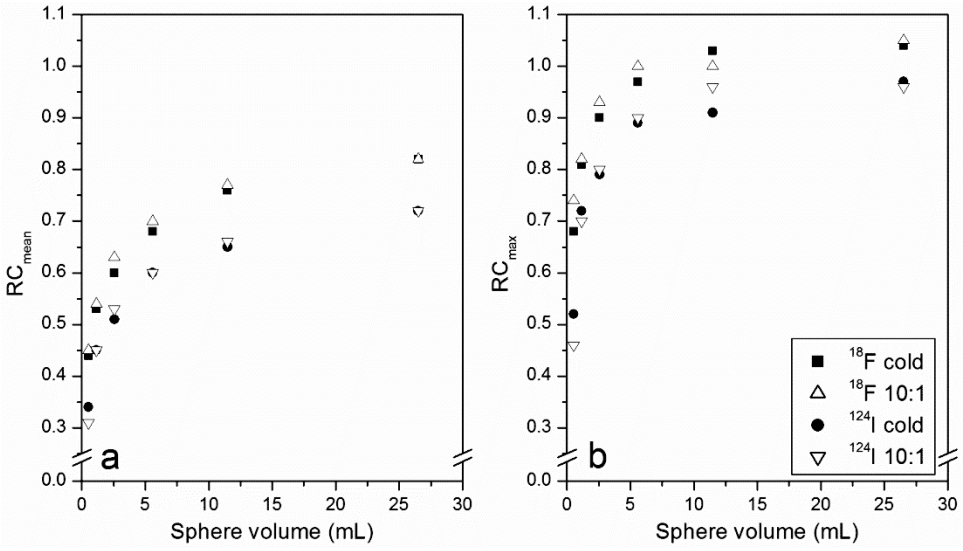

FIGURE 5.2. The accuracy of PET quantification for the soft-tissue phantom is investigated for both ^{18}F and ^{124}I by measuring the RC_{mean} (a) and RC_{max} (b) as function of the sphere volume with and without background radioactivity.

Effect of MR-based attenuation correction of bone lesions

Figure 5.3 presents the percentage deviation in mean ^{124}I radioactivity concentration of the bone lesion images using the 3- or 4-segment MR-based μ-map relative to the CT-based μ-map as a function of sphere diameter. The ^{18}F reconstructed images showed highly comparable results (supplemental material). Attenuation correction performed on the standard 4-segment (without bone) MR-based μ-map resulted in an underestimation up to 15% of the mean radioactivity concentration, due to the too low linear attenuation coefficient assigned to the bone lesion simulating spheres. This underestimation increased with increasing density and sphere diameter. In contrast, the 3-segment (with bone) MR-based μ-map yielded an overestimation up to 10% indicating that a too high linear attenuation correction is assigned to the spheres. This overestimation increased with decreasing density and increasing sphere diameter.

PET spatial resolution measurement

The effective spatial resolutions of ^{18}F and ^{124}I were 4.3 ± 0.5 mm and 5.0 ± 0.3 mm. Compared to ^{18}F, the spatial resolution of ^{124}I was degraded as a result of the high-energy positrons of ^{124}I. The spatial resolution data for each direction are presented in Table 5.1.

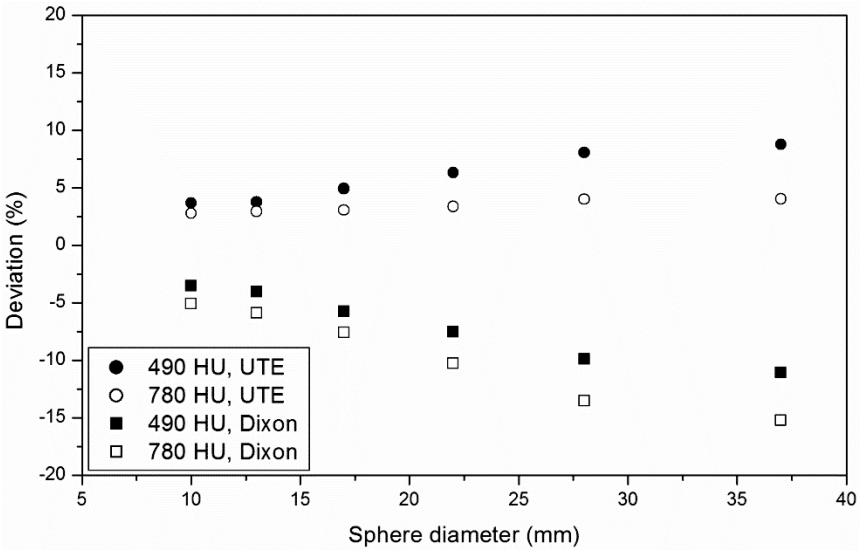

FIGURE 5.3. The effect of MR-based attenuation correction of bone simulating tissue is determined from the percentage deviation in measured mean ^{124}I radioactivity concentration using the 3 (UTE) or 4 (3D Dixon-vibe) segment MR-based μ-map with respect to the original CT-based μ-map as function of the sphere diameter.

TABLE 5.1. Spatial resolution measurement results.

Distance to CFOV (cm)	FWHM ^{18}F (mm)	FWHM ^{124}I (mm)
Tangential spatial resolution		
1	3.57	4.24
10	4.16	4.62
20	4.40	4.85
Radial spatial resolution		
1	3.70	4.36
10	4.25	4.91
20	6.46	6.23
Axial spatial resolution		
1	3.99	5.18
9	3.87	5.21
Effective spatial resolution		
-	4.3 ± 0.5	5.0 ± 0.3

Lesion volume and radioactivity concentration assessment

Figure 5.4 shows the results of the lesion segmentation. For the ^{124}I phantom measurements, the errors in segmented lesion volume and partial volume corrected lesion activity concentration were less than 15% and 25%, respectively. Except for the smallest sphere, all segmented volumes were smaller for the measurements with than without background radioactivity.

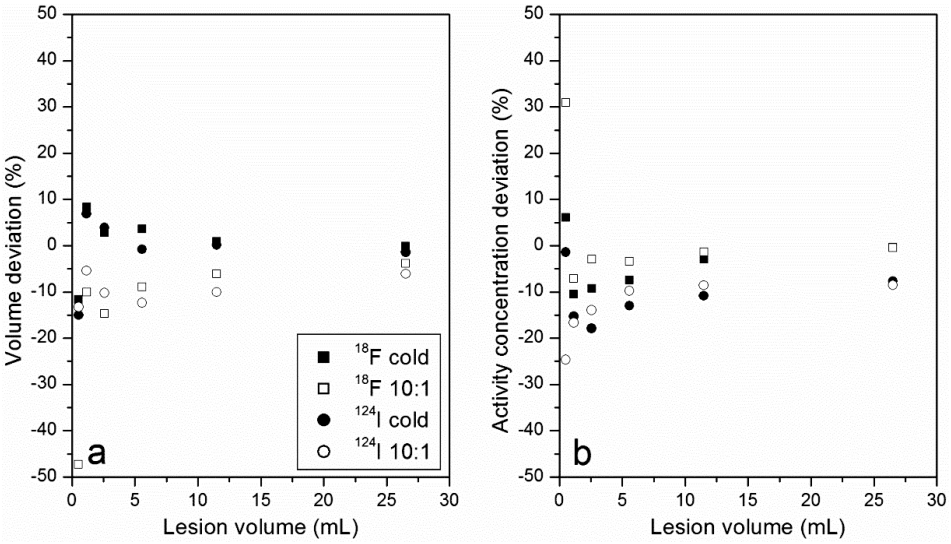

FIGURE 5.4. The accuracy of the used segmentation algorithm for the soft-tissue phantom is assessed from the percentage deviation in segmented lesion volume (a) and mean radioactivity concentration (b) as a function of sphere volume for both ^{18}F and ^{124}I with and without background radioactivity.

Clinical ^{124}I PET/MRI lesion quantification compared to PET/CT

Twenty lesions (6 lymph nodes, 10 thyroid remnants and 4 bone metastases) were identified both on PET/MRI and PET/CT images. Two lesions (lymph nodes) showing very low ^{124}I uptake could only be identified on PET/MRI. As the PET/MRI acquisition was restricted to the head-neck region, one distant bone metastasis present in the lumbar spine region was only visualized in the whole body PET/CT images. In Figure 5.5 fused ^{124}I PET/CT and PET/MRI images of one patient are presented. In Figure 5.6 the Bland-Altman plots comparing the segmented lesion volume and average radioactivity concentration measured with PET/CT and PET/MRI are shown.

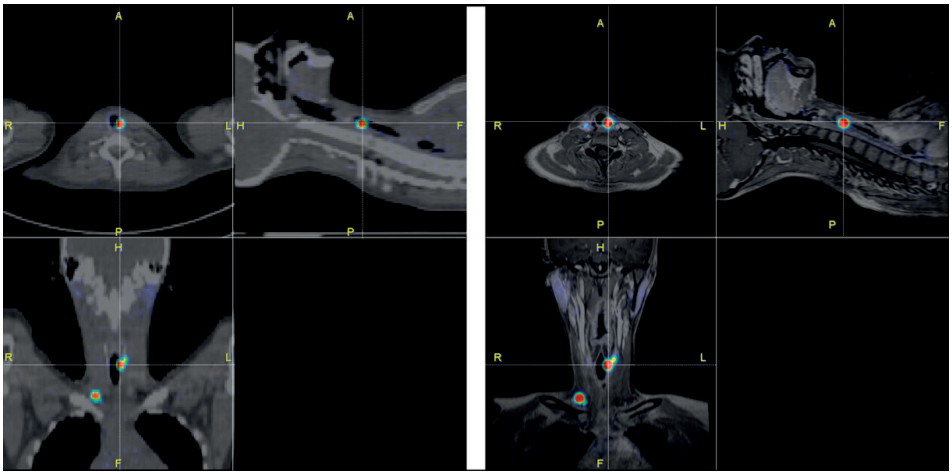

FIGURE 5.5. Visual depiction of clinical ^{124}I PET/CT (left) and PET/MRI (right) images of the same patient showing iodine-avid lesions which could not be identified on CT or MRI images alone.

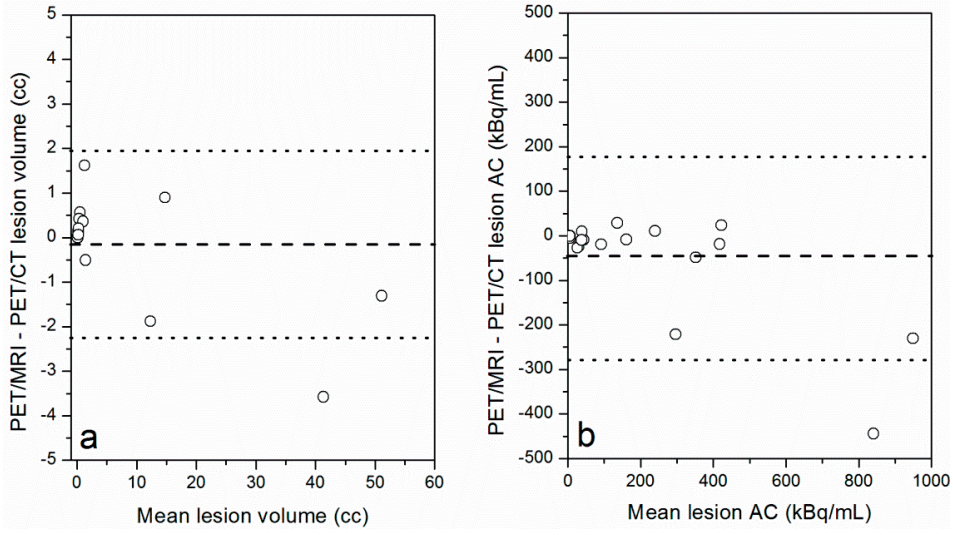

FIGURE 5.6. Comparison of ^{124}I PET/MRI lesion segmented volume (a) and average activity concentration (AC) (b) compared to ^{124}I PET/CT in a clinical setting using Bland-Altman analysis. The dashed line represents the mean activity concentration difference between PET/MRI and PET/CT. The dotted lines represent the 95% confidence interval. Due to overlap of the symbols, less than the twenty analysed lesions are distinguishable.

The ICC values revealed an excellent agreement between PET/MRI and PET/CT quantification for both lesion volume (0.999; 95%-confidence interval: [0.999 – 1.00]) and average radioactivity concentration (0.95; 95%-confidence interval [0.87 – 0.98]). However, percentage deviations larger than 25% in segmented lesion volume (radioactivity con-

centration) were observed for about 50% (25%) of the lesions, in particular for the small lesions (detailed information in supplemental material).

Discussion

To perform reliable ^{124}I PET/MRI lesion dosimetry in DTC patients, accurate assessment of lesion uptake at different time points and lesion volume is required. In previous studies, a systematic underestimation of approximately 10% in measured ^{124}I radioactivity concentration has been reported compared to ^{18}F [4, 15, 18]. This underestimation has in literature been ascribed to overestimation of the conventionally applied scatter correction algorithms resulting in an oversubtraction in the central part of the image [19]. To overcome this problem, a prompt-gamma correction method for ^{124}I, using a scaled random estimate matching the tails of the prompt sinogram [13], is by default implemented on the Siemens Biograph mMR and Biograph mCT systems. However, for both the calibration factor and soft-tissue sphere RC measurements, we still observe an underestimation of 10-12% in measured radioactivity concentration compared to ^{18}F. Although Preylowski et al. [20] showed that implementation of the prompt-gamma correction method did not result in a notable increase in ^{124}I RC values for the Biograph mCT system, they reported similar RC values for ^{124}I and ^{18}F, in contrast to our results. This discrepancy cannot be completely resolved, but is most likely related to an imprecise ^{124}I calibration factor of the dose calibrator [4, 15, 21].

For high resolution MR imaging of the head-neck region, the use of dedicated head-neck and RF surface coils is essential in clinical practice. Such coils cause attenuation of the PET signal, resulting in significant underestimation of the measured radioactivity concentration up to 19% [10, 22]. For rigid, stationary coils, such as the head-neck coil, a CT-based μ-map of the coil is automatically integrated in the PET image reconstruction algorithm upon connection and placement of the coil on the PET/MRI system. Although for flexible surface coils various techniques for attenuation correction have been proposed [22, 23], all Biograph mMR surface coils, including the small and flexible 4-channel RF coil used in this study, are optimized for PET-transparency by stripping the coils from as much of its PET attenuating materials as possible. Our results show that the effect of both investigated RF coils on the PET quantification was locally smaller than 5% for both ^{18}F and ^{124}I.

The classification of bone as soft-tissue in the standard 4-segment μ-map resulted in an increasing underestimation of the measured radioactivity concentration up to 15% with increasing sphere density and diameter, in agreement with values reported in literature [8, 24]. In contrast, for the UTE 3-segment μ-map, in which bone is assigned a fixed linear attenuation coefficient of 0.151 cm^{-1}, an increasing overestimation up to 10% was found. A similar overestimation of bone using UTE-based μ-maps has also been reported in literature [25, 26]. Recently, a novel MR-based attenuation correction

technique using bone mask pairs for major bones has shown to improve PET/MR quantification in bone [24, 27]. Although the quantification differences for bone-tissues are relatively small compared to other uncertainties in the dosimetry calculations (for instance, uncertainties in dose calibrator measurements, kinetic model used to estimate residence time, segmented lesion volume and mean radioactivity concentration), the effect of MR-based attenuation correction on ^{124}I lesion dosimetry of bone lesions requires further investigation.

The used lesion segmentation technique requires the PET spatial resolution to account for regional spill-out and spill-in effects. Therefore, the effective PET spatial image resolution was assessed using line sources in water for both ^{18}F and ^{124}I. The spatial resolution of ^{124}I (5.0 mm) was 0.7 mm degraded compared to ^{18}F (4.3 mm) as a result of the high-energy positrons emitted by ^{124}I, in good agreement with reported ^{124}I PET/CT spatial resolution measurements [4, 18, 20]. In contrast, using point sources in air, Soderlund et al. [12] reported equal ^{124}I and ^{18}F PET spatial resolution values for the Biograph mMR. This discrepancy is explained by the difference in positron range in measurement setup between a point source in water and air, shown by Kemerink et al. [28].

In the presence of background radioactivity, smaller lesion volumes were segmented than without background radioactivity for both ^{124}I and ^{18}F. This is explained by the effect of the cold lesion walls which has been shown to result in a wall-related reduction of the optimum threshold value with increasing background [29]. As a result of this effect, the applied segmentation threshold value is overestimated leading to an underestimation of lesion volume, in agreement with our observations. Despite this effect, the error in segmented lesion volume was less than 15% for ^{124}I. For ^{18}F a relatively large underestimation of 47% in segmented lesion volume was shown for the smallest sphere that is probably caused by a combination of voxel discretization and the cold-wall effect. As this effect depends on the ratio of the thickness of the cold wall to the spatial resolution, this effect is more pronounced for ^{18}F than ^{124}I. Although the used segmentation method used the average lesion activity concentration assuming a spherically shaped lesion with a homogeneous radioactivity concentration, accurate lesion segmentation was shown in clinical scenarios [17].

For the ^{124}I and ^{18}F phantom measurements, the errors in partial volume corrected lesion activity concentration were less than 25%, with the exception of the smallest sphere for ^{18}F. Moreover, for ^{124}I the mean radioactivity concentration was systematically lower compared to ^{18}F, in agreement with the measured calibration factor and soft-tissue sphere RC. After correction for this effect, by dividing the measured radioactivity concentration by the calibration factor, the errors in the partial volume corrected lesion activity concentration were less than 15%. These errors are relatively small compared to other uncertainties in the dosimetry calculations mentioned previously.

Despite an excellent agreement in ^{124}I PET/MRI and PET/CT segmented lesion volume and radioactivity concentration according to the high ICC values (0.999 and 0.95,

respectively), relatively large deviations were observed for some lesions as shown in Figure 5.6. This was caused by the low counting statistics of the PET/CT images, in particular for small lesions and lesions with low radioactivity concentration, and its noise was further enhanced by the 2 mm voxel size to avoid the volume discretization effect. Moreover, the differences in the PET emission times between PET/MRI and PET/CT was a limitation in the direct comparison of ^{124}I lesion quantification of the different modalities. This is reflected in two lymph nodes showing very low ^{124}I uptake. They could only be identified on the PET/MRI images as a result of the long emission time of the PET/MRI acquisition, indicating that an emission time of only two minutes used in whole body PET/CT imaging may not be sufficient for identifying small lesions showing low ^{124}I uptake. However, the PET emission times used reflected the clinical practice. Specifically, in PET/CT, whole body PET examinations are generally performed (with arms up) using an emission time per bed of only a few minutes, whereas, in PET/MRI, single bed positions of the head-neck region are typically performed (with arms down) as a result of the long acquisition times of the various MRI sequences used. As the PET acquisition can be performed simultaneously with MRI, the clinical PET acquisition time is matched to the time of the MRI examination to achieve the best PET image quality. Therefore, the quantitative comparison presented in this study provides a realistic representation of the use of ^{124}I PET/MRI in clinical routine for DTC.

Another shortcoming of this study was the small amount of included patients and analysed lesions. Due to the absence of bone lesions in DTC patients, four ^{124}I-MIBG positive bone lesions were analysed to study the effect of PET/MRI quantification for bone lesions. As the volume and radioactivity concentration of these lesions correspond to the values typically encountered in bone lesions in DTC patients, the comparison is considered to be representative for DTC patients.

Conclusion

For the rigid head-neck RF coil, no decrease in radioactivity concentration resulting from coil attenuation was observed. Near the RF surface coil a small underestimation of less than 5% in radioactivity concentration was observed as a result of RF coil attenuation. For bone simulating lesions, MR-based attenuation correction using the 4-segment μ-map resulted in an underestimation of the mean radioactivity concentration up to 15%, whereas the use to the 3-segment μ-map showed an overestimation up to 10%. In a clinical setting, an excellent agreement between PET/MRI and PET/CT segmented lesion volume and mean ^{124}I radioactivity concentration was observed. Therefore, we conclude that accurate quantitative ^{124}I PET/MR imaging with the aim of performing radioiodine pre-therapeutic lesion dosimetry in DTC is feasible.

References

1. American Thyroid Association (ATA) Guidelines Taskforce on Thyroid Nodules and Differentiated Thyroid Cancer, Cooper, D.S., et al., *Revised American Thyroid Association management guidelines for patients with thyroid nodules and differentiated thyroid cancer*. Thyroid, 2009. **19**(11): p. 1167-214..
2. Jentzen, W., et al., *Assessment of lesion response in the initial radioiodine treatment of differentiated thyroid cancer using 124I PET imaging.* J Nucl Med, 2014. **55**(11): p. 1759-65.
3. Sgouros, G., et al., *Patient-specific dosimetry for 131I thyroid cancer therapy using 124I PET and 3-dimensional-internal dosimetry (3D-ID) software.* J Nucl Med, 2004. **45**(8): p. 1366-72.
4. Jentzen, W., et al., *Iodine-124 PET dosimetry in differentiated thyroid cancer: recovery coefficient in 2D and 3D modes for PET(/CT) systems.* Eur J Nucl Med Mol Imaging, 2008. **35**(3): p. 611-23.
5. Freudenberg, L.S., et al., *124I-PET dosimetry in advanced differentiated thyroid cancer: therapeutic impact.* Nuklearmedizin, 2007. **46**(4): p. 121-8.
6. Wierts, R., et al., *Dose-Response Relationship in Differentiated Thyroid Cancer Patients Undergoing Radioiodine Treatment Assessed by Means of 124I PET/CT.* J Nucl Med, 2016. **57**(7): p. 1027-32.
7. Nagarajah, J., et al., *Diagnosis and dosimetry in differentiated thyroid carcinoma using 124I PET: comparison of PET/MRI vs PET/CT of the neck.* Eur J Nucl Med Mol Imaging, 2011. **38**(10): p. 1862-8.
8. Aznar, M.C., et al., *Whole-body PET/MRI: the effect of bone attenuation during MR-based attenuation correction in oncology imaging.* Eur J Radiol, 2014. **83**(7): p. 1177-1183.
9. Schulz, V., et al., *Automatic, three-segment, MR-based attenuation correction for whole-body PET/MR data.* Eur J Nucl Med Mol Imaging, 2011. **38**(1): p. 138-52.
10. Delso, G., et al., *Evaluation of the attenuation properties of MR equipment for its use in a whole-body PET/MR scanner.* Phys Med Biol, 2010. **55**(15): p. 4361-74.
11. Jentzen, W., L. Freudenberg, and A. Bockisch, *Quantitative imaging of (124)I with PET/ CT in pretherapy lesion dosimetry. Effects impairing image quantification and their corrections.* Q J Nucl Med Mol Imaging, 2011. **55**(1): p. 21-43.
12. Soderlund, A.T., et al., *Beyond 18F-FDG: Characterization of PET/CT and PET/MR Scanners for a Comprehensive Set of Positron Emitters of Growing Application--18F, 11C, 89Zr, 124I, 68Ga, and 90Y.* J Nucl Med, 2015. **56**(8): p. 1285-91.
13. Hayden, C.J., M. Casey, and C. Watson, *Prompt gamma correction for non-standard isotopes in a PET scanner.* US Patent 7,897,652, 2011.
14. Ziegler, S., et al., *NEMA image quality phantom measurements and attenuation correction in integrated PET/MR hybrid imaging.* EJNMMI Phys, 2015. **2**(1): p. 18.
15. Jentzen, W., *Experimental investigation of factors affecting the absolute recovery coefficients in iodine-124 PET lesion imaging.* Phys Med Biol, 2010. **55**(8): p. 2365-98.
16. Boellaard, R., et al., *FDG PET and PET/CT: EANM procedure guidelines for tumour PET imaging: version 1.0.* Eur J Nucl Med Mol Imaging, 2010. **37**(1): p. 181-200.
17. Jentzen, W., *An improved iterative thresholding method to delineate PET volumes using the delineation-averaged signal instead of the enclosed maximum signal.* J Nucl Med Technol, 2015. **43**(1): p. 28-35.
18. Gregory, R.A., et al., *Optimization and assessment of quantitative 124I imaging on a Philips Gemini dual GS PET/CT system.* Eur J Nucl Med Mol Imaging, 2009. **36**(7): p. 1037-48.
19. Conti, M. and L. Eriksson, *Physics of pure and non-pure positron emitters for PET: a review and a discussion.* EJNMMI Phys, 2016. **3**(1): p. 8.
20. Preylowski, V., et al., *Is the image quality of I-124-PET impaired by an automatic correction of prompt gammas?* PLoS One, 2013. **8**(8): p. e71729.
21. Beattie, B.J., et al., *A recommendation for revised dose calibrator measurement procedures for 89Zr and 124I.* PLoS One, 2014. **9**(9): p. e106868.
22. Eldib, M., et al., *Markerless attenuation correction for carotid MRI surface receiver coils in combined PET/MR imaging.* Phys Med Biol, 2015. **60**(12): p. 4705-17.

23. Paulus, D.H., et al., *Simultaneous PET/MR imaging: MR-based attenuation correction of local radiofrequency surface coils.* Med Phys, 2012. **39**(7): p. 4306-15.
24. Paulus, D.H., et al., *Whole-Body PET/MR Imaging: Quantitative Evaluation of a Novel Model-Based MR Attenuation Correction Method Including Bone.* J Nucl Med, 2015. **56**(7): p. 1061-6.
25. Berker, Y., et al., *MRI-based attenuation correction for hybrid PET/MRI systems: a 4-class tissue segmentation technique using a combined ultrashort-echo-time/Dixon MRI sequence.* J Nucl Med, 2012. **53**(5): p. 796-804.
26. Aasheim, L.B., et al., *PET/MR brain imaging: evaluation of clinical UTE-based attenuation correction.* Eur J Nucl Med Mol Imaging, 2015. **42**(9): p. 1439-46.
27. Koesters, T., et al., *Dixon Sequence with Superimposed Model-Based Bone Compartment Provides Highly Accurate PET/MR Attenuation Correction of the Brain.* J Nucl Med, 2016. **57**(6): p. 918-24.
28. Kemerink, G.J., et al., *Effect of the positron range of 18F, 68Ga and 124I on PET/CT in lung-equivalent materials.* Eur J Nucl Med Mol Imaging, 2011. **38**(5): p. 940-8.
29. Hofheinz, F., et al., *Effects of cold sphere walls in PET phantom measurements on the volume reproducing threshold.* Phys Med Biol, 2010. **55**(4): p. 1099-113.

Supplemental materials

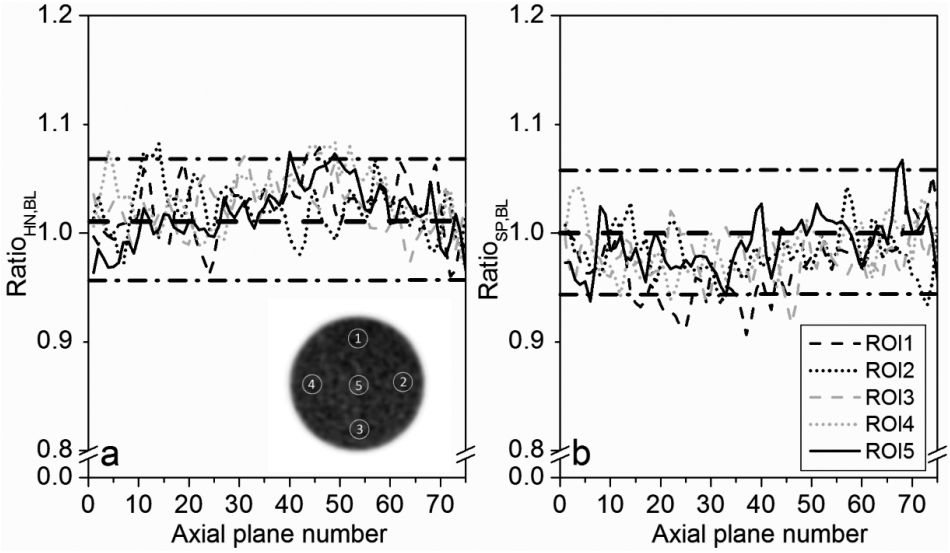

FIGURE S5.1. The influence of RF coil attenuation of the PET signal is assessed using the ratio of the mean ^{18}F radioactivity concentration with RF coil (a: Head-neck coil, b special purpose coil located between plane number 20 and 45) compared to the reference measurement without RF coil measured for all five ROIs shown in the insert of figure a. The horizontal dashed and dash-dotted lines represent the average ratio and 95% uncertainty interval of the radioactivity concentration ratio per plane respectively.

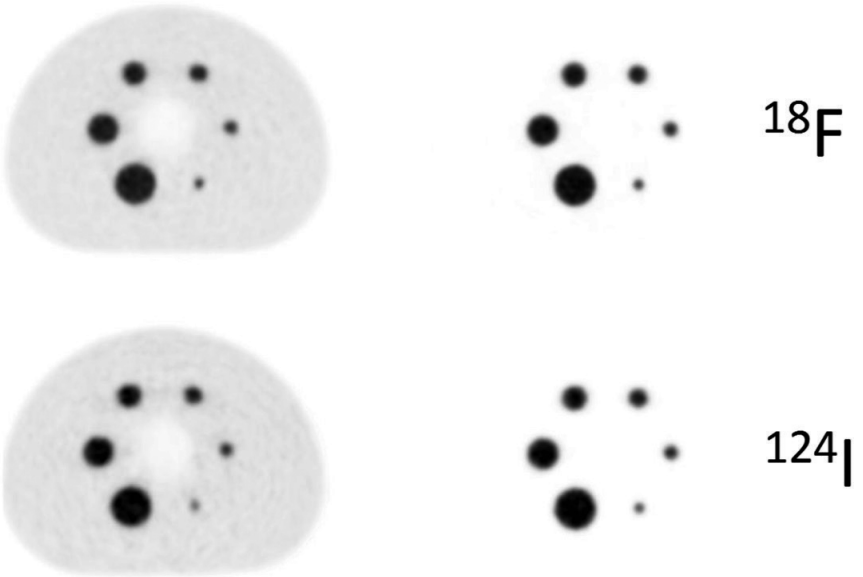

FIGURE S5.2. Reconstructed PET images of the centre slice of the soft-tissue phantom for ^{18}F (top) and ^{124}I (bottom) both with (left) and without (right) background radioactivity.

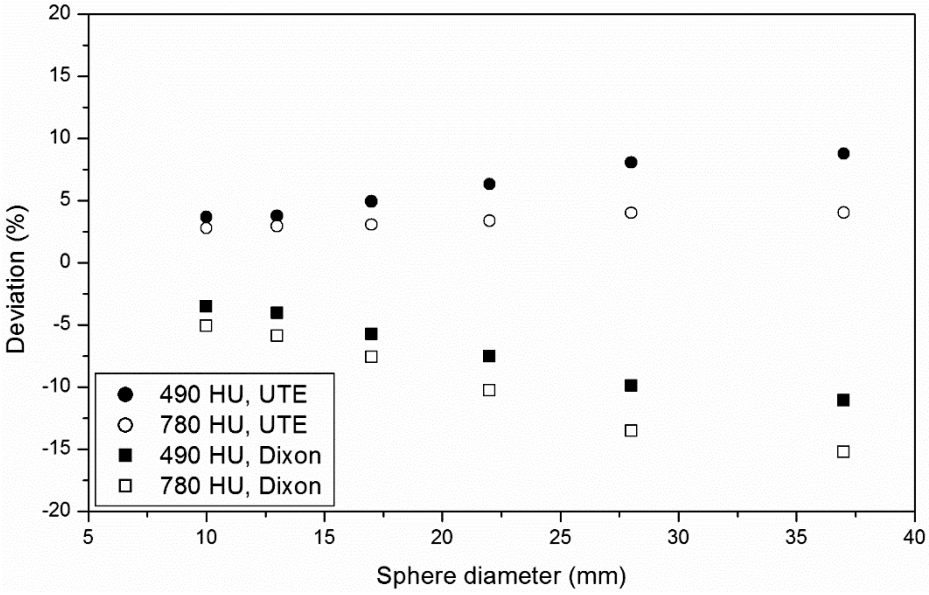

FIGURE S5.3. The effect of MR-based attenuation correction of bone simulating tissue is determined from the percentage deviation in measured mean ^{18}F radioactivity concentration using the 3 (UTE) or 4 (3D Dixon-vibe) segment MR-based μ-map with respect to the original CT-based μ-map as function of the sphere diameter.

TABLE S5.1. Detailed lesion information of patient data. For all lesions, the segmented lesion volume and activity concentration (AC), corrected for partial volume effect (PVE) are presented. In addition, the maximum and average AC (not corrected for PVE) of a spherical volume having a diameter equal to the PET spatial resolution centred at the maximum AC are shown.

			Lesion volume (cc)		Average AC (kBq/mL) PVE corrected		Maximum AC (kBq/mL) not PVE corrected		Resolution AC (kBq/mL) not PVE corrected	
Patient number	Lesion number	Lesion type	PET/CT	PET/MRI	PET/CT	PET/MRI	PET/CT	PET/MRI	PET/CT	PET/MRI
1	1	Lymph node	0.13	0.13	101.7	82.3	40.3	26.6	22.1	17.9
	2	Remnant	0.13	0.13	410.3	434.2	145.5	139.8	89.2	94.4
	3	Remnant	0.13	0.13	47.8	38.6	18.4	12.5	10.4	8.4
	4	Lymph node	0.13	0.13	375.8	327.5	139.6	105.4	81.7	71.2
2	1	Lymph node	0.13	0.28	1063	618.2	323	323	231	241.8
	2	Remnant	0.13	0.13	426.9	408.5	138.9	131	92.8	93.6
	3	Remnant	0.13	0.15	1064	834	327.5	294.5	231.4	216.4
	4	Remnant	0.22	0.79	41.5	17.2	17.8	16	10.1	11.9
3	1	Lymph node	0.13	0.553	40.0	12.8	16.5	9.7	8.7	7.7
	2	Remnant	1.68	1.17	33.9	43.4	55.8	52.2	36.4	40
	3	Lymph node	0.85	1.21	42.9	33.5	50.5	38.8	33.7	30.7
4	1	Remnant	0.13	0.34	407	186.1	130.6	109	88.5	81.9
	2	Remnant	0.135	0.13	234.6	245.2	75.3	76.9	49	53.3
	3	Remnant	0.13	0.13	121.4	150	40.5	46.5	26.4	32.6
	4	Remnant	0.19	0.25	164.8	156.4	69.3	73.5	46.5	54
5	1	Lymph node	0.44	2.06	8.9	3.6	6.9	5.7	3.8	4.3
6	1	Bone metastasis (upper arm)	13.26	11.38	5.0	4.8	9.91	9.08	7.31	7.28
	2	Bone metastasis (pelvis)	43.12	39.54	5.8	5.9	17.28	14.68	10.02	8.92
	3	Bone metastasis (pelvis)	51.76	50.45	4.0	3.8	11.76	8.58	8.35	6.19
	4	Bone metastasis (upper arm)	14.32	15.22	5.8	5.0	11.56	8.36	8.13	6.74

Chapter 6

Monte Carlo simulations of ceiling scatter in nuclear medicine: ^{99m}Tc, ^{131}I and ^{18}F

R.S. Schnerr, A.N. De Jong, G. Landry, C.R.L.P.N. Jeukens, R. Wierts

Med Phys. 2017 Mar;44(3): 1113-1119. Doi: 10.1002/mp.12113

Abstract

Purpose

In the design of nuclear medicine treatment and examination rooms, an important consideration is the shielding required for ionizing radiation from the radioactive isotopes used. The shielding in the walls is normally limited to a height lower than the actual ceiling height. The direct radiation, possible with buildup correction, can be calculated relatively easily. However, little data is available to estimate the dose contribution from ionizing radiation traveling over the wall shielding and scattering off the ceiling. We aim to determine the contribution of the ceiling scatter to the radiation dose outside nuclear medicine rooms.

Methods

Monte Carlo simulations were performed using Gate for different heights of lead shielding in the wall, and different ceiling heights. A point source in air of ^{99m}Tc (141 keV), ^{131}I (365 keV) or ^{18}F (511 keV) was placed 1.0 m above the floor, 3.0 m from the lead shielding. Simulations of ceiling scatter only and for the total radiation dose were performed for these 3 isotopes, 5 different ceiling heights and 4-8 different wall shielding heights, resulting in a total of 165 simulations. This allowed us to compare the contribution of the radiation passing through the shielding and the ceiling scatter.

Results

We find that the shielding required for the primary radiation, measured in half-value layers, is an important factor in determining the relative contribution of ceiling scatter. When more than about 4 half-value layers of shielding are used, ceiling scatter becomes the dominant factor and should be taken into account in the shielding design. In many practical cases for low energy photons (e.g. from ^{99m}Tc; 141 keV; half-value layer of 0.26 mm lead), 2 mm of lead is used and ceiling scatter is a dominant factor contributing >~70% of the dose outside the shielded room. For higher energies (e.g. ^{18}F; 511 keV; half-value layer of 3.9 mm lead) the ceiling scatter is typically less than about 15% when 8 mm of lead shielding is used.

Conclusions

We have performed simulations that allow an estimation of the contribution of ceiling scatter to the radiation dose outside a room, based on the ceiling height, shielding height and isotope used. This will allow for improved shielding designs in nuclear medicine departments.

Introduction

In nuclear medicine departments radioactive isotopes are regularly used for diagnostic and therapeutic treatment purposes. Therefore, it is important to assess the risk of exposure to the associated ionizing radiation, not only for the patients themselves, but also for other patients, visitors and staff members. To protect people outside treatment rooms, it is often necessary to place additional shielding material in the walls. In addition, sensitive measuring equipment such as gamma cameras may require shielding from radiation sources outside the room for optimal performance. Although it is rather expensive, lead shielding is commonly used for this purpose. It is therefore important to carefully assess the placement of shielding to achieve an optimal design that is safe, cost effective, and in line with the applicable legislation.

The attenuation coefficients for γ-radiation of the materials used for radiation protection purposes in practice are readily available [1, 2]. However, calculations based solely on linear attenuation coefficients generally underestimate the radiation levels behind shielding barriers, because they assume narrow beam geometry. Buildup factors to account for the contribution of radiation scattered in the shielding barrier are becoming readily available for the materials and photon energies required [1, 3]. However, even when using a broad beam geometry, this does not take into account that shielding is often applied up to a certain height; typically 2.0-2.5 meters.

For X-ray applications limited data is available on the contribution of radiation that travels over the protective barrier and scatters from the ceiling [4-6]. Recently Martin et al. [5] provided estimates of the ceiling scatter contribution for typical diagnostic X-ray facilities, by summing the contribution of experimentally determined scatter fractions. They concluded that it is important to take ceiling scatter into account for the shielding of e.g., CT scanners. However, such data is not readily available for the γ-radiation commonly encountered in nuclear medicine. To our knowledge, only one study is available involving ceiling scatter of γ-radiation. This study focused on several specific shielding scenarios for a PET/CT room [7]. γ-Radiation differs in some aspects from the radiation generated in X-ray tubes used for diagnostic X-ray imaging. Typically, it has a higher photon energy and a discrete energy spectrum, whereas X-ray tubes emit photons in a broad continuous range of energies. Also, X-ray tubes have a collimated beam that is scattered by the patient, whereas in nuclear medicine the source (the patient) emits ionizing radiation in all directions. Although the basic shielding physics is the same, these considerations make shielding of nuclear medicine rooms different from the shielding of radiology rooms.

This paper aims to facilitate the assessment of the contribution of the ceiling scatter to the radiation dose in nuclear medicine applications. This will allow for improved shielding designs of nuclear medicine rooms. For this purpose we performed Monte Carlo simulations for three isotopes that are commonly used in nuclear medicine: ^{99m}Tc (conventional nuclear medicine), ^{131}I (radionuclide therapy) and ^{18}F (PET imaging); see

Table 6.1. Only the photons with the highest yield and sufficient penetration depth to be relevant in the context of shielding calculations were included in the analysis. These photons cover a wide range in energies: from 141 keV (^{99m}Tc) to 365 keV (^{131}I) and 511 keV (^{18}F). Therefore, our results can be translated to isotopes emitting photons with other energies, and will be useful for almost all isotopes commonly used in nuclear medicine.

Materials and Methods

Setup of the simulations

We used the Gate Monte Carlo toolkit v7.0 [8], which is based on Geant4 v9.6.3 [9, 10] to simulate trajectories of photons emitted by the radioactive isotopes ^{99m}Tc, ^{131}I and ^{18}F. For the electromagnetic physics we used the Penelope models. The Penelope low energy physics models of the Geant4 version used in this work (v9.6.p03), make use of the photon interaction cross sections of the Lawrence Livermore National Laboratory's Evaluated Photon Data Library [11]. This dedicated low energy physics model was preferred to the standard EM models, since the latter are parameterized instead of relying on evaluated data libraries.

TABLE 6.1. Properties of the three radioactive isotopes and the photons emitted with a yield > 0.03. For each isotope the highest yield photon energy was included in the simulations to simplify the interpretation of the results (bold rows). Data were taken from the NuDat database [12] (half-life and yield) and the NIST XCOM database [2] (half-value layer narrow beam). Buildup factors for the broad beam transmission were taken from Shimizu et al. [3].

Isotope	half-life	photons yield > 0.03		half-value layer ($d_{0.5}$)	
	(h)	energy (keV)	Yield ($Bq^{-1}\ s^{-1}$)	narrow beam (mm Pb)	broad beam (mm Pb)
^{99m}Tc	6.006	18.4	0.04	0.01	
		141	**0.89**	**0.26**	**0.42**
^{131}I	192.5	284	0.061	1.35	
		365	**0.815**	**2.23**	**2.60**
		637	0.072	5.29	
^{18}F	1.828	**511**	**1.935**	**3.91**	**4.96**

The sources were simulated as point sources free in air, i.e. no self-absorption. The energy and yield of the photons emitted by these isotopes, with a yield > 0.03 are listed in Table 6.1. For each of the isotopes only the photon energy with the highest yield and penetration depth was included in the simulations (bold rows in Table 6.1). Although this neglects the contribution of some low yield photon energies, it allows for the translation of our results to other photon energies without the complexity of multiple photon energies per isotope.

We chose to use a simplified but realistic room design (see Figure 6.1), consisting of a 30 cm thick concrete floor and ceiling in a space that was 6.0 m wide, 14.0 m long and has a maximum ceiling height of 5.0 m. In the middle of the 14.0 m long side the lead shielding barrier was placed, ranging over the entire width of the space and dividing it into two rooms of 7.0 m length. The thickness of the lead barrier was chosen to be 2.0 mm for ^{99m}Tc and 8.0 mm for ^{131}I and ^{18}F, which correspond to realistic values for adequate shielding in clinical practice. The radiation source was placed in the left room at a distance of 3.0 m from the barrier in the middle of the room at a height of 1.0 m above the floor, which is the approximate height of a patient lying on a bed. The ceiling height was varied between 3.0-5.0 m in 0.5 m steps. For each ceiling height, simulations were performed for different barrier heights. These were chosen to be 1.8, 2.2, 2.6, 3.0, 3.5, 4.0, 4.5 and 5.0 m. The maximum height of the barrier used was the ceiling height; i.e. shielding up to the ceiling.

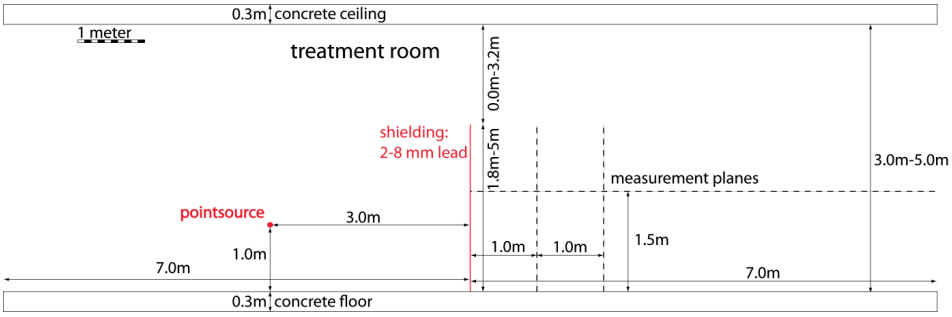

FIGURE 6.1. The room design used in the Monte Carlo simulations. The ceiling height was varied between 3.0 m and 5.0 m and the lead shielding barrier between 1.8-5.0 m. The source was placed 3.0 m from the wall at a height of 1.0 m above the floor. The radiation dose was measured at various measurement planed behind the shielding (dashed lines).

In order to differentiate the contributions of the direct and scattered radiation, we ran the simulations twice for all geometries: once to measure the total radiation dose outside the room, and once to measure only the contribution of the ceiling scatter. The latter was achieved by setting the barrier properties such that it absorbs all incoming radiation. From these two simulations we could assess the contribution of ceiling scatter to the total radiation dose. In total, this resulted in 165 separate simulations: 3 radionuclides, 5 ceiling heights, 4-8 shielding heights and total radiation dose/ceiling scatter only. A fixed number of 40 million photons per simulation was used. This number of photons was chosen after a series of test runs, as it yields sufficient precision (of the order of a few percent in the determined kerma or better) while keeping the computation time reasonable, i.e. around 1 day.

Calculating air kerma from Monte Carlo simulations

To quantify the dose rate behind the protective barrier, we chose to measure the air kerma in vertical and horizontal planes. Air kerma is calculated from the simulations by summing the contribution of all the individual photons *i*:

$$K_{\text{air}} = \sum_i \frac{\mu_{tr}(E_i)E_i}{\rho \cos \alpha_i}, \qquad \text{Eq. 1}$$

where K_{air} is the air kerma (in Gy) and μ_{tr} is the energy transfer coefficient of air (m^{-1}) [13], which depends on the photon energy E_i (J). The density of air is given by ρ (kg/m^3), and α_i is the angle between the photon path and the plane in which the air kerma is calculated. Reported air kerma values are averaged over 1.0 m (horizontal) by 0,5 m (vertical) rectangles.

Broad beam and narrow beam transmission calculations

Narrow beam transmission calculations assume that the photon is lost at every interaction. The contribution of scattered photons is neglected in this approach. In a broad beam approach, buildup factors are used to correct for the contribution of scattered photons. We compared the results of our simulations to both narrow and broad beam transmission calculations. For the broad beam calculations, we used the buildup factors for lead provided by Shimizu et al. [3].

Results

Dependence on ceiling and barrier height

The top row of Figure 6.2 shows the total air kerma at a distance of 1.0 m behind the lead wall, at a height of 1.5 m, for different geometries and three different isotopes. This height was chosen as a typical height of the organs most sensitive to radiation for a person standing at that location. The bottom row shows the ratio of the kerma due to ceiling scatter (scatter air kerma) and the total air kerma. As expected, we found that, for a given ceiling height, the total air kerma behind the barrier decreases as the barrier height is increased. This decrease is the result of a reduction of the ceiling scatter and is more pronounced for lower ceiling heights. For each curve the total air kerma is lowest when shielding is placed all the way up to the ceiling and the air kerma behind the shielding is solely due to transmission of radiation through the shielding.

The contribution of the ceiling scatter also depends strongly on the photon energy. For ^{99m}Tc between 50-100% of the radiation outside the room is due to ceiling scatter; whereas for ^{131}I this is between 5% and 45% and for ^{18}F it is below 20%.

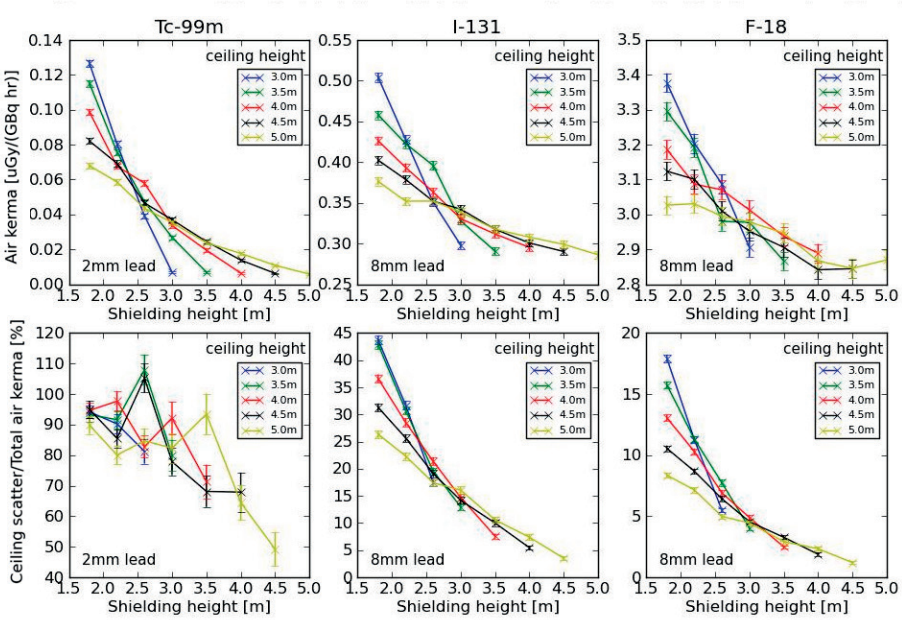

FIGURE 6.2. Total air kerma resulting from an average activity of 1 GBq for 1 hour, measured 1.0 m behind the barrier at a height of 1.5 m, as a function of the barrier height. The different curves per panel show results for different ceiling heights. From left to right we show the results for ^{99m}Tc, ^{131}I and ^{18}F; the top row shows the total air kerma and the bottom row the (ceiling) scatter air kerma contribution as a fraction of the total air kerma.

Dependence on distance to the barrier

We also investigated total air kerma as a function of the distance to the barrier. Figure 6.3 shows the results for a ceiling of 4.0 m. Interestingly, maximum dose levels were not always found directly behind the protective barrier. For ^{99m}Tc, the maximum radiation dose was found about 1-2 m behind the barrier. This decreases slightly for ^{131}I, and for ^{18}F the maximum is directly behind the barrier.

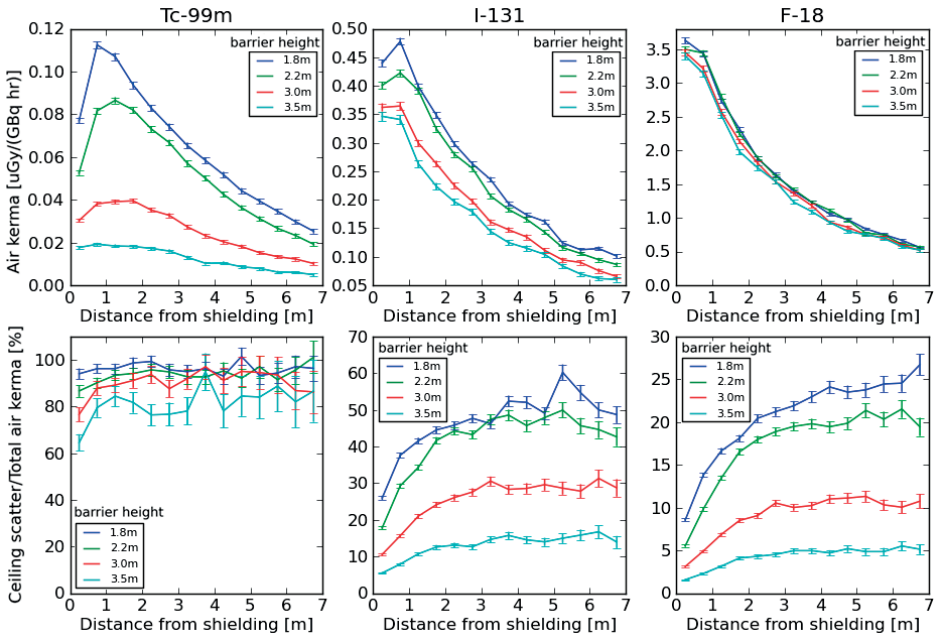

FIGURE 6.3. Total air kerma behind the barrier, at a height of 1.5 m, as a function of the distance to the barrier. The top row shows the total air kerma and the bottom row the ceiling scatter air kerma contribution as a fraction of the total air kerma. Air kerma was averaged over an area of 1.0 m wide and 0.5 m high (1.25-1.75m). Curves are shown for different barrier heights (see legends); the ceiling height was 4.0 m.

Comparison of the simulations to narrow and broad beam calculations

We compared the results of our simulations to narrow and broad beam transmission calculations. To our knowledge, no measurement data are available that could be compared to our simulations. Figure 6.4 shows the effective transmission of the shielding (ratio of air kerma with and without shielding) as a function of the shielding thickness in units of the half value layer, for all three isotopes. Simulations were performed for a typical thickness of the lead shielding (2 mm for ^{99m}Tc and 8.0 mm for ^{131}I and ^{18}F).

The transmission as determined from our simulations, excluding the ceiling scatter, shows good agreement with that of the broad beam transmission calculations. For ^{99m}Tc, the simulations are 31% below the calculations, for ^{131}I and ^{18}F they are 12% and 2.4% higher respectively. The larger deviation for ^{99m}Tc is likely due to the larger uncertainty for this isotope. The lower transmission of the 141 keV photons results in a smaller number of photons detected in the Monte Carlo simulations resulting in a larger uncertainty. Additionally, the relatively large buildup factor for ^{99m}Tc is likely associated with a lower accuracy.

The effective transmission, including ceiling scatter, for different shielding thicknesses can be estimated by adding the ceiling scatter contribution from the simulations

(the difference between the two points) to the broad beam transmission curve. This is a valid approach, as the ceiling scatter is independent of the shielding thickness. This effective transmission is shown by the dotted lines in Figure 6.4.

We find that the difference in the expected transmission between a normal broad beam calculation, and one that includes ceiling scatter can be substantial when the shielding thickness becomes large with respect to the half-value layer. It is also interesting that the curves for the different isotopes are rather similar; for all three isotopes the ceiling scatter contribution reaches 50% of the total radiation dose when about four half-value layers of shielding are used.

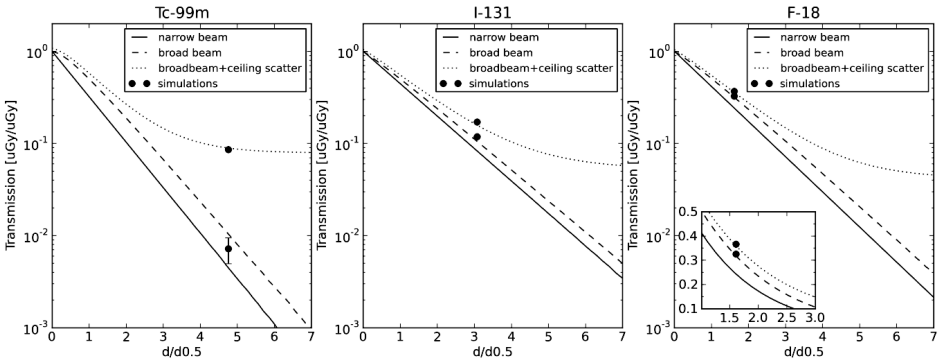

FIGURE 6.4. Comparison of calculated narrow beam transmission (solid line), broad beam transmission (dashed line) and the transmission results of our Monte Carlo simulations plotted as a function of shielding thickness expressed in units of the half-value layer (first half value layer for broad beam transmission, see Table 6.1). Simulation results are for a ceiling height of 3.5 m and a barrier height of 2.2 m (black dots) two points are plotted for each isotope: including ceiling scatter (higher point) and excluding ceiling scatter (lower point). The dotted line shows the broad beam transmission including ceiling scatter as determined from the simulations.

From these results it is clear that there may be many cases in which it is important to take the contribution of ceiling scatter into account. To facilitate the calculation of shielding requirements for new nuclear medicine rooms, we present the air kerma due to ceiling scatter as found in our simulations, with a source at a distance of 3 meters from the wall, in Table 6.2. It should be noted that in our simulations no wall is present above the lead shielding. In practice this will result in a conservative estimate (overestimation) of the ceiling scatter, as a wall will typically offer at least some degree of shielding.

TABLE 6.2. Ceiling scatter air kerma 1 m behind the lead barrier at a height of 1.5 m, for different ceiling heights, barrier heights and for the isotopes ^{99m}Tc, ^{131}I and ^{18}F. Values are in units of [0.1 µGy/(GBq hr)].

	ceiling height [m]														
	^{99m}Tc					^{131}I					^{18}F				
barrier height [m]	3.0	3.5	4.0	4.5	5.0	3.0	3.5	4.0	4.5	5.0	3.0	3.5	4.0	4.5	5.0
1.8	1.2	1.1	0.9	0.8	0.6	2.2	2.0	1.6	1.3	1.0	6.1	5.2	4.2	3.3	2.5
2.2	0.7	0.7	0.7	0.6	0.5	1.4	1.3	1.1	1.0	0.8	3.6	3.6	3.2	2.7	2.2
2.6	0.3	0.5	0.5	0.5	0.4	0.6	0.8	0.8	0.7	0.6	1.7	2.3	2.1	1.9	1.5
3.0	-	0.2	0.3	0.3	0.3	-	0.4	0.5	0.5	0.5	-	1.2	1.5	1.3	1.3
3.5	-	-	0.1	0.2	0.2	-	-	0.2	0.3	0.3	-	-	0.7	1.0	0.9
4.0	-	-	-	0.1	0.1	-	-	-	0.2	0.2	-	-	-	0.5	0.7
4.5	-	-	-	-	0.1	-	-	-	-	0.1	-	-	-	-	0.3
5.0	-	-	-	-	-	-	-	-	-	-	-	-	-	-	-

Discussion

The optimal shielding of a nuclear medicine room depends on many aspects, such as the isotopes and amount of radioactivity used, room dimensions, and the occupancy of neighboring rooms. Typically, stand-alone SPECT and gamma-cameras do not require a lot of radiation shielding. The dose rates of the (diagnostic) amounts of ^{99m}Tc used are typically rather low, except in cases with a high patient throughput, high doses of radioactivity such as encountered in post radionuclide therapy examinations, and/or small examination rooms. However, radioactive sources (such as radioactive patients) outside the scanner room can be problematic when calibrating such a system. In contrast, for PET cameras and radionuclide therapy rooms a substantial amount of shielding is often required, and the amount of lead necessary can be rather costly. Applying shielding close to the ceiling (or above a dropped ceiling) can be especially expensive and cumbersome, as ventilation and plumbing pipes are often located there. It is therefore important to determine, as accurately as possible, how much shielding is necessary and up to which height it is required.

Irrespective of the isotope, we find a clear dependence of the relative importance of ceiling scatter on the room and shielding geometry. This dependence shows a qualitatively similar dependence on ceiling height and barrier height as is seen for X-ray modalities [5]. Higher barriers reduce the radiation dose, as expected, and this effect is more pronounced for lower ceiling heights. This can be expected, as the relative decrease in area of the gap between the ceiling and top of the barrier is larger for lower ceiling heights. For a fixed barrier height, higher ceilings result in lower radiation levels from ceiling scatter. This reduction with height does not simply follow a $1/r^2$ behavior, because the exposed area of the ceiling also increases with increasing ceiling height.

However, there are also important differences compared to X-ray modalities: the range of photon energies is typically much larger, and the photons are mono-energetic. As a result, the differences between low- and high photon-energy applications are much larger. In practice, for high photon-energy applications, such as PET, it is typically more effective to use relatively low and thick shielding, while for lower energy applications relatively thin but higher shielding may be beneficial. This can be understood by our comparison of the results of our simulations to broad beam transmission curves. These show that the relative importance of ceiling scatter strongly depends on the thickness of the applied shielding as measured in units of the half-value layer. In high energy applications, typically only a few half-value layers of shielding are used, while in low energy applications even 2 mm of lead is equivalent to 5 half-value layers or more. Therefore, the radiation traveling through the wall is already effectively shielded and ceiling scatter is the dominant contribution. To determine shielding requirements in a practical situation, an estimate of the relative contribution of ceiling scatter can be made using the data in Figure 6.2 to 6.4. For more detailed calculations the ceiling scatter contribution found in Table 6.2 can be added to the contribution from radiation travelling through the shielding (used in broad beam transmission factors available in the literature), as these two contributions are independent of each other.

Interestingly, we found that, due to the ceiling scatter contribution, the maximum radiation dose might not be found directly behind the shielding barrier. The point of maximum radiation dose can be located more than a meter behind the shielding barrier, depending on the relative contribution of the ceiling scatter. Potentially, a person working behind a desk could be sitting exactly in the dose maximum. Therefore, measuring radiation levels directly behind shielded walls, as typically done to check whether sufficient shielding is present, might not be the most accurate approach in cases with a relatively high contribution of ceiling scatter.

Limitations

In our current simulations we only took the most relevant photon energy into account for each isotope. While this facilitates interpretation of the results, in practice, of course, all photons need to be taken into account. ^{131}I, for instance, emits 637 keV photons with a yield of 7.2% in addition to the 365 keV photons modelled in our simulations. When more than several half-value layers of shielding are used, the contribution of these photons will become dominant and should thus be taken into consideration. In addition, we have modelled the radiation sources as a point source free-in-air. In case patients are the source of radiation, a correction for self-absorption can be performed. Finally, we have placed the source at a distance of 3 meters from the shielding, but in practice this distance will typically vary. For sources located closer to the shielding, the relative contribution of the ceiling scatter will decrease, whereas for sources located further away it will increase [7].

Conclusion

Ceiling scatter can be a dominant factor in the radiation does outside shielded nuclear medicine rooms. The contribution of ceiling scatter, compared to that of ionizing radiation traveling through shielding in the wall, depends mostly on room geometry (ceiling and shielding height) and the thickness of the shielding as measured in units of the half-value layer. When more than about 4-5 half-value layers of shielding are used, ceiling scatter becomes the dominant factor and should be taken into account.

The contribution of ceiling scatter to the radiation dose as determined from our Monte Carlo simulations will facilitate the design of more cost-effective and safe solutions for future nuclear medicine rooms.

Disclosure of conflicts of interest

The authors have no relevant conflicts of interest to disclose.

References

1. Shleien, B., L. Slaback, and B. Birky, *Handbook of Health Physics and Radiological Health*. 3 ed. 1998, Baltimore: Lippincott Williams & Wilkins.
2. Berger, M.J., et al. *NIST XCOM: Photon Cross Sections Database 2*. Available from: www.nist.gov/pml/data/xcom; version 1.5.
3. Shimizu, A., T. Onda, and Y. Sakamoto, *Calculation of gamma-ray buildup factors up to depths of 100 mfp by the method of invariant embedding, (III).* J Nucl Sci Technol, 2004. **41**(4): p. 413-424.
4. McVey, G. and H. Weatherburn, *A study of scatter in diagnostic X-ray rooms.* Br J Radiol, 2004. **77**(913): p. 28-38.
5. Martin, C.J., et al., *Derivation of factors for estimating the scatter of diagnostic x-rays from walls and ceiling slabs.* J Radiol Prot, 2012. **32**(4): p. 373-96.
6. Edwards, S. and D. Schick, *Monte Carlo Modeling of Computed Tomography Ceiling Scatter for Shielding Calculations.* Health Phys, 2016. **110**(4): p. 328-41.
7. Fog, L.S. and J. Cormack, *Mathematical modeling of the radiation dose received from photons passing over and through shielding walls in a PET/CT suite.* Health Phys, 2010. **99**(6): p. 769-79.
8. Jan, S., et al., *GATE V6: a major enhancement of the GATE simulation platform enabling modelling of CT and radiotherapy.* Phys Med Biol, 2011. **56**(4): p. 881-901.
9. Agostinelli, S., et al., *GEANT4-a simulation toolkit.* Nuclear Instruments & Methods in Physics Research Section a-Accelerators Spectrometers Detectors and Associated Equipment, 2003. **506**(3): p. 250-303.
10. Allison, J., et al., *Geant4 developments and applications.* Ieee Transactions on Nuclear Science, 2006. **53**(1): p. 270-278.
11. Cullen, R., J.H. Hubbell, and L. Kissel, *EPDL97: The evaluated photon data library, 97 version.* LLNL Report No. UCRL-50400, 1997. **6**(5).
12. National Nuclear Data Center. *Nudat 2*. Available from: www.nndc.bnl.gov/nudat2; version 2.6.
13. Bos, A.J.J., F.S. Draaisma, and W.J.C. Okx, *Inleiding tot de stralingshygiëne*. 2007, Den Haag: SDU Uitgevers.

Chapter 7

General discussion

Current role of tailored dosimetry in DTC

The overall aim of this thesis was to improve radiation dose assessment in radioiodine treatment in differentiated thyroid cancer (DTC). As described in Chapter 2, advanced tailored dosimetry has been reported feasible in clinical practice and both instrumentation and dosimetric software are still evolving at high pace. For DTC, the concept of performing personalized radioiodine treatment, in which pre-therapeutic blood and/or lesion absorbed dose calculations are considered in the decision-making of the ^{131}I activity to be administered in therapy, is described in the latest guidelines on DTC [1-3]. Although the application of pre-therapeutic lesion absorbed dose assessment has been reported to change patient management in 25%-50% of DTC patients [4, 5], the use of pre-therapeutic dosimetry is not recommended in these guidelines. In clinical practice, empirically determined fixed amounts of radioiodine activity, based on disease characteristics and patient age, are usually still administered. This is explained from a lack of supporting evidence from randomized controlled trials, long standing professional traditions, personal expertise and, last but not least, reimbursement issues [6]. In addition, reliable lesion dosimetry requires accurate quantification of lesion volume and radioiodine uptake at multiple time points which is time consuming, not patient friendly and technically challenging due to the finite spatial resolution and sensitivity of nuclear medicine imaging equipment. Finally, with the current treatment, in which fixed therapeutic amounts of ^{131}I are administered following total thyroidectomy, the prognosis of DTC is in general excellent and 10-year relative survival rates of 0.98 for papillary and 0.92 for follicular disease have been reported [7].

Potential benefits of tailored radioiodine dosimetry

According to the European union council directive 2013 [8] a tailored dosimetry approach is required for all medical radiotherapeutic purposes (including radionuclide therapy) and target volumes should be individually planned, taking into account that doses to non-target volumes and tissues must be as low as reasonably achievable (ALARA). This requirement is supported by the fact that the use of empirically fixed amounts of ^{131}I has been reported to result in the risk of under- or overdosing [2, 9, 10]. Indeed, radioiodine treatment has been shown to result in adverse effects such as salivary gland dysfunction, transient gonadal dysfunction and second primary malignancies and the prevalence and severity of these effects correlate with increasing therapeutic amounts of ^{131}I activity [11]. Recent studies have reported no statistically significant differences in ablation success rate between low (1.1 – 1.85 GBq) and high (3.7 – 5.5 GBq) amounts of administered ^{131}I in low- to intermediate-risk patients [12-15]. Even though long-term data with respect to the chances of local recurrence and the effect of adjuvant therapy are not yet available, post-surgical radioiodine treatment is no longer

routinely indicated for the majority of low- and intermediate-risk DTC patients according to the latest recommendations of the American Thyroid Association (ATA) [1]. This standpoint, however, is debated by the European Association of Nuclear Medicine (EANM) [16] and not endorsed in the Dutch national DTC guidelines in which the use of a low amount of 1.1 GBq ^{131}I activity for remnant ablation in low-risk DTC patients is recommended [17]. At the moment, there is widespread consensus that the use of pre-therapeutic personalized dosimetry for radioiodine treatment is not recommended for low-risk DTC patients and a personalized radioiodine treatment approach only has potential benefit for high-risk patients showing distant metastases [1]. In these patients, radioiodine therapy success is decreased and multiple high-dose (3.7 – 7.4 GBq) radioiodine treatments, are often required [2]. However, in a fixed therapeutic activity approach, the maximum activity that can safely be administered is limited. In fact, it has been demonstrated that in more than 90% of patients much higher activities can be administered, indicating that the majority of high-risk patients are potentially undertreated using a fixed activity approach [18]. Indeed, in a retrospective study described in Chapter 3 we found that lesions that showed complete response to radioiodine therapy received a statistically significant higher lesion absorbed dose compared to the lesions showing no or incomplete response. Using a fixed activity approach, we found a response rate of 69% for metastatic lesions, whereas Jentzen et al. [19] reported a 88% response rate using a ^{124}I PET/CT-based personalized activity approach which resulted in higher administered ^{131}I activities. These findings indicate that a personalized dosimetry approach using ^{124}I PET/CT facilitates lesion dose escalation and may result in improved patient outcome in high-risk DTC patients.

Challenges in tailored radioiodine dosimetry

As described in Chapter 2, the clinical application of performing pre-therapeutic ^{124}I PET dosimetry in DTC faces several challenges and limitations which result in uncertainties in the lesion absorbed dose calculations (inter alia: uncertainties in lesion radioiodine uptake quantification, lesion volume determination, radioiodine residence time and ^{124}I related quantification errors). Despite these uncertainties, we showed in Chapter 3 that the lesion absorbed dose, calculated from pre-therapeutic ^{124}I PET/CT measurements, provided prognostic information with respect to complete lesion response. However, the receiver operator characteristic (ROC) curves presented in Figure 3.2 of Chapter 3 show moderate area under the curve (AUC) values of 0.68 and 0.73 for all remnants and metastases, respectively, which may be increased with improved ^{124}I PET quantitative performance and lesion volumetry, resulting in smaller lesion absorbed dose uncertainties.

Lesion uptake quantification

Accurate quantification of radioiodine uptake is affected by the finite spatial resolution of current nuclear medicine imaging equipment. Even for ^{124}I PET, which is by various groups considered to be the preferred imaging modality for the application of radioiodine dosimetry in DTC [5, 20, 21], the spatial resolution is currently limited to 5-7 mm as shown in Chapter 5. As a consequence, activity recovery is substantially degraded even for relatively large lesion volumes up to 5 cm^3 as shown in the recovery coefficient (RC) curves presented in Chapters 4 & 5, meaning that for smaller lesions sophisticated partial volume correction techniques are required. Moreover, due to the limited spatial resolution relevant small-scale activity inhomogeneities within a tissue will be unknown. In particular, Jentzen et al. [22] reported a discrepancy in the calculated salivary gland absorbed dose, which is considered to be an organ at risk in radioiodine therapy, and clinical observation of glandular side effects which they described to result from a radioiodine distribution on microscopic scale.

In addition, for lesions showing low ^{124}I uptake, lesion quantification can be affected by the low counting statistics of short whole body PET examinations. In Chapter 5 we observed percentage deviations in measured ^{124}I lesion radioactivity concentration larger than 25% for a quarter of all ^{124}I-avid lesions measured with PET/CT and PET/MRI. This was caused by the low counting statistics of the whole body PET/CT images which were acquired for only 2 minutes per bed position. In contrast, for PET/MRI, PET acquisition was restricted to the head-neck region and performed simultaneously with the MRI examinations resulting in long PET acquisition times of 20-30 minutes. These findings indicate that short PET emission times result in substantial uncertainties in calculated lesion absorbed dose.

Lesion volume assessment

Another major challenge in lesion absorbed dose assessment in DTC is the accurate determination of lesion volume which is essential for reliable lesion dosimetry. Due to the limited soft-tissue contrast, the boundary of tumours and thyroid remnants can generally not be segmented clearly on high-resolution anatomical CT or ultrasound images and lesion volumetry based on these imaging modalities is considered unreliable [2]. Therefore, in clinical practice, lesion volume segmentation is commonly performed on PET images. However, the majority of lesions encountered in DTC are very small with respect to the PET spatial resolution. In fact, using a sophisticated iterative lesion volume segmentation method which facilitates accurate volume determination for lesions with a diameter down to the PET spatial resolution and correcting for partial volume effects, we found that lesion volume could only be reliably determined in 40% of all lesions as described in Chapter 3.

Radioiodine residence time

In addition, lesion absorbed dose assessment requires knowledge of the lesion radioiodine uptake as a function of time. The medical internal radiation dose (MIRD) scheme [23], advises to use one or two data points taken at a fraction of the effective radiopharmaceutical half-life T_e, one near T_e and two other data points taken at approximately 3 T_e and 5 T_e, meaning a total of 4-5 data points. For radioiodine therapy in DTC patients, Jentzen et al. demonstrated that the radioiodine residence time, defined as the total number of radioactive disintegrations in the lesion per administered unit activity, can in good approximation be determined from the 24 and 96 hour radioiodine uptake after administration using a single exponential fit through both measurements and assuming linear uptake during the first 8 hours, as shown in Figure 1.3 of Chapter 1 [24]. Although this simplified 24-96 h approach reduces the number of required sample points and therefore facilitates the application of performing pre-therapeutic ^{124}I lesion dosimetry in a clinical setting, deviations up to 38% with respect to the 5 point sample approach for lesions showing a low radioiodine uptake were reported.

^{124}I quantification

Compared to ^{18}F, ^{124}I is not an ideal radionuclide for quantitative PET imaging. First of all, the high amount of low-energy X-rays emitted by ^{124}I are prone to self-absorption within the sample, for instance a syringe or vial. Since this self-absorption depends on sample geometry and dose calibrators are rather sensitive to low-energy X-ray radiation, sample specific dose calibrator settings are essential to perform accurate ^{124}I activity measurements [25]. Moreover, with a positron yield of 22.5%, the count rate sensitivity is over 4 times lower compared to ^{18}F. In addition, due to the high end-point energy of the emitted positrons, the PET spatial resolution in soft-tissue is degraded by 0.5 – 1.0 mm as shown in Table 5.1 of Chapter 5. Furthermore, ^{124}I is not a pure positron emitter and approximately half of the emitted positrons are in cascade with a 603 keV prompt gamma photon resulting in the detection of spurious coincidences termed prompt gamma coincidence (PGC) events. These PGC events are spread all over the PET field of view (FOV) producing higher artificial background levels in the PET sinograms. As current PET scatter correction is performed using a model-based scatter distribution which is scaled to the sinogram tails outside the patient body, the increased background levels lead to an overestimation of the amount of scatter in the central part of the image resulting in an underestimation of the ^{124}I activity concentration as clearly demonstrated in Figure 4.2 of Chapter 4.

Potential of PET developments on ^{124}I lesion dosimetry

PGC correction techniques

In Chapter 4 it was shown in phantom measurements that PGC correction, based on a scaled randoms estimate, substantially reduced the amount of underestimation of the ^{124}I activity concentration present in the background compartment of the phantom. In addition, a systematic increase in sphere RCs were observed ranging from 3-5% for the largest spheres up to 70% for the smallest spheres, indicating the importance of PGC correction. However, even with PGC correction a systematic underestimation in ^{124}I RC values was observed, indicating that the PGC correction method was not perfect. In patient measurements, PGC correction resulted in an increase in measured ^{124}I lesion activity concentration for the majority of lesions at 24h after ^{124}I administration. Although this increase proved to be statistically significant, the mean percentage deviation was less than 3%. More importantly, PGC correction resulted only in a very small increase in calculated lesion dose per administered activity (LDpA) (mean percentage difference 3.1%), and thus lesion absorbed dose, which is considered negligible compared to the other sources of uncertainty in the lesion dosimetry calculations as described previously. Nonetheless, for lesions showing only low ^{124}I uptake (<50 kBq/mL), large deviations in calculated LDpA up to 50% were observed. This indicates that PGC correction may have an important impact in a personalized dosimetry approach of DTC patients and should be applied if available.

Hybrid PET/MR imaging

As a result of the superior soft-tissue contrast of MRI over CT in head-neck imaging, ^{124}I PET/MRI is an attractive alternative to PET/CT for the application of ^{124}I lesion absorbed dose assessment in DTC patients. In Chapter 5 the quantitative performance evaluation of ^{124}I PET/MRI with the aim of performing lesion dosimetry in DTC was described. The effect of radiofrequency (RF) coil attenuation on PET image quantification was less than 5% and considered negligible for two commercially available PET-compatible RF coils used for head-neck imaging. However, coil-related attenuation artefacts resulting in significant underestimation of the measured radioactivity concentration up to 19% have been reported in literature [26, 27]. Therefore, PET-compatibility of RF coils must be confirmed for reliable dosimetry measurements.

In addition, using the default MR-based attenuation correction of the manufacturer in which bone is classified as soft-tissue, phantom measurements of bone-simulating tissue showed an increasing underestimation in measured ^{124}I radioactivity concentration up to 15% with increasing bone density and size. Alternatively, for head-neck imaging, the PET/MRI system facilitates PET attenuation correction in which bone, detected on a ultra-short echo-time (UTE) MR sequence, is assigned a fixed linear attenuation

coefficient. In contrast to the default MR-based attenuation correction method, this approach resulted in an overestimation in measured ^{124}I radioactivity concentration. These findings are in line with values reported in literature [28-31] and indicate the importance of improvements in MR-based attenuation correction, in particular for bone lesion quantification. Recently, a promising novel MR-based attenuation technique using bone mask pairs has been commercially introduced on PET/MRI systems and its impact on ^{124}I bone lesion quantification should be investigated.

Excellent agreement in ^{124}I PET/MRI and PET/CT quantitative performance was observed in a clinical setting according to the high interclass-correlation coefficients (ICC) values of 0.999 and 0.95 in segmented lesion volume and measured ^{124}I activity concentration. Therefore, we conclude that reliable ^{124}I PET/MRI-based lesion dosimetry is feasible in DTC patients.

Radiation protection

Besides the application of lesion absorbed dose assessment in radionuclide therapy, dosimetry is also required to calculate the radiation dose to personnel, the general population or the environment. This is in particular true for radionuclide therapy using large amounts of radioactivity. As a consequence, protective measures such as the placement of shielding materials in the walls of radionuclide treatment rooms are often required to fulfil legal requirements. Optimal cost-effective design of radionuclide treatment rooms requires a tailored dosimetry approach in which room size, occupation level of adjacent areas, radionuclide characteristics and total annual amount of radioactivity used has to be considered. The application of conservative analytic shielding calculations in general requires the use of numerous simplifications (for instance a radioactive point source geometry free in air and neglecting self-absorption of radiation in the patient's body) often resulting in an overestimation of the required shielding thickness or height. In Chapter 6, it was shown that Monte Carlo simulations can successfully be used to determine the contribution of radiation traveling over the applied shielding material and scattering of the ceiling to the total radiation dose outside the treatment room. As expected, the contribution of ceiling scatter to the total radiation dose, depends largely on room geometry and shielding thickness and height. In fact, when more than 4-5 half-value layers of shielding are used, ceiling scatter may become a dominant factor and should be considered. This analysis shows that tailored Monte Carlo-based dosimetry calculations can be used for cost-effective improved shielding designs in nuclear medicine facilities.

Future perspectives

In recent years, important developments in nuclear medicine instrumentation have been introduced. Apart from hybrid PET/MRI systems capable of performing simultaneous acquisition of high-quality PET and MR images, digital PET/CT systems with improved time-of-flight capability, spatial resolution and count rate sensitivity have become commercially available. Combined with novel advanced resolution recovery, PGC correction PET reconstruction algorithms, these developments will strongly improve quantitative PET performance. In addition, advanced user-friendly dosimetry software packages may facilitate the widespread use of personalized radionuclide therapy in a clinical setting. In DTC, the application of a personalized radioiodine approach based on pre-therapeutic ^{124}I PET/CT or PET/MRI dosimetry may result in an improvement of patient outcome, in particular for high-risk patients showing advanced disease. However, for a global adoption of pre-therapeutic personalized dosimetry in radioiodine treatment, randomized controlled studies showing a clear benefit of such approach with respect to the currently standard fixed activity approach will be essential.

General conclusion

Tailored dosimetry approaches are increasingly used to calculate the radiation dose to patients, personnel, general population or environment. In DTC patients, the application of personalized dosimetry, based on pre-therapeutic ^{124}I PET imaging, can be used as a prognostic tool to predict lesion response to radioiodine therapy. Furthermore, the use of a personalized dosimetry approach facilitates optimization of the therapeutic amount of radioiodine to be administered which may improve patient outcome and reduce adverse effects to therapy. The introduction of new developments in ^{124}I PET imaging, such as hybrid PET/MRI and PET reconstruction algorithms including PGC correction, will result in an improvement of the lesion absorbed dose estimation. However, for a widespread adoption of the application of personalized dosimetry in DTC, randomized controlled studies showing a benefit of such approach are essential.

References

1. Haugen, B.R., et al., *2015 American Thyroid Association Management Guidelines for Adult Patients with Thyroid Nodules and Differentiated Thyroid Cancer: The American Thyroid Association Guidelines Task Force on Thyroid Nodules and Differentiated Thyroid Cancer.* Thyroid, 2016. **26**(1): p. 1-133.
2. Luster, M., et al., *Guidelines for radioiodine therapy of differentiated thyroid cancer.* Eur J Nucl Med Mol Imaging, 2008. **35**(10): p. 1941-59.
3. Lassmann, M., et al., *EANM Dosimetry Committee series on standard operational procedures for pre-therapeutic dosimetry I: blood and bone marrow dosimetry in differentiated thyroid cancer therapy.* Eur J Nucl Med Mol Imaging, 2008. **35**(7): p. 1405-12.
4. Freudenberg, L.S., et al., *124I-PET dosimetry in advanced differentiated thyroid cancer: therapeutic impact.* Nuklearmedizin, 2007. **46**(4): p. 121-8.
5. Pettinato, C., et al., *Pretherapeutic dosimetry in patients affected by metastatic thyroid cancer using 124I PET/CT sequential scans for 131I treatment planning.* Clin Nucl Med, 2014. **39**(8): p. e367-74.
6. Luster, M., T. Weber, and F.A. Verburg, *Differentiated thyroid cancer-personalized therapies to prevent overtreatment.* Nat Rev Endocrinol, 2014. **10**(9): p. 563-74.
7. Gilliland, F.D., et al., *Prognostic factors for thyroid carcinoma. A population-based study of 15,698 cases from the Surveillance, Epidemiology and End Results (SEER) program 1973-1991.* Cancer, 1997. **79**(3): p. 564-73.
8. *Council Directive 2013/59/Euratom of 5 December 2013 laying down basic safety standards for protection against the dangers arising from exposure to ionising radiation, and repealing Directives 89/618/Euratom, 90/641/Euratom, 96/29/Euratom, 97/43/Euratom and 2003/122/Euratom.* Official Journal of the European Union, 2014: p. L13/1-L13/73.
9. Stokkel, M.P., *^{131}I therapy for treatment of differentiated thyroid carcinoma*, in *Procedure guidelines of nuclear medicine 2016*. 2016.
10. Lassmann, M., et al., *The use of dosimetry in the treatment of differentiated thyroid cancer.* Q J Nucl Med Mol Imaging, 2011. **55**(2): p. 107-15.
11. Clement, S.C., et al., *Intermediate and long-term adverse effects of radioiodine therapy for differentiated thyroid carcinoma--a systematic review.* Cancer Treat Rev, 2015. **41**(10): p. 925-34.
12. Qu, Y., R. Huang, and L. Li, *Low- and high-dose radioiodine therapy for low-/intermediate-risk differentiated thyroid cancer: a preliminary clinical trial.* Ann Nucl Med, 2017. **31**(1): p. 71-83.
13. Ben Ghachem, T., et al., *A comparison of low versus high radioiodine administered activity in patients with low-risk differentiated thyroid cancer.* Eur Arch Otorhinolaryngol, 2017. **274**(2): p. 655-660.
14. Han, J.M., et al., *Effects of low-dose and high-dose postoperative radioiodine therapy on the clinical outcome in patients with small differentiated thyroid cancer having microscopic extrathyroidal extension.* Thyroid, 2014. **24**(5): p. 820-5.
15. Schlumberger, M., et al., *Strategies of radioiodine ablation in patients with low-risk thyroid cancer.* N Engl J Med, 2012. **366**(18): p. 1663-73.
16. Verburg, F.A., et al., *Why the European Association of Nuclear Medicine has declined to endorse the 2015 American Thyroid Association management guidelines for adult patients with thyroid nodules and differentiated thyroid cancer.* Eur J Nucl Med Mol Imaging, 2016. **43**(6): p. 1001-5.
17. IKNL, *Schildkliercarcinoom, landelijke richtlijn 2.0.* 2015.
18. Kulkarni, K., et al., *The relative frequency in which empiric dosages of radioiodine would potentially overtreat or undertreat patients who have metastatic well-differentiated thyroid cancer.* Thyroid, 2006. **16**(10): p. 1019-23.
19. Jentzen, W., et al., *Assessment of lesion response in the initial radioiodine treatment of differentiated thyroid cancer using 124I PET imaging.* J Nucl Med, 2014. **55**(11): p. 1759-65.
20. Ruhlmann, M., et al., *High Level of Agreement Between Pretherapeutic 124I PET and Intratherapeutic 131I Imaging in Detecting Iodine-Positive Thyroid Cancer Metastases.* J Nucl Med, 2016. **57**(9): p. 1339-42.

21. Capoccetti, F., et al., *The effectiveness of 124I PET/CT in patients with differentiated thyroid cancer.* Q J Nucl Med Mol Imaging, 2009. **53**(5): p. 536-45.
22. Jentzen, W., et al., *Discrepant salivary gland response after radioiodine and MIBG therapies.* Q J Nucl Med Mol Imaging, 2017. **61**(3): p. 331-339.
23. Siegel, J.A., et al., *MIRD pamphlet no. 16: Techniques for quantitative radiopharmaceutical biodistribution data acquisition and analysis for use in human radiation dose estimates.* J Nucl Med, 1999. **40**(2): p. 37S-61S.
24. Jentzen, W., et al., *Optimized 124I PET dosimetry protocol for radioiodine therapy of differentiated thyroid cancer.* J Nucl Med, 2008. **49**(6): p. 1017-23.
25. Jentzen, W., L. Freudenberg, and A. Bockisch, *Quantitative imaging of (124)I with PET/ CT in pretherapy lesion dosimetry. Effects impairing image quantification and their corrections.* Q J Nucl Med Mol Imaging, 2011. **55**(1): p. 21-43.
26. Delso, G., et al., *Evaluation of the attenuation properties of MR equipment for its use in a whole-body PET/MR scanner.* Phys Med Biol, 2010. **55**(15): p. 4361-74.
27. Eldib, M., et al., *Markerless attenuation correction for carotid MRI surface receiver coils in combined PET/MR imaging.* Phys Med Biol, 2015. **60**(12): p. 4705-17.
28. Paulus, D.H., et al., *Whole-Body PET/MR Imaging: Quantitative Evaluation of a Novel Model-Based MR Attenuation Correction Method Including Bone.* J Nucl Med, 2015. **56**(7): p. 1061-6.
29. Aznar, M.C., et al., *Whole-body PET/MRI: the effect of bone attenuation during MR-based attenuation correction in oncology imaging.* Eur J Radiol, 2014. **83**(7): p. 1177-1183.
30. Berker, Y., et al., *MRI-based attenuation correction for hybrid PET/MRI systems: a 4-class tissue segmentation technique using a combined ultrashort-echo-time/Dixon MRI sequence.* J Nucl Med, 2012. **53**(5): p. 796-804.
31. Aasheim, L.B., et al., *PET/MR brain imaging: evaluation of clinical UTE-based attenuation correction.* Eur J Nucl Med Mol Imaging, 2015. **42**(9): p. 1439-46.

Summary

The aim of this thesis was to improve radiation dose assessment in radioiodine treatment in differentiated thyroid cancer (DTC), both for the application of personalized patient treatment using quantitative ^{124}I PET imaging and radiation protection of personnel and the general population. With respect to patient management, the application of lesion dosimetry, based on pre-therapeutic ^{124}I PET, may provide valuable prognostic information and allow for a personalized radioiodine treatment approach. A personalized radioiodine treatment approach facilitates dose escalation and may improve patient outcome, which is in particular important for high-risk DTC patients. In addition, for patients presenting with lesions showing high radioiodine uptake, a personalized treatment approach may yield lower amounts of radioiodine used in therapy and result in less adverse effects.

From the perspective of radiation protection, accurate dosimetry allows for improved shielding designs in radionuclide therapy facilities that are safe, cost effective and in line with the applicable legislation.

In Chapter 1 a general introduction on the application of radioiodine therapy in DTC is provided. In addition, the concept of performing personalized pre-therapeutic lesion absorbed dose assessment for radioiodine therapy in DTC, based on hybrid PET/CT and PET/MRI imaging, is described. Finally, the use of Monte Carlo-based dosimetry, aimed at radiation protection of visitors and personnel in radioiodine treatment, is discussed.

Chapter 2 provides a review of the literature with respect to personalized dosimetry approaches and relevant developments in molecular nuclear therapy. It is shown that advanced personalized dosimetry in radionuclide therapy is feasible and that developments in nuclear medicine imaging instrumentation and dosimetric software are evolving at a high pace. However, personalized procedures developed so far differ in approach and sophistication, and standard operating procedures necessary for a widespread implementation are only scarcely available.

In Chapter 3, the dose-response relationship of radioiodine therapy using a fixed-activity approach is retrospectively investigated for DTC by means of lesion absorbed dose assessment based on ^{124}I PET/CT examinations that were performed prior to the therapy. Using a novel segmentation technique, allowing accurate lesion volume estimation down to the ^{124}I PET spatial resolution volume, we found that lesions showing complete lesion response to the radioiodine therapy received a statistically significant higher lesion absorbed dose compared to lesions showing no or incomplete lesion response. In addition, receiver-operating-characteristic curve analysis demonstrated that pre-therapeutic ^{124}I PET/CT lesion dosimetry can be used as a prognostic tool to predict lesion response to radioiodine therapy.

Accurate ^{124}I PET quantification, and thus lesion dose assessment, is affected by the detected prompt gamma coincidence (PGC) events of ^{124}I. In recent years, different techniques for PGC correction have been investigated and have become commercially available. In Chapter 4 we investigated the impact of a PGC correction technique on ^{124}I PET/CT quantification for both phantom and patient data. In addition, the effect of PGC

correction on calculated lesion absorbed dose was determined. In phantom measurements, PGC correction substantially improved background uniformity. In addition, PGC correction resulted in significant higher sphere recovery coefficient values, measured ^{124}I lesion uptake and calculated absorbed lesion dose and should be applied whenever available.

Due to the superior soft-tissue contrast of MRI compared to CT for head-neck imaging, ^{124}I PET/MRI may become increasingly important in DTC patients. However, compared to PET/CT, in which a relatively straightforward CT-based PET attenuation correction is applied, quantitative PET/MRI is more challenging. In Chapter 5 the quantitative performance of ^{124}I PET/MRI, aimed at performing lesion dosimetry in DTC patients, was investigated. Using phantom measurements, it was shown that the ^{124}I radioactivity concentration was underestimated by 12%. The influence of radiofrequency coil attenuation on ^{124}I quantification was less than 5% and considered negligible. For bone-simulating lesions, standard MR-based attenuation correction, in which bone tissue is ignored, resulted in an additional underestimation of the ^{124}I activity concentration. This underestimation increased with increasing lesion density and diameter. In a clinical setting, an excellent agreement between PET/MRI and PET/CT segmented lesion volume and mean ^{124}I radioactivity concentration was observed for DTC patients. Therefore, we concluded that accurate lesion dose assessment in DTC patients is feasible based on ^{124}I PET/MR imaging.

Besides lesion dose assessment in patients, radiation dose calculations are also important in the shielding design of nuclear medicine therapy facilities. In practice, the shielding in walls is often limited to a height lower than the actual ceiling height. Consequently, radiation traveling over the shielding material and scattered by the ceiling may result in an important contribution to the radiation dose outside the radionuclide treatment facility. Using Monte Carlo simulations, in Chapter 6 this contribution of ceiling scattered radiation to the total radiation dose was investigated. As expected, we found that the shielding required for the primary radiation, measured in half-value layers, is an important factor in the relative contribution of ceiling scatter. In fact, when more than about four half-value layers of shielding are used, ceiling scatter becomes the dominant factor and should be taken into account in the shielding design. The results of this study will facilitate improvements in the design of radionuclide treatment facilities.

In Chapter 7, the results of the previous chapters are discussed in a broader perspective. Besides the current role of tailored dosimetry in DTC also the potential benefits of this approach are discussed together with the technical challenges and novel developments on ^{124}I PET-based lesion dosimetry.

Samenvatting

Het doel van deze thesis is het verbeteren van stralingsdosisberekeningen van patiënten met gedifferentieerd schildklierkanker die behandeling met radioactief jodium ondergaan. Dit betreft zowel de toepassing van een gepersonaliseerde patiënt behandeling waarbij gebruik wordt gemaakt van kwantitatieve ^{124}I PET imaging, als de bescherming tegen ioniserende straling van personeel en leden van de bevolking. Voor wat betreft patiënt management kan de toepassing van laesie dosimetrie, gebaseerd op pre-therapeutische ^{124}I PET imaging, waardevolle prognostische informatie verschaffen en gepersonaliseerde therapie met radioactief jodium mogelijk maken. Een gepersonaliseerde therapie benadering faciliteert dosis escalatie en kan de kans op succesvolle therapie verbeteren, hetgeen in het bijzonder van belang is voor hoog-risico schildklierkanker patiënten. Bovendien zou gepersonaliseerde jodiumtherapie, voor patiënten met laesies die veel radioactief jodium opnemen, kunnen resulteren in het gebruik van lagere hoeveelheden radioactief jodium en een afname van de nadelige effecten ten gevolge van de therapie.

Vanuit het perspectief van stralingsbescherming kan nauwkeurige dosimetrie leiden tot verbeteringen van afschermingsmaatregelen in radionuclide therapiekamers welke veilig, kosteneffectief en in overeenstemming met de vigerende wet- en regelgeving zijn.

In Hoofdstuk 1 wordt een algemene introductie met betrekking tot de toepassing van radioactief jodiumtherapie in gedifferentieerd schildklierkanker gegeven. Daarnaast wordt het concept van gepersonaliseerde, pre-therapeutische stralingsdosisberekeningen aan laesies, gebaseerd op hybride PET/CT en PET/MRI beeldvorming, beschreven voor jodiumtherapie bij gedifferentieerd schildklierkanker. Tot slot wordt het gebruik van Monte Carlo gebaseerde dosimetrie bij jodiumtherapie, ten behoeve van stralingsbescherming van personeel en leden van de bevolking, beschreven.

Hoofdstuk 2 verschaft een uiteenzetting van de literatuur betreffende gepersonaliseerde dosimetrie methodieken en relevante ontwikkelingen in moleculaire nucleaire therapie. De mogelijkheden van het gebruik van geavanceerde, gepersonaliseerde dosimetrie in radionuclidentherapie zijn aangetoond en ontwikkelingen op het gebied van beeldvormende instrumentatie en dosimetrie software binnen de nucleaire geneeskunde vinden op hoog tempo plaats. De tot dusver ontwikkelde gepersonaliseerde procedures verschillen echter in benadering en complexiteit en standaard werkinstructies noodzakelijk voor een wijdverbreide implementatie zijn slechts in geringe mate beschikbaar.

In Hoofdstuk 3 is de dosis-response relatie van jodiumtherapie ten behoeve van schildklierkanker onderzocht in een retrospectieve studie middels berekening van de stralingsdosis welke door laesies is ontvangen tijdens therapie. De dosisberekening is hierbij uitgevoerd op basis van ^{124}I PET/CT onderzoeken uitgevoerd voorafgaand aan de jodiumtherapie. Door gebruik te maken van een nieuwe segmentatiemethode, waarmee een nauwkeurige schatting van het volume verkregen kan worden voor laesies groter dan het ^{124}I PET spatiële resolutievolume, hebben we gedemonstreerd dat laesies

welke volledig respondeerden op de jodiumtherapie een statistisch significant hogere stralingsdosis hebben ontvangen dan laesies die niet of onvolledig respondeerden. Bovendien is met een 'receiver operating characteristic curve' analyse aangetoond dat pre-therapeutische ^{124}I PET/CT laesie dosimetrie gebruikt kan worden als een prognostisch middel om de respons van laesies op therapie met radioactief jodium te voorspellen.

Nauwkeurige ^{124}I kwantificatie, en dus de berekening van de stralingsdosis van laesies, wordt beïnvloed door de detectie van zogenaamde prompt gamma coïncidentie (PGC) events van ^{124}I. Verschillende technieken om te corrigeren voor dit PGC effect zijn onderzocht en sinds kort commercieel beschikbaar. In Hoofdstuk 4 hebben we de impact van een PGC correctietechniek op de ^{124}I PET/CT kwantificatie onderzocht voor zowel fantoom- als patiëntdata. Daarnaast is het effect van de PGC correctie op de berekende stralingsdosis ontvangen door laesies bepaald. Voor fantoom metingen leidde de PGC correctie tot een substantiële verbetering van de achtergrond uniformiteit. Bovendien resulteerde PGC correctie in significant hogere 'sphere recovery coefficient' waardes, ^{124}I opname en berekende stralingsdosis van laesies en dient toegepast te worden indien dit beschikbaar is.

Vanwege het superieure weke-delen contrast van MRI ten opzichte van CT in hoofd-hals imaging bestaat de mogelijkheid dat ^{124}I PET/MRI in toenemende mate een belangrijke rol zal gaan spelen in gedifferentieerd schildklierkanker. Kwantitatieve PET/MRI is echter aanzienlijk complexer dan PET/CT, waarbij gebruik wordt gemaakt van een relatief eenvoudige CT-gebaseerde correctie voor PET verzwakking. In Hoofdstuk 5 is de kwantitatieve performance van ^{124}I PET/MRI, met als doel het toepassen van laesie dosimetrie in gedifferentieerd schildklierkanker, onderzocht. Middels fantoom metingen is aangetoond dat de radioactiviteitsconcentratie van ^{124}I werd onderschat met 12%. De invloed van verzwakking van de MRI spoelen op de ^{124}I kwantificatie bleek minder dan 5% te bedragen en werd als verwaarloosbaar beschouwd. De standaard MR-gebaseerde verzwakkingscorrectie waarin botweefsel wordt genegeerd, resulteerde in een verdere onderschatting in de gemeten ^{124}I activiteitsconcentratie voor gesimuleerde laesies die de eigenschappen van bot hadden. Deze onderschatting nam toe met toenemende laesie dichtheid en diameter. Voor gedifferentieerd schildklierkanker-patiënten werd in een klinische setting een zeer goede overeenkomst gevonden met betrekking tot het gesegmenteerde laesievolume en de ^{124}I radioactiviteitsconcentratie gemeten met PET/MRI en PET/CT. Daarom concludeerden wij dat een nauwkeurige schatting van de stralingsdosis ontvangen door laesies tijdens jodiumtherapie mogelijk is aan de hand van ^{124}I PET/MR imaging.

Naast de bepaling van de stralingsdosis ontvangen door laesies, speelt dosimetrie ook een belangrijke rol in het afschermingsontwerp van radionuclidentherapieruimtes. In praktijk is de afscherming vaak aangebracht tot een hoogte lager dan de hoogte van het plafond. Hierdoor kan straling, welke over de afscherming gaat, verstrooid worden aan het plafond en een belangrijke bijdrage leveren aan de totale stralingsdosis buiten

de radionuclidentherapieruimte. Op basis van Monte Carlo simulaties is in Hoofdstuk 6 de bijdrage van deze verstrooide straling ten opzichte van de totale stralingsdosis onderzocht. Zoals verwacht vonden we dat de dikte van de afscherming, nodig voor de afscherming van de primaire straling, uitgedrukt in het aantal halveringsdiktes, een belangrijke factor is voor de relatieve bijdrage van de straling verstrooid aan het plafond. Voor situaties waarin de dikte van de afscherming meer dan ongeveer vier halveringsdiktes bedraagt, kan straling verstrooid aan het plafond zelfs de dominante factor worden en dient deze dus meegenomen te worden in het ontwerp van de afscherming. De resultaten van deze studie maken de optimalisatie van het ontwerp van afscherming van radionuclidentherapieruimtes mogelijk.

In Hoofdstuk 7 worden de resultaten van de voorafgaande hoofdstukken bediscussieerd in een breder perspectief. Naast de huidige rol van gepersonaliseerde dosimetrie in gedifferentieerd schildklierkanker worden tevens de mogelijke voordelen van deze benadering besproken samen met de technische uitdagingen en nieuwe ontwikkelingen op het gebied van ^{124}I PET-gebaseerde laesie dosimetrie.

Valorisation

Relevance for society

Thyroid cancer is the most frequent endocrine malignancy having a yearly incidence of 3.1 and 9.3 per 100,000 for men and females, respectively. The last decades, the yearly incidence of thyroid cancer has shown a significant increase worldwide. Differentiated thyroid cancer (DTC), in which specific iodine uptake is preserved, comprises the vast majority of all thyroid cancers. When adequate treatment, including radioiodine therapy, is given, the prognosis of DTC is in general excellent for patients showing no distant metastases.

In clinical practice, empirically determined fixed amounts of radioiodine are generally administered in radioiodine therapy in DTC, according to Dutch and international guidelines. In this approach, the amount of radioiodine to be administered is based on disease and patient characteristics. However, it has been shown that radioiodine uptake of iodine-avid lesions, and thus the lesion absorbed radiation dose, varies highly, not only between different patients but also between different lesions within the same patient. In addition, radioiodine treatment in DTC patients may result in adverse effects such as salivary gland dysfunction, transient gonadal dysfunction and secondary primary malignancies which have been shown to correlate with increasing radioiodine activity. As a consequence, the fixed activity radioiodine therapy approach may result in an under- or overdosing of patients. Indeed, for patients presenting with distant metastases, chances of successful therapy are decreased substantially. In addition, recurrence rate after initial treatment is relatively high and subsequent radioiodine therapy is needed in a considerable number of patients.

As an alternative to the fixed-activity approach, pre-therapeutic dosimetry assessment can be used to facilitate personalized radioiodine treatment. In fact, according to the 2013 council directive of the European Union, a tailored dosimetry approach is required for all medical radiotherapeutic purposes, including radionuclide therapy. In this thesis we have shown in a retrospective study that a personalized radioiodine approach, using pre-therapeutic ^{124}I PET/CT based lesion dosimetry, provided prognostic information with respect to lesion response. Therefore, we conclude that a personalized dosimetry approach may be useful in DTC patient management, in particular for high-risk patients.

Target groups

The results of our studies with respect to ^{124}I PET based lesion dosimetry are of interest for radiologists and nuclear medicine physicians, endocrinologists, medical physicists, radiation protection experts and, most importantly, in the future also for patients suffering from DTC. The application of a tailored dosimetry approach in DTC may result in optimized and individualized radioiodine treatment. On the one hand, this would facili-

tate lesion dose escalation and may improve patient outcome, which is in particular important in high-risk DTC patients presenting with distant metastases. On the other hand, for patients with lesions showing high radioiodine uptake, a personalized treatment approach may yield lower amounts of radioiodine used in therapy and result in less adverse effects.

The results of our study to the contribution of ceiling scatter to the total radiation dose outside nuclear medicine treatment rooms are of interest for radiation protection officers, radiation protection experts and medical physicists and allow for improved shielding designs in nuclear medicine departments which are save, cost effective, and in line with the applicable legislation.

Activities

The overall aim of this thesis was to improve radiation dose assessment in radioiodine treatment in DTC, both for the application of personalized patient treatment using quantitative ^{124}I PET imaging and radiation protection of personnel and the general population. To this end, first we provided an overview of currently used personalized dosimetry approaches and relevant developments in the field of molecular nuclear therapy. Moreover, we investigated the quantitative characteristics of PET/MRI with respect to ^{124}I PET lesion dosimetry in radioiodine therapy in DTC patients. Using both phantom and patient data, we showed that accurate ^{124}I PET/MRI quantification with the aim of performing pre-therapeutic lesion dosimetry in DTC patients is feasible in a clinical setting. As PET/MRI offers a superior soft-tissue contrast in the head-neck region compared to PET/CT, in the future, PET/MRI may become increasingly important for specific clinical tasks (such as children with DTC) or, at least, in combination with PET/CT a modality of choice for ^{124}I PET imaging in DTC patients. In addition, we investigated the impact of a novel sinogram-based prompt gamma coincidence correction technique on ^{124}I PET uptake quantification and on the lesion absorbed dose estimation in DTC. It was shown that prompt gamma coincidence correction may have a substantial impact in a personalized radioiodine approach, in particular for small lesions showing low ^{124}I uptake, and should be applied whenever available.

So far, the results described in this thesis have been reported in one review article and three original research articles that were published in peer-reviewed scientific journals in the field of nuclear medicine or medical physics. In addition, results were presented on the international congress of the European Association of Nuclear Medicine.

Innovation

Although dosimetry in radionuclide therapy is still greatly in development, advanced tailored dosimetry based on pre-therapeutic imaging has been reported feasible in recent years. Important developments in nuclear medicine instrumentation improving (quantitative) image quality such as hybrid SPECT/CT, PET/CT and PET/MRI systems, time-of-flight PET, digital PET detectors and novel advanced reconstruction algorithms using sophisticated physics models have become commercially available. In addition, the development of dosimetric software programs capable of performing personalized dosimetry is still evolving at high pace.

Implementation of a pre-therapeutic ^{124}I PET dosimetry approach in a clinical setting is limited as a result of a lack of supporting evidence from randomized controlled trials, long standing professional traditions, personal expertise and reimbursement issues. Furthermore, reliable lesion dosimetry is technically challenging, time consuming and expensive.

In this thesis we have shown in a retrospective study that lesions showing complete lesion response to radioiodine therapy received a statistically significant higher lesion absorbed dose, assessed from pre-therapeutic ^{124}I PET/CT, compared to lesions showing no or incomplete lesion response. Moreover, pre-therapeutic ^{124}I PET/CT based lesion dosimetry provided prognostic information with respect to lesion response to radioiodine treatment, indicating that a personalized dosimetry approach may be useful in patient management and improve treatment outcome.

Planning and realisation

The research described in this thesis was performed in a close collaboration with the university hospital of Essen and the university hospital RWTH Aachen. In addition, for one study we collaborated with the university hospital of Essen, and the university of Twente.

Hybrid PET/MRI systems have recently become commercially available. Although to date no studies have been published in which the added value of ^{124}I PET/MRI imaging in DTC patients was investigated for a large number of patients, this thesis demonstrated the feasibility of performing pre-therapeutic ^{124}I PET/MRI based lesion dosimetry. As PET/MRI offers a superior soft-tissue contrast in the head-neck region compared to PET/CT, PET/MRI may provide important added value over PET/CT imaging and may become a modality of choice for ^{124}I PET imaging in DTC patients in the future.

The concept of performing personalized radioiodine treatment in DTC patients, in which radiation absorbed dose calculations are considered in the decision-making of the amount therapeutic radioiodine to be administered in therapy, is described in the latest guidelines of both the American Thyroid Association and the European Associa-

tion of Nuclear Medicine. Moreover, the application of pre-therapeutic lesion absorbed dose assessment has been reported to result in a change in patient management for a substantial number of DTC patients. However, personalized radioiodine treatment based on pre-therapeutic dosimetry calculations is not recommended in the latest guidelines on radioiodine therapy in DTC as the biologic effectiveness of dosimetry-guided approaches has not been proven yet. In fact, to date, prospective randomized controlled studies addressing the optimal activity approach are lacking. Based on our results that showed that ^{124}I PET-based lesion dosimetry provides prognostic information on lesion response, we would strongly advocate cooperative efforts to establish a multicentre prospective ^{124}I trial to investigate the potential benefits of a personalized radioiodine approach over the empirically determined fixed-activity approach.

List of publications

Wierts R, Jentzen W, Quick HH, Wisselink HJ, Pooters INA, Wildberger JE, Herrmann K, Kemerink GJ, Backes WH, Mottaghy FM, *Quantitative performance evaluation of ^{124}I PET/MRI lesion dosimetry in differentiated thyroid cancer.* Phys Med Biol, 2017. [Epub ahead of print].

Schnerr RS, de Jong AN, Landry G, Jeukens CR, **Wierts R**, *Monte Carlo simulations of ceiling scatter in nuclear medicine: ^{99m}Tc, ^{131}I and ^{18}F.* Med Phys, 2017. 44(3): p. 1113-1119.

Verwer EE, Zegers CM, van Elmpt W, **Wierts R**, Windhorst AD, Mottaghy FM, Lambin P, Boellaard R, *Pharmacokinetic modelling of a novel hypoxia PET tracer [^{18}F] HX4 in patients with non-small cell lung cancer.* EJNMMI Phys, 2016. 3(1): 30.

Jentzen W, Verschure F, van Zon A, van de Kolk R, **Wierts R**, Schmitz J, Bockisch A, Binse I, *124I PET assessment of response of bone metastases to initial radioiodine treatment of differentiated thyroid cancer.* J Nucl Med, 2016. 57(10): p. 1499-1504.

Vöö S, Kwee RM, Sluimer JC, Schreuder FH, **Wierts R**, Bauwens M, Heeneman S, Cleutjens JP, van Oostenbrugge RJ, Daemen JW, Daemen MJ, Mottaghy FM, Kooi ME, *Imaging intraplaque inflammation in carotid atherosclerosis with 18F-fluorocholine positron emission tomography-computed tomography: perspective study on vulnerable atheroma with immunohistochemical validation.* Circ Cardiovasc Imaging, 2016. 9(5).

Hendrikx G, Bauwens M, **Wierts R**, Mottaghy FM, Post MJ, *Left ventricular function measurements in a mouse myocardial infarction model. Comparison between 3D-echocardiography and ECG-gated SPECT.* Nuklearmedizin, 2016. 55(3): p. 115-122.

Wierts R, Brans B, Havekes B, Kemerink GJ, Halders SG, Schaper NN, Backes WH, Mottaghy FM, Jentzen W, *Dose-response relationship in differentiated thyroid cancer patients undergoing radioiodine treatment assessed by means of 124I PET/CT.* J Nucl Med, 2016. 57(7): p. 1027-1032.

Peters M, Willems P, Weijers R, **Wierts R**, Jutten L, Urbach C, Arts C, van Rhijn L, Brans B, *Pseudarthrosis after lumbar spinal fusion: the role of ^{18}F-fluoride PET/CT.* Eur J Nucl Med Mol Imaging, 2015. 42(12): p. 1891-1898.

Peters MJ, **Wierts R***, Jutten EM, Halders SG, Willems PC, Brans B, *Evaluation of a short dynamic 18F-fluoride PET/CT scanning method to assess bone metabolic activity in spinal orthopedics.* Ann Nucl Med, 2015. 29(9): p. 799-809.

Hendrikx G, De Saint-Hubert M, Dijkgraaf I, Bauwens M, Douma K, **Wierts R**, Pooters I, van den Akker NM, Hackeng TM, Post MJ, Mottaghy FM, *Molecular imaging of angiogenesis after myocardial infarction by (111)In-DTPA-cNGR and (99m)Tc-sestamibi dual-isotope myocardial SPECT.* EJNMMI Res, 2015. 5:2.

Hanssen MJ, **Wierts R**, Hoeks J, Gemmink A, Brans B, Mottaghy FM, Schrauwen P, van Marken Lichtenbelt WD, *Glucose uptake in human brown adipose tissue is impaired upon fasting-induced insulin resistance*. Diabetologia, 2015. 58(3): p. 586-595.

van der Lans AA, **Wierts R**, Vosselman MJ, Schrauwen P, Brans B, van Marken Lichtenbelt WD, *Cold-activated brown adipose tissue in human adults: methodological issues.* Am J Physiol Regul Integr Comp Physiol, 2014. 307(2): p. R103-113.

Bauwens M, **Wierts R**, van Royen B, Bucerius J, Backes W, Mottaghy F, Brans B, *Molecular imaging of brown adipose tissue in health and disease*. Eur J Nucl Med Mol Imaging, 2014. 41(4): p. 776-791.

Makris NE, Boellaard R, Visser EP, de Jong JR, Vanderlinden B, **Wierts R**, van der Veen BJ, Greuter HJ, Vugts DJ, van Dongen GA, Lammertsma AA, Huisman MC, *Multicenter harmonization of 89Zr PET/CT performance.* J Nucl Med, 2014. 55(2): p. 264-267.

Zegers CM, van Elmpt W, **Wierts R**, Reymen B, Sharifi H, Öllers MC, Hoebers F, Troost EG, Wanders R, van Baardwijk A, Brans B, Eriksson J, Windhorst B, Mottaghy FM, De Ruysscher D, Lambin P, *Hypoxia imaging with [^{18}F]HX4 in NSCLC patients: defining optimal imaging parameters.* Radiother Oncol, 2013. 109(1): p. 58-64.

Vosselman MJ, Bran B, van der Lans AA, **Wierts R**, van Baak MA, Mottaghy FM, Schrauwen P, van Marken Lichtenbelt WD, *Brown adipose tissue activity after a high-calorie meal in humans.* Am J Clin Nutr, 2013. 98(1): p. 57-64.

Vosselman MJ, van der Lans AA, Brans B, **Wierts R**, van Baak MA, Schrauwen P, van Marken Lichtenbelt WD, *Systemic β-adrenergic stimulation of thermogenesis is not accompanied by brown adipose tissue activity in humans.* Diabetes, 2012. 61(12): p. 3106-3113.

Brans B, Weijers R, Halders S, **Wierts R**, Peters M, Punt I, Willems P, *Assessment of bone graft incorporation by 18 F-fluoride positron-emission tomography/computed tomography in patients with persisting symptoms after posterior lumbar interbody fusion.* EJNMMI Res, 2012. 2(1): 42.

Wierts R, de Pont CD, Brans B, Mottaghy FM, Kemerink GJ, *Dosimetry in molecular nuclear therapy*. Methods, 2011. 55(3): p. 196-202.

Wierts R, de Jong JR, Lazarenko SV, Paans AM, Dierckx RA, *Characteristics of a new system for monitoring the leakage factor during regional hyperthermic isolated limb perfusion*. Nucl Med Commun, 2011. 32(9): p. 853-862.

Wierts R, Janssen MJ, Kingma H, *Measuring saccade peak velocity using a low-frequency sampling rate of 50 Hz.* IEEE Trans Biomed Eng, 2008. 55(12): p. 2840-2842.

* Indicates equal contribution

Dankwoord

Na jaren hard werken is het einde van mijn promotietraject dan eindelijk in zicht. Gedurende deze periode heb ik proefondervindelijk ervaren dat mijn keuze om na mijn studie natuurkunde eerst in opleiding tot klinisch fysicus te gaan, om vervolgens alsnog te promoveren naast een fulltime baan als klinisch fysicus, mij voor een enorme uitdaging heeft gesteld. Tijdens mijn promotieonderzoek heb ik ontzettend veel steun en hulp gehad van veel mensen waarvan ik een paar mensen in het bijzonder wil bedanken.

Allereerst wil ik mijn promotoren Prof. dr. Mottaghy en Prof. dr. ir. Backes en copromotor Dr. Kemerink bedanken voor de manier waarop ik zelf richting heb mogen geven aan mijn promotieonderzoek en jullie kritische blik en constructieve feedback hierop. Hierdoor heb ik mij de laatste jaren kunnen ontwikkelen als wetenschapper op het gebied van de klinische fysica binnen de (nucleair geneeskundige) beeldvorming en radionuclidentherapie.

Beste Felix, direct na mijn opleiding in Groningen heb jij mij als klinisch fysicus aangenomen op de voormalige afdeling nucleaire geneeskunde van het MUMC+. Ik herinner mij hierbij nog goed dat in de gestelde vacature gevraagd werd naar een geregistreerd en gepromoveerd klinisch fysicus NG met minimaal 5 jaar werkervaring als klinisch fysicus. Ondanks het feit dat op het moment dat wij elkaar voor het eerst ontmoetten (dit was de dag nadat het Nederlands elftal de WK finale van Spanje had verloren) ik aan geen van deze eisen voldeed, besloot je mij toch aan te nemen, zonder ooit een officiële sollicitatiebrief van mij ontvangen te hebben. Hierbij hebben we van begin af aan de intentie en wederzijdse wens uitgesproken dat ik alsnog zou promoveren in Maastricht. Het verheugt mij dat ik met het afronden van mijn promotie de destijds gemaakte belofte eindelijk in kan lossen. Hartelijk bedankt voor het in mij gestelde vertrouwen. Ik hoop dat ik dit nog vele jaren mag blijven waarmaken.

Beste Walter, na jouw aanstelling als hoogleraar klinische fysica, heb ik je enkele jaren geleden gevraagd of je geïnteresseerd zou zijn om als mijn promotor op te treden. Hoewel jouw fysisch hart in eerste instantie bij MRI ligt, was jij hier graag toe bereid. Sinds die tijd heb je mij ontzettend gesteund en kon ik altijd met mijn vragen bij jou terecht. Jouw kritische kijk en feedback vanuit klinisch fysisch perspectief op mijn wetenschappelijke werk heeft mij meer dan eens uit mijn comfort zone gebracht, hetgeen uiteindelijk heeft geleid tot een aanzienlijke verbetering van de kwaliteit van mijn onderzoek. Ik denk dat onze samenwerking een mooi voorbeeld is hoe op een succesvolle manier invulling gegeven kan worden aan de fusie tussen radiologie en nucleaire geneeskunde. Ik wil je dan ook hartelijk danken voor al jouw inspanningen van de afgelopen jaren.

Gerrit, dankzij jou kwam ik na mijn opleiding in een gespreid bedje binnen op de afdeling nucleaire geneeskunde van het MUMC+. Volgens mij heb ik je nooit gezegd hoezeer ik destijds twijfelde over mijn keuze om in jouw voetsporen als klinisch fysicus NG van een academisch ziekenhuis te treden, waarbij ik de angst had om als onervaren klinisch fysicus niet te kunnen voldoen alle verwachtingen die hier aan mij gesteld zou-

den worden. Gedurende mijn eerste jaar in Maastricht ben jij nog een tijd aangebleven om mij wegwijs te maken binnen de afdeling en de rest van het MUMC+ en heb ik van jou nog veel mogen leren. Daarnaast was je zelfs bereid om na jouw pensionering als copromotor op te treden van mijn promotieonderzoek. Hierbij heb je me altijd geadviseerd om vooral mijn eigen keuzes te maken. Dank je wel hiervoor!

Dear Prof. dr. Jentzen, dear Tinho, my research would not have been possible without our pleasant collaboration. During the last five years you have shared your tremendous amount of expertise in the field of ^{124}I PET quantification and lesion dosimetry with me. Thank you so much for all your help! I always enjoy visiting you in Essen to discuss our next research projects. I hope we will be able to collaborate for many years and nice projects to come.

Beste Anne en Antoon, nog tijdens mijn afstudeeronderzoek van mijn masteropleiding technische natuurkunde besloten jullie om mij, afkomstig uit het uiterste zuiden van het land, aan te nemen als klinisch fysicus in opleiding op de afdeling nucleaire geneeskunde en moleculaire beeldvorming binnen het UMCG in het hoge noorden.

Ten tijde van het schrijven van dit dankwoord ontving ik helaas het droeve bericht van het overlijden van Anne. Anne, in de jaren dat jij mijn opleider was, heb ik op verschillende gebieden ontzettend veel van jou mogen leren, uiteenlopend van hoe je een fantoom homogeen met radioactiviteit vult, de (on)zin van het uitvoeren van periodieke metingen van de stralingsdosis op de afdeling NG, tot het aanbrengen van prioriteiten door gebruik te maken van het permanent archief. Nog elke dag ondervind ik hier veel profijt van. Het feit dat jij als één van de 'founding fathers' van de PET in Nederland mijn opleider geweest bent, beschouw ik als een grote eer.

Vanaf mijn eerste dag in het MUMC+ werd ik meteen opgenomen binnen de groep klinische fysica van de huidige afdeling beeldvorming. Walter, Eline, Cécile, Roald, Leonie en Harmen, de mogelijkheid om op fysisch inhoudelijk vlak met jullie te kunnen overleggen en periodiek elkaar op de hoogte te houden van relevante ontwikkelingen binnen het vakgebied, zie ik als een grote meerwaarde. Ik heb onze onderlinge samenwerking op klinisch fysisch gebied altijd als bijzonder prettig ervaren en ik hoop dan ook dat deze na de fusie alleen maar verder zal toenemen.

Tevens wil ik al mijn collega's bedanken die zich dagelijks inzetten op het gebied van de stralingsbescherming binnen de afdeling beeldvorming. Cécile, sinds begin 2016 zijn wij beiden gemandateerd als coördinerend stralingsdeskundige binnen het azM. Hierbij neem jij de röntgentoestellen voor jouw rekening en ik de radioactieve stoffen. Op deze manier hebben we de taken onderling goed verdeeld en kunnen we bij elkaar aankloppen wanneer dat nodig is. Ik hoop nog vele jaren samen met jou te kunnen optreden als coördinerend stralingsdeskundige van het azM. Maartje, al ruim vijf jaar werken wij nauw samen op het gebied van de stralingsbescherming binnen de nucleaire geneeskunde. Als toezichthoudend stralingsdeskundige ben jij niet alleen mijn rechterhand,

maar ook mijn ogen en oren op de afdeling. Ik zou niet weten hoe ik zonder jouw aflatende inzet de tijd zou hebben gevonden om aan mijn wetenschappelijke projecten toe te kunnen komen. Dank je wel voor al het goede werk dat je elke dag weer verricht. Axel, Ellen, Hub, Marieke, jullie bijdrage als toezichthoudend stralingsdeskundige en/of medewerker van het dosimetriecentrum binnen de groep stralingshygiëne heeft de stralingsbescherming binnen de afdeling beeldvorming de afgelopen jaren tot een hoger niveau getild. Ik verheug me altijd op onze jaarlijkse barbecue. Daarnaast wil ik iedereen bedanken die zich de laatste jaren actief heeft ingezet binnen de commissie röntgentoestellen en radioactieve stoffen. Tot slot wil ik nog iedereen van het RNL en de SBE bedanken voor de onderlinge samenwerking van de afgelopen jaren.

Natuurlijk wil ik ook al mijn (oud-)collega's van de afdeling beeldvorming die een bijdrage aan dit proefschrift hebben geleverd heel erg bedanken. In het bijzonder wil ik mijn dank uitspreken aan alle collega's van team 2 (nucleaire geneeskunde) en het PET/MRI team voor de fijne samenwerking van de afgelopen jaren. Zonder jullie was dit proefschrift niet tot stand gekomen.

Joachim, dank je wel voor de mogelijkheid om na de fusie van de afdelingen radiologie en nucleaire geneeskunde mijn promotietraject voort te kunnen zetten binnen de nieuwe afdeling beeldvorming en alle steun die je hierbij hebt geleverd. Boudewijn, het idee om retrospectief laesiedosimetrie op de ^{124}I data in Maastricht uit te voeren was initieel jouw voorstel. Ik moet toegeven dat ik aanvankelijk enigszins sceptisch was over de haalbaarheid van dit project, maar gedurende het project bleek mijn initiële terughoudendheid ongegrond.

Ivo, altijd ben jij bereid om mij te helpen wanneer ik activiteit nodig heb voor mijn (kwaliteits) metingen, bij het vullen van een fantoom of gewoon even ergens over van gedachten te wisselen. Tevens is jouw bijdrage aan het borgen van de kwaliteit van de laboratorium apparatuur cruciaal. Naast het feit dat je mijn collega en kamergenoot bent, beschouw ik je bovenal al geruime tijd als mijn vriend. Buiten het werk gaan we dan ook regelmatig met elkaar om. Ik hoop dat dit nog vele jaren zo mag blijven.

Matthias, meer dan eens heb ik jou de laatste tijd kunnen lastigvallen wanneer ik vragen had op het gebied van radiochemie of wanneer ik de behoefte had om de resultaten van mijn onderzoek met jou te bespreken. Omgekeerd weet jij mij regelmatig te vinden voor hulp op fysisch of stralingshygiënisch gebied. Ook koester ik de gezellige spelletjesavonden met onze groep die de afgelopen jaren georganiseerd zijn.

Naast mijn collega's zijn mijn vrienden ontzettend belangrijk geweest tijdens mijn promotieonderzoek. Sergiy, wij leerden elkaar elf jaar geleden kennen tijdens onze opleiding tot klinisch fysicus in Groningen. Tijdens onze opleiding hebben wij ontzettend veel steun aan elkaar gehad en heeft zich een hechte vriendschap ontwikkeld. De manier waarop jij als geboren Oekraïner je in Nederland hebt ontwikkeld en aangepast is bijzonder indrukwekkend. Ook nu wij ver uit elkaar wonen en we elkaar helaas relatief

weinig zien, houdt onze vriendschap stand. Ik realiseer mij dat dit zeker geen vanzelfsprekendheid is en hoop nog vele jaren bij jou op bezoek te mogen komen in Alkmaar.

Matthijs, onze vriendschap gaat helemaal terug tot aan de zandbak van de lagere kleuterklas van basisschool "De Schacht". Ik vind het ontzettend bijzonder hoe wij vanaf deze tijd nagenoeg hetzelfde traject in ons leven tot dusver hebben doorlopen. In Eindhoven waren we huisgenoten tijdens onze opleiding technische natuurkunde. Vervolgens besloten we allebei de opleiding tot klinisch fysicus te volgen, jij in Heerlen, ik in Groningen. En nu zullen we allebei in het voorjaar van 2018 vader worden. Ik hoop dat onze vriendschap nog vele jaren stand mag houden.

Dennis, onze vriendschap ontstond twaalf jaar geleden tijdens ons afstudeerproject in het provisorium van het azM. Vanaf het eerste moment konden wij het erg goed met elkaar vinden. Ook na mijn vertrek richting Groningen hielden we contact en spraken we regelmatig met elkaar af waarbij jij en Priscilla ook vaker een bezoek bij mij in het verre Groningen brachten. Ik ben nog steeds ontzettend vereerd en trots dat jullie mij ruim vijf jaar geleden vroegen als peetoom van jullie tweede kind Babet. In mijn ogen is dit het ultieme symbool van vertrouwen en vriendschap.

Uiteraard ben ik ontzettend veel dank verschuldigd aan mijn lieve familie en schoonfamilie.

Aron, het is niet in woorden te beschrijven wat onze band voor mij betekent. Als grote broer sta jij altijd voor mij klaar, no matter what. Je bent niet alleen de beste broer die ik me kan wensen, maar zoveel meer dan dat. Je bent mijn allerbeste vriend en deze vriendschap is onvoorwaardelijk. Dit heeft zich de laatste jaren onder andere geuit in het feit dat jij en Annet besloten hebben om Marieke en mij als peettante en peetoom van jullie eerste kind Sverre te benoemen. Daarnaast was jij afgelopen zomer één van de twee getuigen op onze bruiloft. Met Sverre en Stijn hebben jij een Annet een fantastisch gezin opgebouwd en ik wens jullie niks dan goeds voor de toekomst.

Pap en mam, het is vrijwel onmogelijk om jullie te bedanken voor alles dat jullie voor mij de afgelopen 34 jaar gedaan hebben. Bedankt voor jullie onvoorwaardelijke steun en liefde en alle mogelijkheden die jullie mij gegeven hebben om mijzelf te ontwikkelen. Nog steeds staan jullie altijd voor mij klaar wanneer ik raad nodig heb of er weer eens geklust moet worden in ons huisje. Ik hou van jullie.

Tot slot mijn lieve vrouw Marieke. Inmiddels zijn we al vijf jaar ontzettend gelukkig samen. Sinds afgelopen zomer heb ik bovendien de grote eer om je mijn vrouw te mogen noemen. Ik weet dat de afgelopen maanden voor ons niet makkelijk zijn geweest. Het afronden van mijn proefschrift betekende dat ik jou de afgelopen periode niet altijd de aandacht en tijd kon geven die je verdient, maar ondanks alles heb je mij altijd gesteund. Ik zal nooit vergeten hoe je mij in de eerste week van augustus 2017 vertelde dat je zwanger bent van ons eerste kindje. Hoewel de zwangerschap fysiek een zware belasting voor je is, blijf je altijd positief en vol goede moed. Je doet het supergoed en ik

ben ontzettend trots op je! Ik kan niet wachten om dit voorjaar onze zoon te mogen verwelkomen en samen met jullie mijn verdere leven te delen. Marieke, je bent het beste dat mij is overkomen, je bent mijn lief en ik hou van je met heel mijn hart.

Curriculum vitae

Roel Wierts was born on March 30th 1983 in Heerlen, the Netherlands. He graduated secondary school (VWO, gymnasium) with honour cum laude in 2001 at the St. Jans-college in Hoensbroek. Afterwards, he studied applied physics at the Technical University of Eindhoven. During his bachelor period, he was rewarded with the CIVI-price of the 'Hollandsche Maatschappij der Wetenschappen' for the best propaedeutic exam in applied physics in 2002. After receiving his Master of Science degree in applied physics with honour cum laude, he started as a medical physicist in training at the field of nuclear medicine at the department of nuclear medicine and molecular imaging at the university medical center in Groningen under supervision of Prof. dr. A.M.J. Paans. In 2011 he finished his medical physics training and started working as a medical physicist at the nuclear medicine department of the Maastricht university medical center, where he started his PhD project in parallel with his work as a medical physicist.